# UC Irvine
## UC Irvine Electronic Theses and Dissertations

**Title**
Probing solute-grain boundary interactions in alloys

**Permalink**
https://escholarship.org/uc/item/3bz979rh

**Author**
Hu, Yang

**Publication Date**
2020

Peer reviewed|Thesis/dissertation

UNIVERSITY OF CALIFORNIA,
IRVINE


Probing solute-grain boundary interactions in alloys


DISSERTATION


submitted in partial satisfaction of the requirements
for the degree of


DOCTOR OF PHILOSOPHY

in Materials Science and Engineering


by


Yang Hu


Dissertation Committee:
Associate Professor Timothy J. Rupert, Chair
Professor Martha L. Mecartney
Assistant Professor Mohammad Javad Abdolhosseini Qomi


2020

# DEDICATION

To my parents and grandparents,

whose strong support made it possible for me to complete this work.

I always remember the words given by my grandpa before I left for America,

千里之行，始于足下。
A journey of a thousand miles begins with a single step.

They motivate me to face challenges and overcome difficulties throughout my Ph.D. study.

# TABLE OF CONTENTS

Page

# LIST OF FIGURES

# LIST OF TABLES

# ACKNOWLEDGEMENTS

I would like to take this opportunity to first express my gratitude towards my advisor, Professor Timothy Rupert, who has guided me through the process of becoming a mature scientist during the past five years. He has always been inspiring, encouraging and patient. His help has been significant in all aspects of becoming an efficient researcher, from developing new ideas, to conducting simulations, to disseminating my research findings to the scientific community.

I would also like to thank the members of my thesis committee, Professor Martha Mecartney and Professor Mohammad Javad Abdolhosseini Qomi. Their helpful criticisms and suggestions have given me invaluable insight which has helped me improve my thesis as well as my presentation skills.

Special thanks go to all the members from the Rupert Lab for providing a great environment conducive to scientific discussion and an eagerness to assist fellow lab mates in need. It was a very pleasant time to work with such amazing researchers, Dr. Vladyslav Turlo, Dr. Zhiliang Pan, Dr. Zhifeng Huang, Dr. Jennifer Schuler, Charlette McDevitt and Megan McCarthy, just to name a few. Our discussions have stimulated creative research ideas and helped me solve some of my most difficult research problems.

Finally, I would like to thank those MSE graduate students who came to UCI the same year as I did. Some of them already graduated and may be in different parts of the world now. I am grateful to them for the days that we took classes together and studied for exams together.

Thank you all!

# CURRICULUM VITAE

## Yang Hu

### EDUCATION

| | |
|---|---|
| 2010-14 | Undergraduate Researcher, Program in Materials Science and Engineering, Northwestern Polytechnical University, Xi'an, Shaanxi, China |
| 2014 | B.E. in Materials Science and Engineering, Northwestern Polytechnical University, Xi'an, Shaanxi, China |
| 2015-18 | Graduate Research Assistant, Program in Materials Science and Engineering, University of California, Irvine |
| 2018 | M.S. in Materials Science and Engineering, University of California, Irvine |
| 2018-20 | Graduate Research Assistant, Program in Materials Science and Engineering, University of California, Irvine |
| 2020 | Ph.D. in Materials Science and Engineering, University of California, Irvine |

### RESEARCH EXPERIENCES

Dept. Materials Science and Engineering, UCI                    01/2016 - present

Graduate Research Assistant

Project: Multiscale alloy design of HCP alloys via twin mesh engineering,    09/2017 - present

PI: Prof. Timothy Rupert (In collaboration with Prof. Enrique Lavernia (UCI), Prof. Julie Schoenung (UCI), Prof. Irene Beyerlein (UC Santa Barbara) and Prof. Subhash Mahajan (UC Davis))

- Performed simulations on twin embryo growth in Mg and Mg alloys (molecular dynamics method)
- Developed continuum modeling on understandings the twin embryo growth mechanisms

Project: Doping metallic grain boundaries to control atomic structure and damage tolerance,
04/2016 - 09/2017

PI: Prof. Timothy Rupert

- Identified appropriate interatomic potentials for simulating interfacial segregation and structural transition

- Performed simulations (molecular dynamics method) on grain boundary segregation and structural transition in ternary alloys to explore the possibility of forming thicker amorphous intergranular films

Project: The role of water vapor and incorporated protons in enhancing diffusion and sintering in ceramics, 01/2016 - 04/2016

PI: Prof. Martha Mecartney (In collaboration with Prof. Ruqian Wu (UCI))

- Conducted simulations (first-principles calculations) on hydroxyl ion ($OH^-$) diffusion in α-alumina for explaining the water vapor assisted oxygen diffusion in α-alumina

Dept. Materials Science and Engineering, NPU 09/2014 - 09/2015

Graduate Research Assistant

Project: Defects in $HfO_x$-based thin films and their resistive switching characteristics,

PI: Prof. Zhengtang Liu

- Conducted simulations (first-principles calculations) on Au-doped $HfO_2$ single crystals for understanding the effect of Au dopants on the formation of conducting filaments

Project: 2D $WSe_x$: Al thin films for XOI p-FET and conductivity characteristics

- Conducted simulations (first-principles calculations) on Au, O-doped monolayer $MoS_2$ to explore improving Au–S bondings for nanodevice design

Dept. Geosciences, SBU 01/2014 - 07/2014

Visiting Student

Project: Graphene grain boundary structures prediction and electronic properties,

PI: Prof. Artem Oganov (National Overseas Program for Outstanding Undergraduates (Funded by China Scholarship Council))

- Performed simulations on predicting structures of graphene grain boundaries (USPEX) and exploring the electronic properties (first-principles calculations)

Dept. Materials Science and Engineering, NPU 06/2012 - 06/2014

Undergraduate Researcher

Project: High-performance gamma-ray detector based on CdZnTe (CZT), State Key Laboratory of Solidification Processing

(Students' Innovation Training Project (Funded by the Ministry of Education of PRC))

- Performed data analysis for understanding the carrier transportation using Hetch equation and the energy spectrum gained by CZT detector

Dept. Materials Science and Engineering, NPU                     01/2012 - 09/2013

Undergraduate Researcher

Project: Fechner color effect and its potential applications, Shaanxi Province Experimental Teaching Demonstrations on Physics

- Performed design on black and white patterns for observing the color change
- Performed data analysis to explore factors that influence (spinning speed, patterns designed) colors observed

## PUBLICATIONS

1. X Wang, **Y Hu**, K Yu, S Mahajan, IJ Beyerlein, EJ Lavernia, TJ Rupert, JM Schoenung. "Segregation and clustering of Y at {10-12} twin boundaries in a Mg-Y binary alloy," in preparation.

2. **Y Hu**, V Turlo, IJ Beyerlein, EJ Lavernia, S Mahajan, JM Schoenung, TJ Rupert. "Embracing the chaos: Alloying adds stochasticity to twin embryo growth," Physical Review Letters, in review.

3. **Y Hu**, V Turlo, IJ Beyerlein, EJ Lavernia, S Mahajan, JM Schoenung, TJ Rupert. "Disconnection-mediated twin embryo growth in Mg," Acta Materialia, 194, 437 (2020).

4. **Y Hu**, TJ Rupert. "Atomistic modeling of interfacial segregation and structural transitions in ternary alloys," Journal of Materials Science, 54, 3975 (2019).

5. **Y Hu**, JD Schuler, TJ Rupert. "Identifying interatomic potentials for the accurate modeling of interfacial segregation and structural transitions," Computational Materials Science, 148, 10 (2018).

6. J Su, Y Zhang, **Y Hu**, L Feng, Z Liu. "Tuning the electronic properties of bondings in monolayer $MoS_2$ through (Au, O) co-doping," RSC Advances, 83, 68085 (2015).

## CONFERENCE TALKS

1. **Y Hu**, V Turlo, S Mahajan, EJ Lavernia, IJ Beyerlein, JM Schoenung, TJ Rupert. "Manipulating twin morphology in Mg alloys by varying solute concentration," The Minerals, Metals and Materials Society (TMS) Annual Meeting & Exhibition, February 2020, San Diego, CA.

2. **Y Hu**, V Turlo, S Mahajan, EJ Lavernia, IJ Beyerlein, JM Schoenung, TJ Rupert. "Growth of twin embryos by disconnection propagation in Mg: Molecular dynamics and continuum modeling," Materials Science & Technology (MS&T) Conference and Exhibition, October 2019, Portland, OR.

3. **Y Hu**, TJ Rupert. "Atomistic modeling of interfacial segregation and structural transitions in ternary alloys," Materials Science & Technology (MS&T) Conference and Exhibition, October 2018, Columbus, OH.

4. **Y Hu**, TJ Rupert. "Identifying interatomic potentials for the accurate modeling of interfacial segregation and structural transitions," Materials Science & Technology (MS&T) Conference and Exhibition, October 2017, Pittsburgh, PA. (Poster)


## CONTRIBUTED TALKS

(Presenting author is shown in bold)

1. **X Wang**, Y Hu, K Yu, S Mahajan, IJ Beyerlein, EJ Lavernia, TJ Rupert, JM Schoenung. "{10-12} Boundary Segregation of Y in Mg alloys," The Minerals, Metals and Materials Society (TMS) Annual Meeting & Exhibition, February 2020, San Diego, CA.

2. **Y Su**, M Kumar, X Wang, Y Hu, K Yu, J Wang, S Mahajan, EJ Lavernia, TJ Rupert, JM Schoenung, IJ Beyerlein. "Characterization of twin-twin interactions in Mg," The Minerals, Metals and Materials Society (TMS) Annual Meeting & Exhibition, February 2020, San Diego, CA.


## TEACHING EXPERIENCES

- TA for ENGRMAE 157 at UCI                    01/2017 - 03/2017
- TA for CBEMS 169 at UCI                      04/2016 - 06/2016


## HONORS AND AWARDS

- March finalist, Robert W. Cahn Best Paper Prize for the Journal of Materials Science (03/2019)

- Merit Student of School of Materials Science and Engineering for the year of 2013

- Second-class Special Scholarship from Wu Xi Turbine Blade Co., LTD (11/2013)

- NPU Merit Student for the year of 2011 and 2012

- First Prize in 13th Northwestern Polytechnical University Undergraduate Mathematics Modeling Contest (06/2012)


## LANGUAGES

Chinese (Native), English (Fluent)

# ABSTRACT OF THE DISSERTATION

Probing solute-grain boundary interactions in alloys

by

Yang Hu

Doctor of Philosophy in Materials Science and Engineering

University of California, Irvine, 2020

Associate Professor Timothy J. Rupert, Chair

Grain boundaries are important planar defects which influence a variety of bulk properties, while the structures and behaviors of grain boundaries can be altered by solute atoms to enable the design of beneficial material performance. Different interactions between solutes and grain boundaries exist. One example is that under certain conditions, solutes travel to grain boundaries and change grain boundary chemistry and structure, to vary the so-called "grain boundary complexion" state. Current studies on grain boundary complexions have been primarily limited to binary alloys. While in ternary or quaternary systems, multi-element segregation might be utilized to create thicker amorphous intergranular films (AIFs), a structural feature that helps toughen nanocrystalline alloys. Another example is the migration of grain boundaries at the presence of solutes, a situation in which there are both segregated dopants on boundaries and dopants as solid solution additions in the surrounding crystal. A promising dopant concentration might be found at which grain boundary motion in alloys can be changed and therefore leads to optimal microstructure beneficial for material performance. To provide guidance to experiments as well as explaining the physical mechanisms responsible for the experimental observations,

atomistic modeling is chosen to address the challenges mentioned above. In this thesis, certain criteria for selecting appropriate interatomic potentials for modeling are first established. Then, the interfacial segregation and structural transition behavior in ternary alloys have been investigated and the possibility of forming thicker AIFs in certain ternary alloys by controlling the ratio of different dopant elements has been demonstrated, which could open up the opportunity of tuning the structure and properties of materials by co-doping. In the second part of the thesis, the migration of twin boundaries, basal-prismatic interfaces and conjugate twin boundaries (also referred to as twin tips in some cases) in pure Mg and Mg alloys has been studied. By understanding the effect of segregated dopants as well as randomly distributed dopants in the matrix on the motion of a group of special boundaries, it is able to alter the microstructure evolution by alloying and further tune the mechanical properties of Mg alloys.

# Chapter 1 Introduction

## *1.1 Motivation*

Interfaces are important planar defects in materials, especially those between the same phase but with different crystallographic orientations are called grain boundaries. Grain boundaries influence a variety of bulk properties such as the electrical resistance, densification during sintering, tensile strength, ductility, fracture toughness, fatigue resistance, formability, creep resistance, and thermal stability [1-6]. Early works on the conductivity of polycrystalline Cu showed that as the grain boundary area increases (i.e., grain size decreases), electrons are more strongly scattered by grain boundaries and the electrical resistance also increases [7]. During the sintering of ceramic materials, grain boundaries attract vacancies and allow for their accumulation and collapse, leading to enhanced densification [8]. Grain boundaries particularly play an important role in the mechanical responses of nanocrystalline metals. Nanocrystalline metals are a class of materials with grain size smaller than 100 nm, and therefore contain a large volume of grain boundaries, which directly causes the superior strength yet low ductility and thermal stability [9-14]. The high strength of nanometals comes from the hindrance of dislocation motion by the grain boundaries, higher stresses are required to further deform the material [9-11]. However, as the negative product of the limited motion of dislocations at grain boundaries, the existence of local stress concentration induces crack or voids formation near the grain boundaries and reduces the strain-to-failure [9-11]. Moreover, grain boundaries have higher energies than perfect crystals and these extra energies become the driving force for grain growth [12-14]. Therefore, nanometals are usually not thermally stable and once grain coarsening occurs, they lose the advantage of high strength.

One way to improve the overall bulk properties and enable the design of beneficial material behavior is through alloying. Following the previous discussion, to fight against the low thermal stability of nanocrystalline metals, 10 at.% Ta dopants were introduced into nanocrystalline Cu and only a 12% increase of grain size was obtained for samples annealed for 4 h at 0.5 $T_m$ (melting temperature of Cu) [15]. Compared with pure nanocrystalline Cu which was found to coarsen to the micron regime at 100 °C [16, 17], extraordinary stability was realized in the nanostructured Cu-Ta alloys. The sample microstructure shows the existence of Ta nanoclusters with various sizes at grain boundaries. This process of solute elements traveling to grain boundaries is called grain boundary segregation. An additional example of beneficial alloying effects is strengthening pure Mg. Nie et al. observed a periodic pattern of Gd and Zn atoms at coherent twin boundaries which exhibit a strong pinning effect on twin boundary migration, and therefore higher stresses are required to further activate twin boundary motion [18]. The two examples stated above both show some sort of solute-grain boundary interactions, which occur inevitably in all polycrystalline alloys. In both examples, solute atoms segregate to grain boundaries (twin boundaries are a special type of grain boundaries) and harden their motion. Two corresponding grain boundary phenomena, grain boundary segregation and grain boundary migration in the presence of solutes, make up the two main topics of this thesis.

## 1.2 Solutes alter grain boundary chemistry and structure

### 1.2.1 Grain boundary segregation

Grain boundary segregation describes the inhomogeneous distribution of solute atoms in the grain boundary region versus the grain interior. It is not uncommon to have a grain

boundary concentration several orders of magnitude higher than grain interior concentration [19]. In recent years, grain boundary segregation was gradually considered as a tool for site-specific manipulation which allows for optimizing grain boundary properties, rather than an undesired and inherited phenomenon, and so-called "grain boundary segregation engineering" was developed [20, 21]. Grain boundary segregation can be driven by reducing the grain boundary energy as well as reducing the lattice distortion caused by solutes being in the bulk. The thermodynamics of grain boundary segregation are described by different models regarding different interfacial phenomena, here we give a brief introduction of the Wynblatt-Ku [22, 23] model, as a basis for the discussion of ordered grain boundary segregation at low temperatures. Developed based on the so-called bond-breaking model, it is able to capture the segregation behavior under the conditions that grain boundary structure remains ordered with a specific number of segregation sites, yet fails to describe the situation of high solute concentration at which grain boundary structure becomes much rougher due to solute segregation. The model considers three main contributions to interfacial segregation: (1) the elastic contribution, (2) the interfacial energy contribution, and (3) the interatomic contribution. The total formulation for segregation enthalpy is shown in Eq. (1):

$$\Delta H_{seg} = -\frac{24\pi B\mu r_I r_M (r_I - r_M)^2}{3Br_I + 4\mu r_M} + (\sigma_I - \sigma_M)A^\Phi - \frac{\Delta H_m}{ZX_I X_M}\left[Z_L(X_I^\Phi - X_M) + Z_P\left(X_I - \frac{1}{2}\right)\right] \qquad (1)$$

where $r_I$ and $r_M$ are the atomic radii for the solute and solvent, $B$ is the bulk modulus of solute I, $\mu$ is the shear modulus of solvent M, $\sigma_I$ and $\sigma_M$ are the interfacial energies for elements I and M, $A^\Phi$ is the interface area per atom, $X_I$ and $X_M$ are the bulk concentration of I and M respectively, $X_I^\Phi$ is the interfacial concentration of the solute, $\Delta H_m$ is the enthalpy of mixing of the M-I alloy, $Z$ is the coordination number, $Z_L$ is the number of lateral bonds made by an

3

atom within its plane, and $Z_P$ is the number of bonds made with adjacent planes of atoms. The kinetics of grain boundary segregation involves discussions on atom diffusion, and heat treatment methods are usually applied to promote atom diffusion [15].

### 1.2.2 Grain boundary complexions

Segregating elements induce the formation of complexions, which are defined as interfacial states in thermodynamic equilibrium with adjacent grains and maintain a stable, finite thickness [24-26]. A complexion can be considered as a quasi-two-dimensional "phase", but it is different from the Gibbs definition of a phase due to the inhomogeneous and possible gradients of structure, composition, and other properties [24, 27, 28]. There is a variety of ways to categorize different types of complexions, according to the structure, composition, or degree of periodicity of complexions [28]. For example, using thickness as the categorization criterium, Dillon and coworkers first reported six types of complexions in the doped and undoped alumina [27], including clean grain boundary, monolayer complexion, bi-layer complexion, tri-layer complexion, nanolayer complexion and wetting films (see Fig. 1.1). Different types of grain boundary complexions can undergo phase-like transitions under certain thermodynamic conditions (temperature, pressure, chemical potential) [24, 27, 28]. An example would be Frolov et al. reported that a split-kite structure of the Σ5 (210) grain boundary in Cu-Ag system transforms to a filled-kite structure at 900 K after the grain composition of Ag reaches 0.02 at.% [25], and the related complexion type changes from the monolayer complexion to the bi-layer complexion. In this case, the grain boundary structure remains ordered and the grain boundary thickness is small. In other scenarios, much thicker complexions can be formed at the grain boundary after the doping

concentration reaches a certain level and at high temperature, and the grain boundary structure becomes amorphous as what is reported for Cu-Zr [29, 31, 32], Cu-Hf [31], Ni-Zr [31], Cu-Ag [30] and so on. The structurally disordered complexions, also referred as amorphous intergranular films (AIFs), play important roles in toughening nanocrystalline metals. Khalajhedayati et al. [29] observed enhanced ductility of nanocrystalline Cu-Zr alloys with AIFs than those with ordered grain boundaries, as shown in Fig. 1.2. Using molecular dynamics (MD) simulations, Pan and Rupert [33] provided an explanation for the much higher ductility of nanostructured Cu-Zr with AIFs, finding that AIFs can efficiently absorb incoming dislocations during plastic deformation and reduce the stress concentration at grain boundaries which delays crack initiation and propagation. The transition between different types of complexions can be characterized by the change of film thickness as well as grain boundary concentration of dopant versus the global dopant concentration. Take Cu-Zr nanoalloy as an example, Fig. 1.3 shows that as the global Zr concentration increases, the grain boundary complexions undergo four different stages as their thickness keeps increasing, and the formation of wetting films can be determined by whether the grain boundary concentration of dopant reaches a plateau [26].
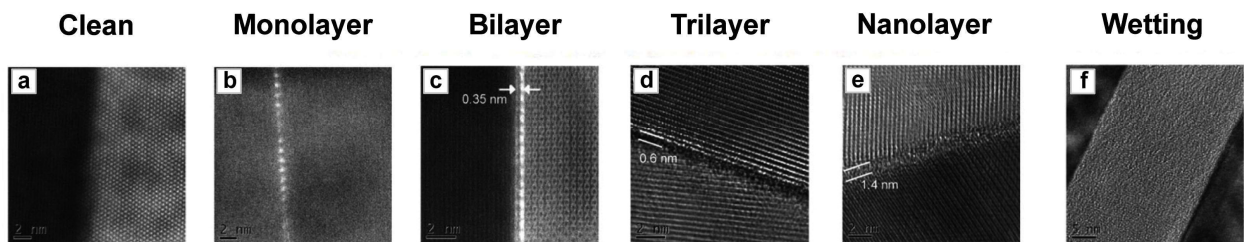


Fig. 1.1 The six discrete Dillon–Harmer complexions as originally discovered in undoped and doped (CaO, MgO, $SiO_2$, $Nd_2O_3$) $Al_2O_3$ (a–f) [28].
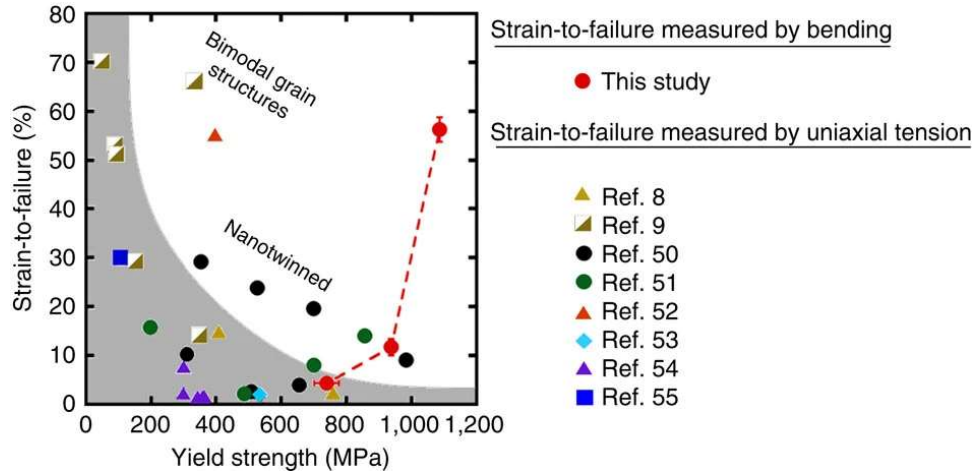
Fig. 1.2 The strain-to-failure versus yield strength for pure Cu and Cu-based alloys [29].
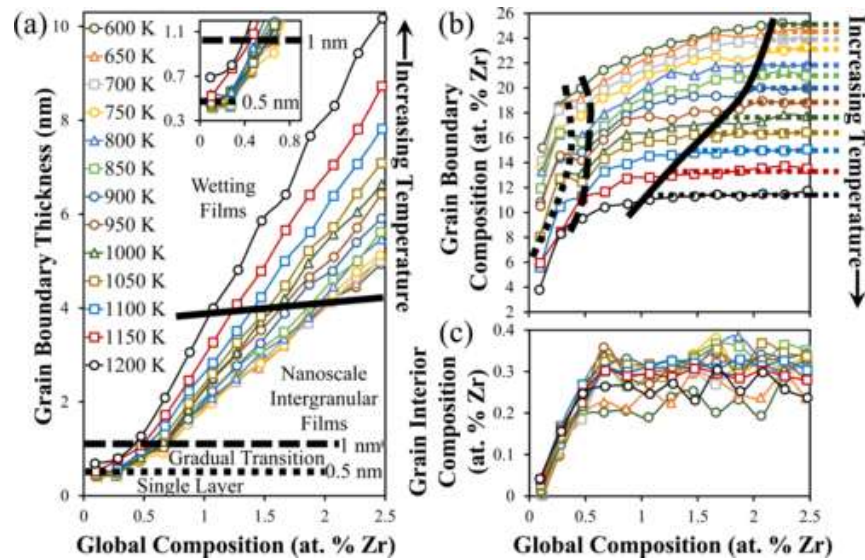


Fig. 1.3 (a) Grain boundary thickness, (b) grain boundary composition, and (c) grain interior composition as a function of global composition for samples containing Σ5 (013) grain boundaries and simulated at different doping temperatures. The inset of (a) shows the grain boundary thickness at the beginning of the doping process. Horizontal dotted lines in (b) mark the equilibrium grain boundary composition of the wetting film formed at temperatures denoted by the line color [26].

*1.3 Solutes alter deformation mechanisms in Mg*

*1.3.1 The strengths and weaknesses of Mg*

Mg and Mg-based alloys are chosen as model materials for the discussions on grain boundary migration, and the motion of special boundaries such as twin boundaries and basal-prismatic interfaces are focused. Mg and Mg alloys have received more and more attention in recent years due to their superior properties. Mg is the lightest structural material with high specific strength. It is, therefore, a promising material candidate in the fields of aerospace and automobiles. The application of Mg can significantly reduce the weight of aircrafts or vehicles and in turn decrease fuel costs and the carbon footprint, contributing to lower environmental impact [34-36]. Specific numbers are given in the following example. A typical car weighs around 1525 kg, containing about 975 kg of steel, 127 kg of Al, 114 kg of polymeric materials, and just 5 to 6 kg of magnesium [37]. While Mg is 33% lighter than aluminum, 60% lighter than titanium, and 75% lighter than steel, a tremendous impact can be achieved by replacing other materials with Mg alloys and composites. Other interesting properties of Mg include high thermal conductivity, a good castability, and the large abundance on earth [36]. A few applications of Mg alloys are realized on automobile components such as steering wheels, steering column parts, instrument panels, seats, gear boxes, air intake systems, stretcher, gearbox housings, and tank covers [36]. Non-automotive applications include hobby equipment and communication engineering [36]. However, the limited number of cases are negligible compare with the huge potential of Mg alloys. In fact, the data of structural materials currently used in aircrafts from Boeing Company shows that aluminium alloys are the major structural materials in most Boeing aircrafts, and composite materials also gain increasing

attention in recent years [38, 39]. The weaknesses which restrict the application of Mg and Mg alloys lie inherently in its crystal structure. Mg is a typical hexagonal close-packed (hcp) metal with less easy-activated slip systems than face centered-cubic (fcc) metals. According to the data shown in Table 1.1, the slip system requiring the least stress to be activated in Mg is the basal slip and the number of basal slip is only three, meaning that the strain along the <c> axis cannot be supported if only basal slips are activated in Mg and therefore it is impossible to have homogeneous plastic deformation (Von Mises criteria: five independent slip systems are needed to allow crystals undergo general and homogeneous strains without changing volume [40]). The much higher critical resolved shear stress to activate other slip systems in Mg also leads to plastic anisotropy and low formability. Therefore, it is essential to achieve an enhanced ductility or formability of Mg and Mg alloys to meet industrial needs.

Table 1.1 The slip systems for fcc, bcc and hcp metals [41]

| Metals | Slip Planes | Slip directions | # of slip systems |
|---|---|---|---|
| Face-centered cubic | | | |
| Cu, Al, Ni, Ag, Au | $\{111\}$ | $\langle 1\bar{1}0 \rangle$ | 12 |
| Body-centered cubic | | | |
| α-Fe, W, Mo | $\{110\}$ | $\langle \bar{1}11 \rangle$ | 12 |
| α-Fe, W | $\{211\}$ | $\langle \bar{1}11 \rangle$ | 12 |
| α-Fe, K | $\{321\}$ | $\langle \bar{1}11 \rangle$ | 24 |
| Hexagonal close-packed | | | |
| Cd, Zn, Ti, Mg, Be | $\{0001\}$ | $\langle 11\bar{2}0 \rangle$ | 3 |
| Ti, Mg, Zr | $\{10\bar{1}0\}$ | $\langle 11\bar{2}0 \rangle$ | 3 |
| Ti, Mg | $\{10\bar{1}1\}$ | $\langle 11\bar{2}0 \rangle$ | 6 |

### 1.3.2 Slip activities in Mg versus Mg alloys

Three slip systems are often observed in plastically deformed Mg and Mg alloys, the basal slip, the prismatic slip and the pyramidal slip. The Burgers vector and the critical resolved shear stress (CRSS) for each slip system are shown in Table 1.2. Pyramidal $\langle c+a \rangle$

dislocations are particularly interesting as shown by the work of Wu and Curtin [48], the activities of $\langle c+a \rangle$ dislocations help explain the origin of the low ductility of Mg. Wu and Curtin performed MD simulations to investigate the motion and dissociation of edge $\langle c+a \rangle$ dislocations initially located on pyramidal II planes. They observed a transformation of $\langle c+a \rangle$ dislocations into basal-dissociated products under applied compressive stress, and the final dislocation structure obtained at different stresses vary from basal $\langle c+a \rangle$, prismatic $\langle c \rangle$ + basal $\langle a \rangle$ to more complicated structures. These products on basal planes are energetically favorable yet immobile. This detrimental transition hardens the motion of edge $\langle c+a \rangle$ dislocations, and therefore the motion of $\langle c+a \rangle$ screw dislocations becomes critical and may be possibly tuned via alloying to achieve a higher ductility. Wu et al. [49] established mechanistic models (Eq. (2)) that relate the cross-slip energy barrier of $\langle c+a \rangle$ screw dislocations from the pyramidal II to pyramidal I plane ($\Delta G_{XS}$) with the energy difference between pyramidal I and II screw dislocations ($\Delta E^{I-II}$), which can be reduced by adding alloying elements. With a large reduction of $\Delta E^{I-II}$, screw dislocation cross-slip becomes favorable than edge dislocation transition to immobile structures, enabling rapid cross-slip and dislocation multiplication, and thus enhanced ductility of Mg alloys. Fig. 1.4 shows that rare earth elements and Zr and Ca are very effective in improving the ductility of Mg, with a little amount of solutes, the cross-slip energy barrier can be reduced to zero.

$$\Delta G_{XS} = \Delta G_{XS,i} + \Delta E^{I-II} l_{XS} + \Gamma \Delta s - \Delta \tau b A \tag{2}$$

Table 1.2 The slip plane, slip direction and CRSS for pure Mg

| Slip plane | Slip direction | CRSS (MPa) |
|---|---|---|
| {0001} | $\langle 11\bar{2}0 \rangle$ | 0.81[42], 0.76[43] |
| {10$\bar{1}$0} | $\langle 11\bar{2}0 \rangle$ | 39[44], 50[45] |
| {10$\bar{1}$1} | $\langle 11\bar{2}3 \rangle$ | 54[46] |
| {11$\bar{2}$2} | $\langle 11\bar{2}3 \rangle$ | 188, 197[47] |
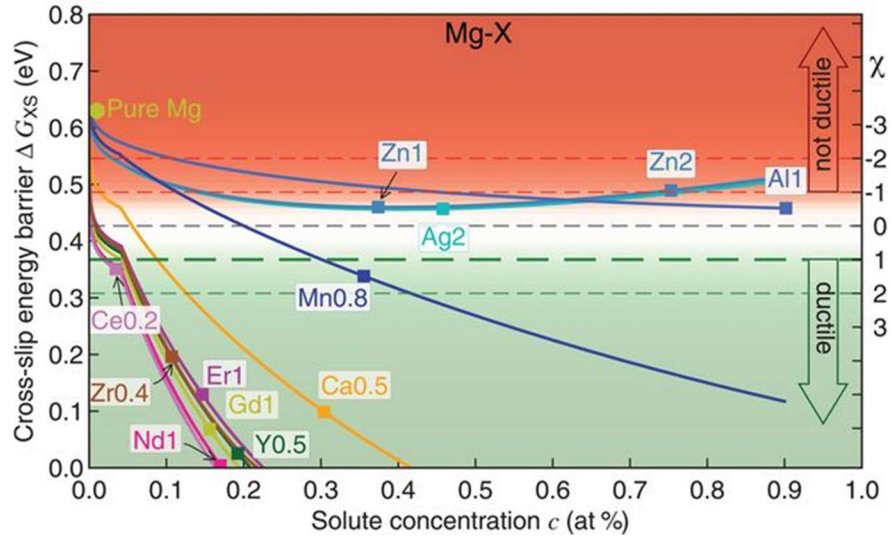
Fig. 1.4 Activation energy for screw dislocation cross-slip and ductility index $\chi$ for binary Mg alloys [49]. $\chi$ is an index indicating favorable and unfavorable conditions for ductility.

### 1.3.3 Deformation twinning in Mg versus Mg alloys

Twinning is an important deformation mode in Mg in addition to dislocation slip. Unlike basal slip, plastic strain along the c-axis can be accommodated through twinning, which contributes to the plasticity of Mg. Some common twinning modes in Mg include the tension twins $\{10\bar{1}2\}\langle\bar{1}011\rangle$, $\{11\bar{2}1\}\langle\overline{11}26\rangle$ and contraction twins $\{10\bar{1}1\}\langle10\bar{1}\bar{2}\rangle$, $\{11\bar{2}2\}\langle11\bar{2}\bar{3}\rangle$ [50] (see Fig. 1.5(a)). For each twin mode, there exist multiple twin variants. Take the $\{10\bar{1}2\}$ tension twin as an example, there are six twin variants for $\{10\bar{1}2\}$ tension twins, T1 $(\bar{1}102)[1\bar{1}01]$, T2 $(1\bar{1}02)[\bar{1}101]$, T3 $(\bar{1}012)[10\bar{1}1]$, T4 $(10\bar{1}2)[\bar{1}011]$, T5 $(0\bar{1}12)[01\bar{1}1]$, and T6 $(01\bar{1}2)[0\bar{1}11]$ [51-53] (see Fig. 1.5(b)). The six twin variants can be separated into three twin variant pairs, T1 and T2, T3 and T4, T5 and T6 are in the same twin variant pair. Members in the same twin variant pair exhibit 7.4° misorientation and are called co-zone

10

twins [51, 52]. The vast majority of attention has been given to the $\{10\bar{1}2\}$ tension twin, as

it is the most profuse twinning mode observed in deformed hcp metals [54, 55]. $\{10\bar{1}2\}$ twins

are easier to nucleate due to the lower shear and shuffle displacements required of atoms in

order to twin along the $\{10\bar{1}2\}$ plane [56]. In addition, $\{10\bar{1}2\}$ twinning planes can interact

with lattice defects, such as dislocations, to form interfacial twinning disconnections,

dislocations with a step character, that have been proposed as being responsible for twin

boundary (TB) motion [57-59]. Therefore, $\{10\bar{1}2\}$ twins can easily grow as well.
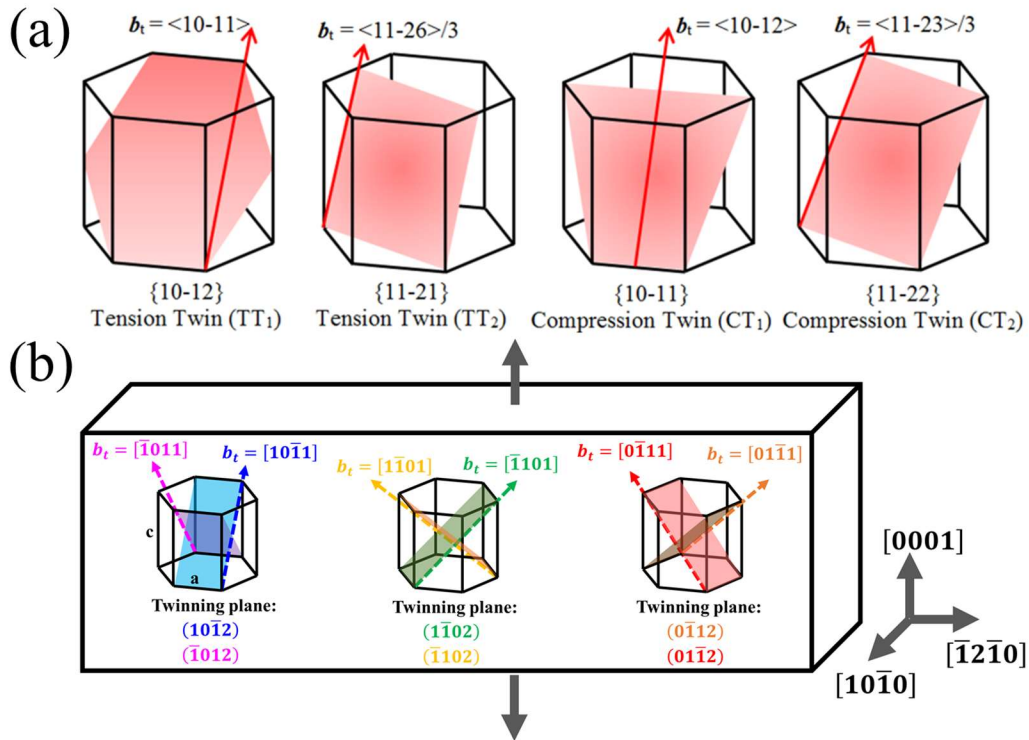


Fig. 1.5 Schematics of (a) different twinning modes in Mg [50], (b) different twin variants for
the $\{10\bar{1}2\}$ tension twin.

Twinning is a process that incorporates multiple length-scales, covering twin nucleation,

twin growth, and twin-twin interactions. Studies of twin nucleation can be traced back to

the 1950s when both homogeneous [60] and heterogeneous nucleation mechanisms [61] were first proposed. Heterogeneous nucleation assisted by dislocation slip, grain boundaries, free surfaces, or other defects requires less stress and energy, making it the likely dominant mechanism. In support of the concept of heterogeneous nucleation, Mendelson later found that the nonplanar dissociation of $\langle a \rangle$, $\langle c+a \rangle$, and $\langle c \rangle$ dislocations can all generate glissile twinning dislocations [62, 63]. More recent work by Wang et al. [64] showed that $\{10\bar{1}2\}$ tension twins can be nucleated through partial dislocation dipoles with Burgers vectors parallel to the twinning direction, forming twin embryos bound by TBs and basal-prismatic (BP) or prismatic-basal (PB) interfaces. BP/PB interfaces are asymmetric boundaries attached to TBs with a basal lattice facing a prismatic lattice (the choice of BP or PB is determined by whether the basal lattice plane is in the twin or the matrix) [65-67]. The growth of mature twins is realized through the formation and propagation of twinning disconnections on existing twin planes [68-73]. Twinning disconnections are defined as interfacial dislocations with both a Burgers vector and a step height, which exist to maintain the coherency at TBs during their migration. A magnified view of the atomic structure of a twinning disconnection is shown in Fig. 1.6. The step height is twice the interplanar spacing of the twin plane, and the Burgers vector is parallel to the twinning direction. Luque et al. [70] and Spearot et al. [73] have described the growth of mature twins in deterministic ways, twin boundary velocity (twin growth rate) is found to be a function of grain size, temperature, applied stress and characters of disconnection loops nucleated on the twin plane (such as disconnection loop size and step height, etc.). Twins eventually grow large enough so that the stress field around one twin can affect the growth of another twin [74, 75]. One twin can either terminate at another twin or terminate at the grain boundary and

induce the nucleation of twins in a neighboring grain, a phenomenon called twin transmission [76, 77].



$$b_t = \frac{1}{15}\,[10\bar{1}1]$$
$$h_d = 0.38\ nm$$
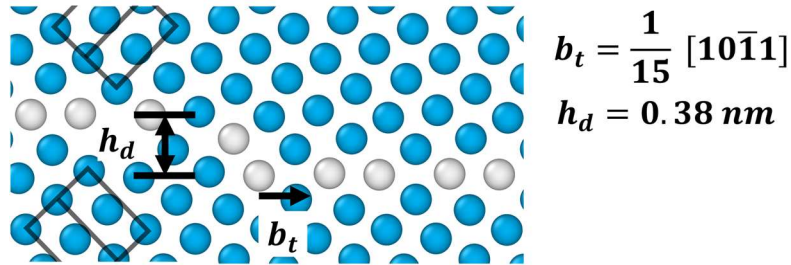
Fig. 1.6 A magnified view of the atomic structure of a twinning disconnection.

## *1.4 Atomistic simulation methods*

Most of the research studies mentioned above were in some way combined with modeling techniques to explore the physical mechanisms responsible for the behavior observed in experiments. Simulations are easier to conduct, require less time and expense, and are able to provide guidance for experiments. With the capability of tackling problems at different length-scale and time-scale, simulation methods can be classified into four groups, quantum mechanics methods, atomistic simulations, mesoscale modeling, and continuum modeling [78, 79] (see Fig. 1.7). In this thesis, two methods in the family of atomistic simulations are mainly involved, MD and Monte Carlo (MC) method. MD simulates the physical movements of atoms and molecules. It operates on a collection of atoms or molecules with initial positions and velocities, calculates the force associated with each atom via potential energy landscape and atomic position, and calculates acceleration using the force obtained from the last step, and then obtain the new position and velocity of each atom at the next time step (A schematic of the MD simulation procedures is shown in Fig. 1.8). Therefore, MD can naturally give time evolution of a material system. However, MD cannot

handle cases such as atom diffusion, in which the system evolves dynamically at an extremely slow rate. On the contrary, atoms can be given "unphysical" displacements in MC simulations which speeds up the simulated diffusion process. MC refers to a very broad class of computer simulations, which use randomness to calculate the properties of mathematical models. MC samples a variety of configurations from the potential energy landscape, and accept new configurations either have lower energies than the previous configurations or accept with some given probability of those configurations with higher energies. To take advantage of both MD and MC simulations, hybrid MD/MC methods were developed and are especially powerful in simulating grain boundary segregation and structural transition [82-84]. The classical MD simulation enables the structure relaxation while the MC simulation is used to find the chemical equilibrium faster.
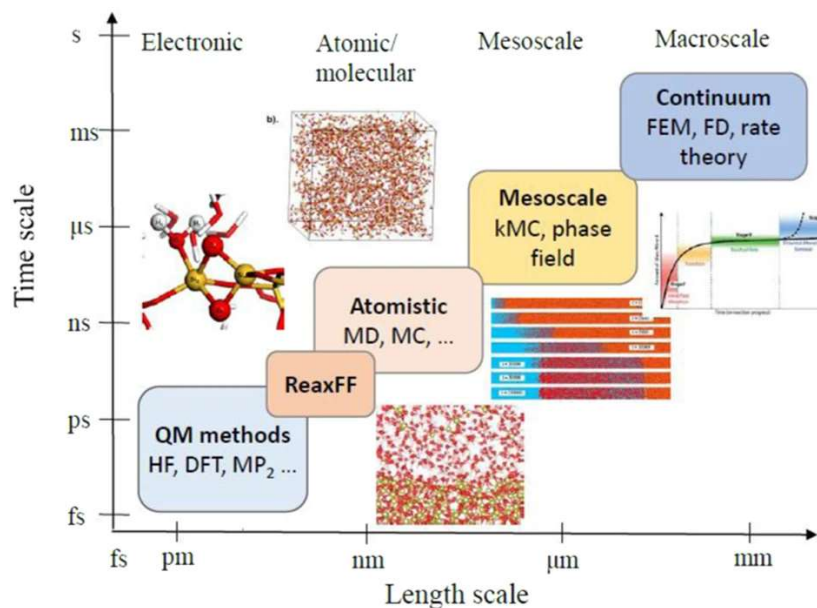


Fig. 1.7 Multi-scale modeling techniques which access different temporal and spatial scales [80].

## Molecular Dynamics
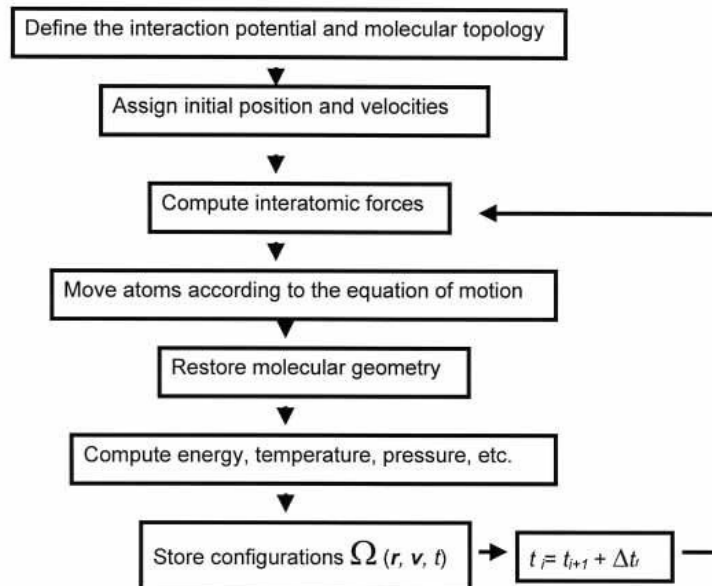


Fig. 1.8 MD simulation procedures [81].

One general concern of MC and MD simulations is that the reliability of simulation results depends on the choice of interatomic potentials which are developed for describing the interaction between atoms. Typically, the interatomic potential fitting process is guided by experimental data and/or first-principles calculations. In some cases, the relevant material properties or defects energies of interest are obvious. For example, a direct fit to anisotropic elastic moduli can be used if elasticity is of interest [85], while fitting to the experimental phase diagram will allow precipitation and phase separation to be modeled [86]. In other cases, it is more difficult to isolate the essential properties to be fit for accurate simulation, particularly when a given phenomenon is not directly related to an equilibrium thermodynamic parameter in the bulk. For instance, Dziedzic et al. [87] focused on the structure and mass transport properties of liquid Al-Cu alloys and compared three distinct potentials by their ability of reproducing total and partial pair correlation functions,

densities, angular distribution functions, coordination numbers, and self-diffusion coefficients. The authors found that two of the potentials failed to produce reasonable melting temperatures or densities of the targeted alloys, as well as missing the mark on other important properties, and thus were not appropriate for their study. However, even the potential which reproduced these properties still had difficulty reproducing local chemical ordering in an accurate manner. Similarly, Malerba et al. [88] tested the efficacy of four potentials for modeling radiation damage in Fe. They found that interatomic potentials fitted to first-principles forces (i.e., the slopes of potential-energy surfaces) or liquid structure factors (i.e., pair correlation functions) were able to more closely match available first-principles data for point defect formation and migration, key behaviors of interest when simulating radiation damage. Overall, selecting appropriate potentials for simulation is essential to obtain physical results rather than simulation artifacts.

## *1.5 Problem statement and research objectives*

It is clear that solute-grain boundary interactions are of great importance during materials processing and materials application. A more comprehensive understanding is required to explain materials behavior, and thus open opportunities for materials design. Although there are extensive studies on grain boundary phenomena in alloys since the last century, questions that are not answered still exist. Since it is such a fundamental topic covering different types of materials and different grain boundary behaviors, in this thesis, we focus on segregation-induced grain boundary complexions and special boundary motion in the presence of randomly distributed or segregated solutes, studying a range of materials

including Al-, Cu-, and Mg-rich alloys as our model systems for investigation. Issues to be addressed are summarized as follows:

First of all, in terms of simulating interfacial segregation and structural transitions, currently there are no guidelines for the selection of a suitable potential. Without confidence in the choice of interatomic potentials, convincing results cannot be expected.

Secondly, most of the current studies on grain boundary complexions are limited to binary systems as in ternary or quaternary systems, the interfacial segregation and structural transition behaviors can be complicated by the interaction between different types of segregated dopants at grain boundaries. In addition, the number of ternary or even quaternary interatomic potentials for simulation is limited. However, one may actually plan to have a complex chemical composition at the boundary as long as promising dopant pairs are selected. Impressive work has been done on the so-called "high-entropy complexion" in Ni-based alloys and it is found out that the multielement segregation may lead to extra (effective) grain boundary configurational entropies which helps in significantly reducing the grain boundary energy [89]. However, the theoretical part of this study was conducted by developing thermodynamic theories and equations, so an atomistic view about the grain boundary structure cannot be provided, the grain boundary chemistry was not investigated either. More simulation works in atomistic scale need to be done, which provides guidance for experimentalists and opens up the opportunity of tuning the structure and properties of materials by co-doping.

Thirdly, despite the efforts in studying twin nucleation and mature twin growth, twin embryo growth mechanisms have been largely neglected due to the difficulties of tracking their growth process experimentally. Twin embryos typically grow rapidly and become

mature twins by the time they are observed. However, the early stages of the twin embryo growth process should dramatically impact the morphology of mature twins, underscoring the critical need for a comprehensive model of twin embryo growth. We have mentioned earlier that twin thickening involves the nucleation and propagation of twinning disconnections (or twinning dislocations) on existing twin planes [68-73]. While the boundary of a twin embryo is a combination of twin planes, twin tips and basal-prismatic (BP/PB) interfaces, it is unclear the role of these BP/PB interfaces in the formation of twinning disconnections and the overall twin embryo growth. Especially during the early stages of twin growth, BP/PB interfaces make up a high fraction of the overall interfacial area separating the twin embryo from the matrix [64, 68, 90] and their presence may change which process controls twin embryo growth: nucleation or propagation of twinning disconnections. On the other hand, the migration process and growth mechanism of twin tips stay puzzling, the few existing reports on the lateral motion of TTs focus only on revealing the microstructure of the twin tip [68, 90-93].

Lastly, the effect of solutes on twin embryo growth needs to be understood. In the work by Cui et al. [94], we noticed the significant differences between the microstructures in pure Mg versus Mg-Al-Zn alloys, which provides hints that alloying can fundamentally change the twinning process. These authors observed the effect of solutes on detwinning in Mg-Al-Zn alloys compared with the detwinning process in pure Mg. Mechanical testing was performed on pre-compressed Mg, AZ31 (Mg-3.1Al-0.9Zn-0.45Mn, wt.%) and AZ91 (Mg-8.9Al-0.89Zn-0.42Mn, wt.%) alloys to initiate further twinning or detwinning, and the microstructure at the pre-compressed state as well as during the further deformation was tracked. All samples before pre-compression obtain similar grain size and basal texture, and thus the effect of

grain size and initial texture on twinning and detwinning can be excluded. Though not the focus of this study, the microstructure of the pre-compressed pure Mg, AZ31 and AZ91 samples shows that, there are more different twin variants being activated in the alloys than the pure Mg sample. Currently it is unclear whether alloying elements induce the formation of different twin variants, and if yes, whether it is a result of the changed local stresses due to adding solutes. The formation of the final twin morphology traces back to the growth of small twin embryos. As is mentioned earlier, Luque et al. [70] and Spearot et al. [73] have described the growth of mature twins in deterministic ways. However, whether the growth process of twin embryos in Mg alloys is deterministic as mature twins remains unclear.

The studies performed to address the issues mentioned above are categorized into four chapters:

- Chapter 2: Identifying interatomic potentials for the accurate modeling of interfacial segregation and structural transitions, and set up the selection criteria.

- Chapter 3: Investigate the interfacial segregation and structural transition in two model ternary alloys, and determine the possibility of forming thicker AIFs in multi-element systems.

- Chapter 4: Explore the atomistic growth mechanisms of a twin embryo in a single crystal of pure Mg, and then develop a phenomenological model for embryo growth to bridge between atomistic simulations and available experimental results.

- Chapter 5: Explore the solute effect on overall twin embryo growth, and the migration of faceted twin boundary. Two scenarios are considered, dopants with random distribution and dopants segregated at the faceted twin boundary.

# Chapter 2 Identifying interatomic potentials for the accurate modeling of interfacial segregation and structural transitions

## *2.1 Introduction*

It is only until recently that grain boundary segregation is considered as an approach for tailoring grain boundary properties, and the new concept of "grain boundary segregation engineering" has emerged. Following the increasing attention to this topic, more atomistic simulations are performed to simulate interfacial segregation and structure transitions. Since the reliability of atomistic simulations depends on the description of atomic interactions, criteria for the selection of an appropriate interatomic potential becomes imperative. In this chapter, we aim to set up such criteria to allow for accurate modeling of interfacial phenomena. Inspired by the thermodynamic equations describing interfacial segregation and structural transitions, we hypothesize that accurate reproduction of enthalpy of mixing and bond energies are required, and these quantities are strongly dependent on the fitting process used to develop the potential. The Cu-Zr alloy is chosen to test different interatomic potentials because of the available experimental results which provide a baseline for comparing simulated results obtained by different potentials. Four binary interatomic potentials, two using the embedded-atom-method (EAM) formulation and two using the Finnis-Sinclair formulation, are used. They have different mathematical forms and were constructed using a variety of physical properties so that are good representatives of the potentials used in this type of simulation. The criteria established based on the Cu-Zr alloy is then applied to Ni-Zr alloy to test the efficacy of our selection rule.

## 2.2 Computational Methods

Bicrystal models containing two Σ5 (310) grain boundaries were used as starting configurations. A Σ5 (310) grain boundary has a small, repeating kite-shaped structure (shown in Fig. 2.1) that allows for a reasonable simulation cell size, yet can act as a representative high-angle and high-energy grain boundary. Periodic boundary conditions were applied in all directions during the simulations. The simulation box has a length of approximately 23 nm (X direction), a height of 11 nm (Y direction), and a thickness of 4 nm (Z direction) containing 95,520 atoms. A hybrid Monte Carlo/molecular dynamics simulation method was used to simulate grain boundary segregation and any subsequent structural transitions [82]. Classical molecular dynamics simulations controlled the structural relaxation and were performed using the Large-scale Atomic/Molecular Massively Parallel Simulator (LAMMPS) package with an integration time step of 1 fs [95]. An isothermal-isobaric (NPT) ensemble with the Nose-Hoover thermostat/barostat was applied to relax samples at two temperatures (600 K and 1000 K) under zero pressure. To find chemical equilibrium, Monte Carlo simulations in a variance-constrained semi-grand canonical ensemble were performed after every 100 molecular dynamics steps.
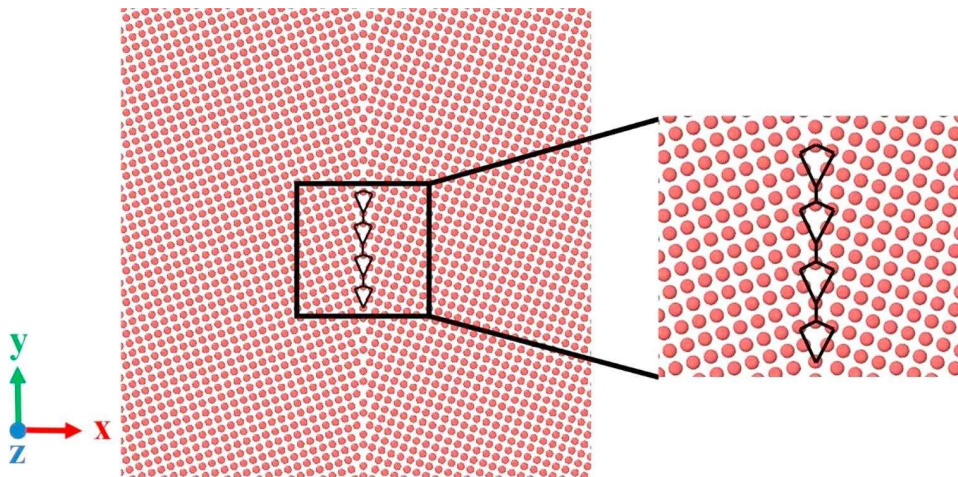
Fig. 2.1 A Σ5 (310) grain boundary in pure Cu (i.e., a clean grain boundary). The repeating kite-shaped structural unit is outlined by black lines.

Dopant concentrations of 0.4 and 4 at.% Zr were used to compare and contrast the four potentials for Cu-Zr. For the later simulations of Ni-Zr, compositions of 0.4 at.%, 5 at.% and 9 at.% Zr were explored. While high temperature and high Zr boundary concentration promotes the formation of thicker disordered intergranular films, ordered grain boundaries have been reported at low temperatures and dopant concentrations [32]. After structural and chemical equilibrium were achieved, a conjugate gradient energy minimization was used to remove any remaining thermal noise. All structural analysis and visualization of atomic configurations used the open-source visualization tool OVITO [96], with the local crystal structure of each atom identified according to common neighbor analysis (CNA) [97]. The potentials used in our simulation were developed by Cheng et al. [98], Ward et al. [99], Zhou et al. [100] and Mendelev et al. [101]. For brevity, we refer to these potentials using a combination of the first letter of each author's last name in the following sections. Based on the author's names for each publication, the potentials are referred to as the CSM potential, WAFW potential, ZJW potential, and MKOSYP potential.

## 2.3 Results

### 2.3.1 Experimental results for benchmarking (Experiments performed by Dr. Jennifer Schuler)

To provide an experimental baseline that can be used to validate the different potentials, Cu-Zr thin films were sputter deposited and subsequently processed to promote the

22

transformation of the grain boundary structure. While the average film composition was 4.3 at.% Zr, local variation in the Zr concentration at the grain boundaries was also observed, accompanied by disordered nanoscale intergranular films after quenching from 900 °C. Fig. 2.2(a) shows an HRTEM image of a grain boundary with an amorphous complexion that is approximately 2 nm thick. Fig. 2.2(b) is the corresponding EDS line profile scan showing that the concentration of Zr is ~1 at.% in the grain interior and ~6 at.% at the grain boundary. The exact EDS composition values are subject to uncertainty due to spatial averaging from the electron beam interaction volume, but Zr segregation to the grain boundary is clearly shown. Khalajhedayati and coworkers [29], [32] studied the Cu-Zr system as well and found similar results. In that study, a mechanically alloyed Cu-3 at.% Zr powder was created by ball milling followed by annealing and quenching, and those authors found similar disordered nanoscale intergranular films when the annealing temperature was at or above 850 °C. In contrast, samples that were annealed at 550 °C or 750 °C only contained ordered grain boundaries. Similar reports of segregation and amorphous film formation in other materials have also been reported in the literature (see, e.g., [27], [31], [102]). All of the experimental evidence presented here and available in the literature shows (1) interfacial segregation of Zr and (2) a structural transition to nanoscale amorphous complexions at high temperatures and sufficient dopant compositions. Therefore, interatomic potentials that are able to accurately describe interfacial segregation and grain boundary structural transition must be able to recreate these two features that were observed in the experiments.

(a) (b)
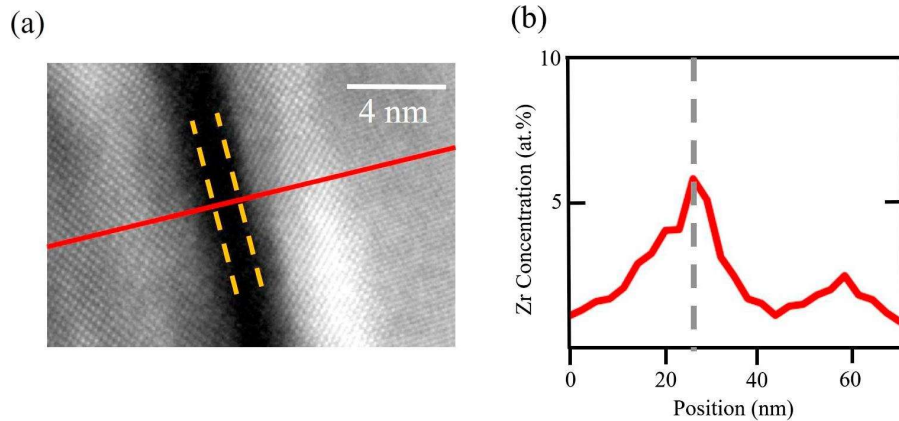
Fig. 2.2 (a) High resolution transmission electron microscopy (TEM) image of a nanoscale amorphous complexion at the grain boundary in a sputtered Cu-Zr sample. (b) EDS line profile scan across the grain boundary, showing Zr enrichment at the interface. The red line in (a) gives the scan path while the dashed yellow lines roughly outline the amorphous film. The grey line in (b) denotes the grain boundary location.

### 2.3.2 Zr segregation and complexion formation simulated by different potentials

The four potentials tested in this study predicted a variety of behaviors. The chemical and structural information of the doped Σ5 (310) grain boundary obtained by four potentials is shown in Fig. 2.3. We begin our analysis and discussion with the ZJW potential. Fig. 2.3 shows that Zr atoms segregate to the grain boundaries, occupying the kite tip at 600 K and 0.4 at.% Zr global concentration, while few can be found elsewhere. Finally, at a high Zr composition and high temperature, the positions of both Cu and Zr atoms at the grain boundary are randomly distributed and no repeating structural units are visible. The grain interior concentration at 4 at.% global Zr concentration is 3.6 at.% and 3.8 at.% at 600 K and 1000 K, respectively. These values are significantly higher than the ~1 at.% shown in Fig. 2.2(b), meaning the potential demonstrates a level of solid solubility that does not exist in

real Cu-Zr alloys. Therefore, the ZJW potential overestimates the solubility of Zr in the Cu lattice and underestimates the segregation tendency of Zr atoms to grain boundary sites. The WAFW potential was investigated next, again producing results that are quite different from experimental observations. An interesting feature that can be found is the formation of small Zr-rich clusters in samples doped with 0.4 at.% Zr at both 600 K. The formation of disordered intergranular films is captured at 1000 K for samples doped with 4 at.% Zr and the grain boundary concentration is 28.4 at.% Zr. Although the films are structurally amorphous as measured by the CNA parameter, they are chemically ordered (i.e., there is a patterning of chemical composition) and the grain boundary composition values are significantly higher than what was observed in the experimental reports. This high Zr segregation tendency and the formation of Zr-rich clusters are signs that the potential has limitations for modeling complexion transitions. The disordering behavior observed here happens when the Zr-rich clusters at the grain boundaries grow larger and eventually connect to each other. However, no such clustering is observed experimentally.

While the two potentials discussed above do not accurately reproduce Zr segregation, the CSM and MKOSYP potentials faithfully reproduce the expected segregation and formation of nanoscale amorphous complexions in a manner that is similar to experimental observations. For the CSM potential, Fig.2.3 shows that a monolayer complexion forms at the grain boundary with Zr atoms occupying the tip of the kite structure. As the global Zr concentration goes to 4 at.%, the grain boundary becomes fully disordered and a complexion of nanoscale thickness forms. The MKOSYP potential shows a similar transition from a monolayer complexion at low Zr concentration and temperature to an AIF at high Zr concentration and temperature.
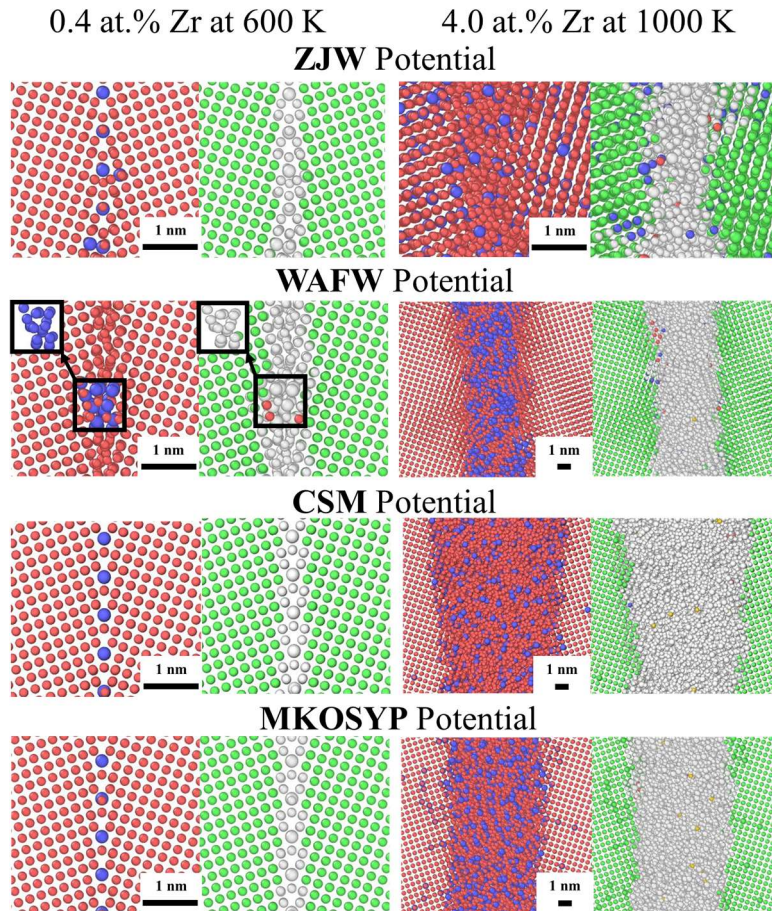
Fig. 2.3 The equilibrium chemical (left panel) and structural (right panel) information of the

Σ5 (013) grain boundary in Cu doped with 0.4 at.% Zr at 600 K, and 4 at.% Zr at 1000 K using

the ZJW, WAFW, CSM and MKOSYP potential.  In the panels on the left, Cu atoms are colored

red and Zr atoms are colored blue.  In the panels on the right, fcc atoms are colored green,

hcp atoms red, bcc atoms purple, icosahedral atoms yellow, and other atoms white.

## 2.4 Discussion

### 2.4.1 The ability of potentials to reproduce different physical quantities

The Wynblatt-Ku [22, 23] model was used as a basis for the discussion of ordered grain boundary segregation at low temperatures. While all of the parameters in Eq. (1) can affect an alloy's segregation enthalpy, many can be ruled out as the cause behind the disparate observations from our multiple simulations. Some of the calculated properties of Cu and fcc-Zr are shown in Table 2.1 for the four potentials studied here, along with experimental data or density functional theory (DFT) calculations to provide a reference. All of the potentials accurately reproduce the equilibrium lattice constants to an accuracy of approximately 0.5% as compared to the reference values. Other parameters such as $\Delta H_m$ of the alloy are more complicated and harder to recreate with the cross-potential terms, therefore being likely sources of poor fitting.

Table 2.1 Lattice parameters and grain boundary energies reproduced by different interatomic potentials

| Element | Cu | | | | |
|---|---|---|---|---|---|
| Interatomic Potential | ZJW[100] | WAFW[99] | CSM[98] | MKOSYP[101] | Reported data |
| Lattice Parameter (Å) | 3.615 | 3.614 | 3.597 | 3.639 | 3.616[103] 3.615[105] |
| Σ5 (310) GB energy (J/m²) | 0.783 | 0.784 | 0.901 | 0.903 | 0.88[105] |
| Element | fcc-Zr | | | | |
| Interatomic Potential | ZJW[100] | WAFW[99] | CSM[98] | MKOSYP[101] | Reported data |
| Lattice Parameter (Å) | 4.532 | 4.531 | 4.539 | 4.545 | 4.537[103] |

To probe the ability of the four potentials to reproduce the enthalpy of mixing of the Cu-Zr system, a 7.23 nm × 7.23 nm × 7.23 nm pure Cu model was first generated, and the Monte Carlo/molecular dynamics hybrid method was then used to introduce Zr into this bulk

sample.  An NPT ensemble was applied to the system at 1873 K and zero pressure, with the high temperature chosen so that our calculations could be compared with available experimental data taken from the liquid phase.  Experimental data from Turchanin et al. [106] is used as a reference.  As shown in Fig. 2.4, the CSM and MKOSYP potentials are able to reproduce the variation of enthalpy of mixing with respect to Zr concentration that is seen in the experimental data [106].  Alternatively, the enthalpy of mixing values obtained by the WAFW potential are positive at low Zr concentrations, marking a clear deviation from real material behavior.  In addition, the enthalpy of mixing obtained by the ZJW potential is much more negative (approximately 400% lower) than the reported data.  Using the Wynblatt-Ku model introduced above and keeping all other variables constant, a positive $\Delta H_m$ will enhance segregation and clustering of like atoms.  The positive values of enthalpy of mixing given by the WAFW potential contribute to the formation of Zr-rich clusters at the grain boundaries.  On the other hand, if $\Delta H_m$ is much too negative, like the behavior produced by the ZJW potential, there will be very little segregation of Zr to the grain boundaries because Cu-Zr bonds are favored in the lattice.
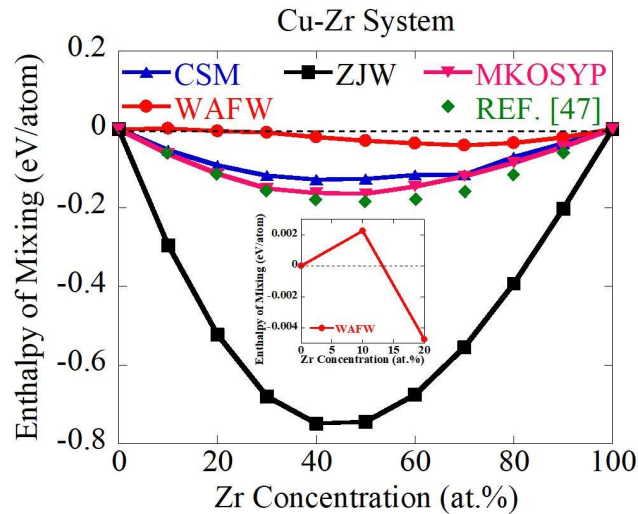
Fig. 2.4 Enthalpy of mixing of the Cu-Zr system calculated at 1873 K. The reference data comes from Turchanin [106]. The inset shows a zoomed view of the enthalpy of mixing from 0 at.% to 20 at.% Zr simulated by the WAFW potential.

In addition to segregation, the formation of amorphous complexions should also be related to a potential's ability to accurately reproduce the enthalpy of mixing. In their thermodynamic model for disordered complexion formation, Luo et al. [107] proposed that the stabilization of an AIF occurs when the free energy penalty for the formation of the film is smaller than the reduction in interfacial energy as a result of replacing a clean grain boundary with two crystal-liquid interfaces. A key consideration for the discovery of good glass formers is a negative enthalpy of mixing (see, e.g., [108]), meaning this parameter should be related to the energetic of the amorphous phase. In fact, Schuler and Rupert [31] recently created a set of materials selection rules for alloys that could sustain AIFs where a negative enthalpy of mixing was also of primary importance. Thus, the accurate reproduction of enthalpy of mixing by the CSM and MKOSYP potentials also leads to a realistic picture of disordered complexion formation at high temperatures and dopant compositions. Grain boundary energy can provide an additional metric to facilitate a comparison between the various potentials. The calculated energies of a clean $\Sigma 5$ (310) grain boundary simulated by each potential are shown in Table 2.1, along with a reliable energy value taken from DFT calculations [105]. Both the CSM potential and the MKOSYP potential recreate grain boundary energy with errors of less than 3% compared to the baseline value, while the ZJW and WAFW potentials give energies that are much too low.

### 2.4.2 Potential fitting process

To explain the various behaviors of potentials used in this study, one can return to inspect the fitting process used for each of the four potentials. For the ZJW potential, the pairwise cross-function is constructed solely based on the elemental two-body pair potentials, which use lattice constants, cohesive energies, bulk moduli, Voigt-average shear moduli, unrelaxed vacancy formation energies of pure Cu and Zr, and the dilute-limit heats of solution of Zr in Cu to fit the potential [100, 109]. Similarly, the WAFW potential is also constructed using the existed monatomic potentials from literature. Mixing enthalpies, bulk moduli, and lattice parameters of possible B2 and L12 Cu-Zr intermetallics are used for fitting the cross-potential term in this case [99]. Due to these limited fitting procedures, the ZJW and WAFW potentials are, at best, only able to reproduce the enthalpy of mixing at certain Zr concentration (e.g., Cu doped with an extremely small amount of Zr), which limits their application. In addition, only a few crystalline structures are considered for fitting the cross-potential terms for these two interatomic potentials. Such a limited procedure is problematic when studying systems containing defects like grain boundaries or systems which undergo interfacial structural transitions to amorphous complexions that are structurally and compositionally complex.

In contrast, the MKOSYP potential is constructed based on a previous developed interatomic potential for Cu-Zr [110] but adds additional complexity associated with a new pairwise cross-function created using experimental diffraction data, the liquid density at 1500 K of amorphous Cu64.5Zr35.5, and the enthalpy of mixing of the liquid state [101]. With features of multiple crystalline and amorphous states incorporated into the fitting procedure, a better reproduction of interfacial segregation is achieved. In addition, the use

of fitting to diffraction data for an amorphous Cu-Zr alloy is advantageous. An amorphous structure contains both free volume and a statistical distribution of bond lengths that are larger than the equilibrium lattice constant, both of which are features of a grain boundary's equilibrium structure. Thus, this potential can better capture the atomic bonding and its ability to reproduce interfacial energy is improved. The CSM potential incorporates additional complexity by using a force-matching method [111], where the potential energies, atomic forces (slope of potential-energy surfaces), and stress tensors of 954 configurations calculated by first-principles method are included in the fitting database. The addition of this detail allows the potential to more accurately describe the chemical bonding between atoms, since forces acting on atoms come from the interaction between electrons and the interaction between electrons and nuclei [111], all of which are captured by first-principles calculations. Moreover, a very broad range of structural configurations of pure Cu, pure Zr, and binary Cu-Zr alloys were used for fitting, including liquid phases, metallic glasses quenched at different cooling rates, and crystalline structures with interfacial and point defects [98, 112]. These configurations contain a variety of bonding types associated with the entire gambit of material defects that are important for reproducing interfacial segregation. In summary, the CSM and MKOSYP potentials provide overall better reproduction of the physical properties such as enthalpy of mixing and grain boundary energy that appears in Eq. (1) above, leading to more realistic modeling of interfacial segregation behavior.

### 2.4.3 Apply potential selection rule to Ni-Zr alloy

To show that the observations above are useful for other materials besides Cu-Zr, we simulate interfacial segregation and complexion transitions in Ni-Zr. Schuler and Rupert [31] have recently shown that this alloy can sustain thick AIFs, due to the segregation of Zr to the grain boundaries and the negative enthalpy of mixing, which reduces the penalty for an amorphous phase. The same bicrystal configuration was used here, containing two $\Sigma 5$ (310) grain boundaries. An interatomic potential which fits to the ab initio atomic forces and thus satisfies the requirement of accurately reproducing the enthalpy of mixing (as shown in Fig. 2.5), bond energies and other physical properties were chosen [113]. A few examples of equilibrium grain boundary structures are provided in Fig. 2.6, with chemical information in the left panel of each figure part and structural information in the right panel. Fig. 2.6(a) and (b) show that the segregation of Zr occurs but that the lattice can also accept some Zr atoms. A sudden increase in film thickness occurs when the global concentration reaches 9 at.% Zr, signaling the formation of an amorphous nanoscale complexion. The lower segregation tendency of Zr in Ni, as compared to Cu, is consistent with a higher solubility on the bulk phase diagram [114].
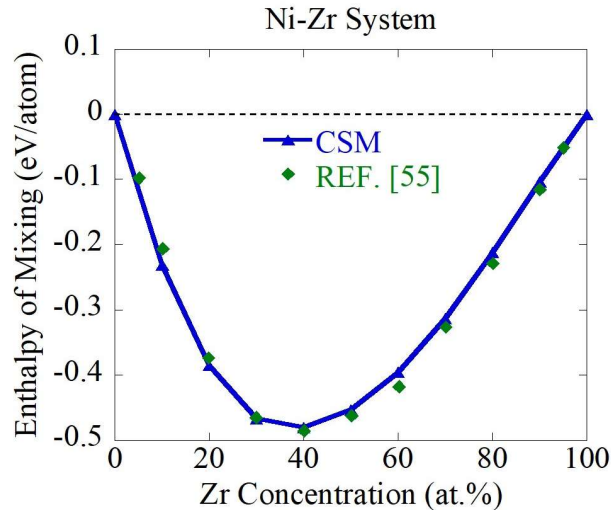
Fig. 2.5 Enthalpy of mixing of Ni-Zr system calculated at 1873 K. The reference data comes from Turchanin et al. [113].
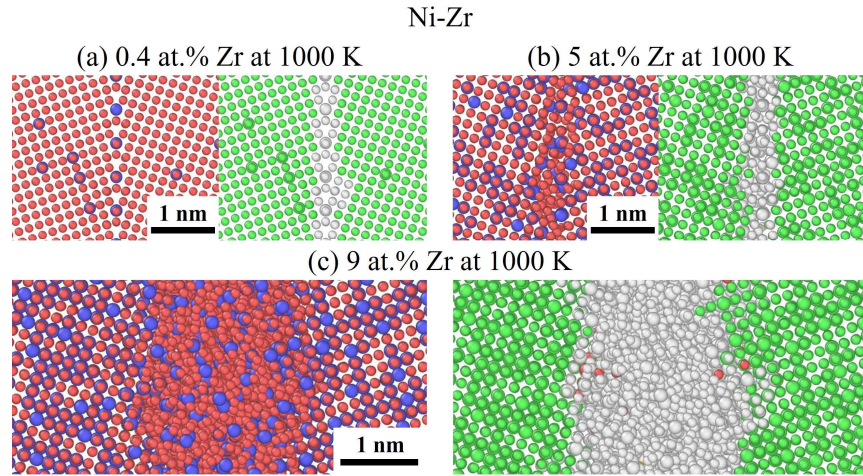


Fig. 2.6 The equilibrium chemical (left panel) and structural (right panel) information of the Σ 5(013) grain boundary in Ni doped with (a) 0.4 at.% Zr at 1000 K, (b) 5 at.% Zr at 1000 K, and (c) 9 at.% Zr at 1000 K.  In the panels on the left, Ni atoms are colored red and Zr atoms are colored blue.  In the panels on the right, fcc atoms are colored green, hcp atoms red, bcc atoms purple, icosahedral atoms yellow, and other atoms white.

## 2.5 Conclusions

In this work, we have identified the key characteristics of interatomic potentials which are able to accurately recreate interfacial segregation and complexion transitions.  Four interatomic potentials were tested on their ability to recreate key experimental observations in the Cu-Zr alloy.  Based on these results, the following conclusions can be made:

•       Zr atoms segregate to Cu grain boundaries, eventually leading a transformation to nanoscale amorphous complexions as doping concentration and temperature increase.

- The ZJW potential underestimates the segregation tendency of Zr, while the WAFW potential captures the segregation of Zr but produces an erroneous clustering of Zr atoms in the boundary. In contrast, both the CSM potential and the MKOSYP potential are able to produce simulation results which mimic experimental observations.

- Accurate modeling of interfacial segregation and structural transitions requires the reproduction of physical quantities such as enthalpy of mixing and bond energies. To obtain precise values of these parameters, experimental or first-principles data from multiple phases and material states should be included in the fitting database used to create the cross-potential terms.

- Accurate simulations can also be performed on the Ni-Zr system, which demonstrates a more subtle tendency for grain boundary segregation of Zr but the ability to form AIFs.

By understanding what features are needed for accurate modeling of interfacial phenomena, this work opens the door for further materials discovery. Alloys of interest can be tested in simple bicrystal models prior to experimentation, to identify promising material combinations that can sustain disordered complexions.

# Chapter 3 Interfacial segregation and structural transition in ternary alloys

## *3.1 Introduction*

AIFs have been proven to toughen nanocrystalline Cu both experimentally and theoretically [26, 29, 31-33], Pan and Rupert even showed that this toughening effect might be maximized by forming thicker films [33]. While current efforts are put in exploring binary alloys, we postulate that thicker AIFs can be formed in certain multi-element systems with more than one solute element segregating to the grain boundary. In this chapter, the results for two model ternary alloys, Cu-Zr-Ag and Al-Zr-Cu are shown with the hope of discovering general rules that can be applicable to other multi-component alloys. Previous studies reported dopant segregation in Cu-Zr, Cu-Ag, Al-Zr and Al-Cu alloys and the ability of Zr and Ag to amorphize Cu grain boundaries, so it is expected that the same behaviors will be achieved in ternary alloys containing these elements. The aforementioned binaries also differ from each other in aspects such as the atomic radius mismatch between solute and solvent atoms, and the enthalpy of mixing. All these factors, as well as the interaction between different solute elements, contribute to a more complex interfacial phenomenon of the ternary alloys. With the goal of determining the possibility of forming thicker AIFs, different doping concentrations are tested which covers a wide range of alloys.

## *3.2 Computational Methods*

The simulation model is similar to what is shown in last chapter, except that the clean grain boundary structure in Al simulated by the Al-Zr-Cu ternary potential at 0 K is

asymmetric as is presented in Fig. 3.1 below. This asymmetric structure is truly more stable than the symmetric version, as the calculated 0 K grain boundary energy of the asymmetric structure (460.63 mJ/m$^2$) is lower than the symmetric structure (464.75 mJ/m$^2$). However, this asymmetric structure is not stable at finite temperature and for the doped grain boundary which will be shown later. The two ternary interatomic potentials used in this work were constructed by the force-matching method and validated by calculating the liquid enthalpy of mixing.
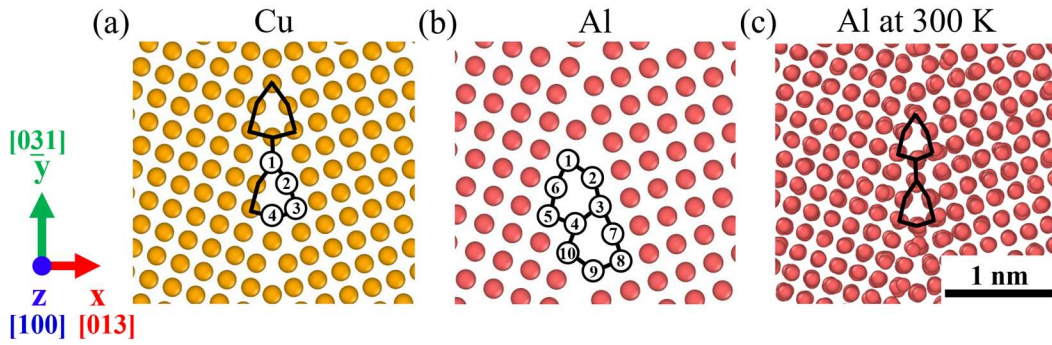


Fig. 3.1 A Σ5 (310) grain boundary in (a) pure Cu, (b) pure Al (i.e. a clean grain boundary), and (c) pure Al at 300 K. The repeating kite-shape structure unit is outlined by black lines and certain sites are numbered for the calculation of segregation energy of solute to different positions at the grain boundary.

The Cu-Zr-Ag and Al-Zr-Cu alloy were chosen for this study for a number of reasons. First, there is evidence that all of the added dopants will segregate to the interfaces, such as the segregation of Zr [29, 31, 32] and Ag [25, 30] to grain boundaries in Cu-based alloys, and that of Cu [115-117] in Al-based alloys. Similarly, Tsivoulas and Robson [118] observed Zr enrichment along dislocations, followed by Al$_3$Zr precipitation in the as-cast and fully homogenised Al-Cu-Li based alloys. Second, Zr [29, 31, 32] and Ag [25, 30] addition by

themselves have been reported to facilitate AIF formation in the Cu-Ag and Cu-Zr binary systems. Therefore, the Cu-Zr-Ag alloy is a clear candidate to explore the effect of a shift to ternary chemical compositions. Although there are no direct studies about AIF formation in binary Al-Cu and Al-Zr, researchers have investigated the glass forming ability of binary metallic glasses with these chemical compositions, as well as the ternary Al-Zr-Cu system [119-121]. For example, Yan et al. [120] managed to obtain a stable amorphous phase in Al-Cu for an Al concentration range of 64-74 at.%. While these two ternary systems are selected to observe both interfacial segregation and AIF formation, they do differ from each other when considering other aspects such as the atomic radius mismatch and enthalpy of mixing. For the Cu-Zr-Ag system, the atomic sizes of Zr and Ag are 25% and 12.5% larger than Cu, respectively. Atomic size mismatches of >12% have historically aided metallic glass formation [108]. For the Al-Zr-Cu system, the atomic size of Zr is 11.9% larger than Al while that of Cu is 10.5% smaller than Al, respectively. Cu-Zr, Al-Zr and Al-Cu all have negative enthalpies of mixing, while Cu-Ag has a positive enthalpy of mixing. A negative enthalpy of mixing is typically required for a good glass former [108].

### 3.3 Results and Discussion

### 3.3.1 Segregation and structural transitions in binary systems

The simulated interfacial segregation and structural transition in individual binary alloys are first presented as a baseline for comparison. The chemical information (left frames) and structural information (right frames) of doped grain boundaries in the Cu-Zr, Cu-Ag, Al-Cu and Al-Zr systems are shown in Fig. 3.2. In this figure, the chemical information is shown in the frames on the left of each figure part, while the structural information is

presented in the frames on the right. Atomic snapshots of samples simulated at 350 K (Al-rich alloys) or 600 K (Cu-rich alloys) and with 0.4 at.% or 1 at.% dopant concentration are presented to display representative examples of ordered grain boundaries. Additional samples simulated at higher temperatures of 350 K (Al-rich alloys) or 600 K (Cu-rich alloys) and with larger dopant concentrations are chosen to show representative examples of conditions that are conducive to AIF formation. Interfacial segregation of dopants occurs in all four binary systems, but the structural transition at the grain boundaries is quite different. In the Cu-Zr and Cu-Ag alloy with ordered grain boundaries, the segregating dopants prefer to occupy the kite-tip sites (site 1 in Fig. 3.1(a)) and form what can be classified as a monolayer complexion at the grain boundary. At high temperature and doping concentration, AIFs form in both alloys.

For Al-Cu with ordered grain boundaries (Fig. 3.2(e)), a variety of grain boundary sites are occupied. Some Cu atoms are found at site 4 (the bottom of the kite unit), while others are found along the edges of the kite unit. Finally, some dopants become interstitials that occupy the empty space in a kite-shape structure. An AIF that is both structurally and chemically disordered forms in the sample doped by 9 at.% Cu at 600 K. For the Al-Zr system, the grain boundary remains ordered even as the global Zr concentration reaches 10 at.% and the temperature reached 600 K. As mentioned previously, researchers who observed Zr segregation to dislocations in Al-based alloys found $Al_3Zr$ precipitates at dislocations, not amorphous phases, meaning that Zr atoms prefer to stay in ordered, crystalline phases when added to Al [118]. The lack of an AIF in Al-Zr suggests that the energy penalty for forming an amorphous complexion is simply too large to make it energetically favorable, even when heavily doped at high temperatures.

**(a)** Cu-Zr (0.4 at.% Zr) at 600 K
**(b)** Cu-Zr (4 at.% Zr) at 1000 K
**(c)** Cu-Ag (0.4 at.% Ag) at 600 K
**(d)** Cu-Ag (5 at.% Ag) at 1000 K
**(e)** Al-Cu (0.4 at.% Cu) at 350 K
**(f)** Al-Cu (9 at.% Cu) at 600 K
**(g)** Al-Zr (1 at.% Zr) at 350 K
**(h)** Al-Zr (10 at.% Zr) at 600 K
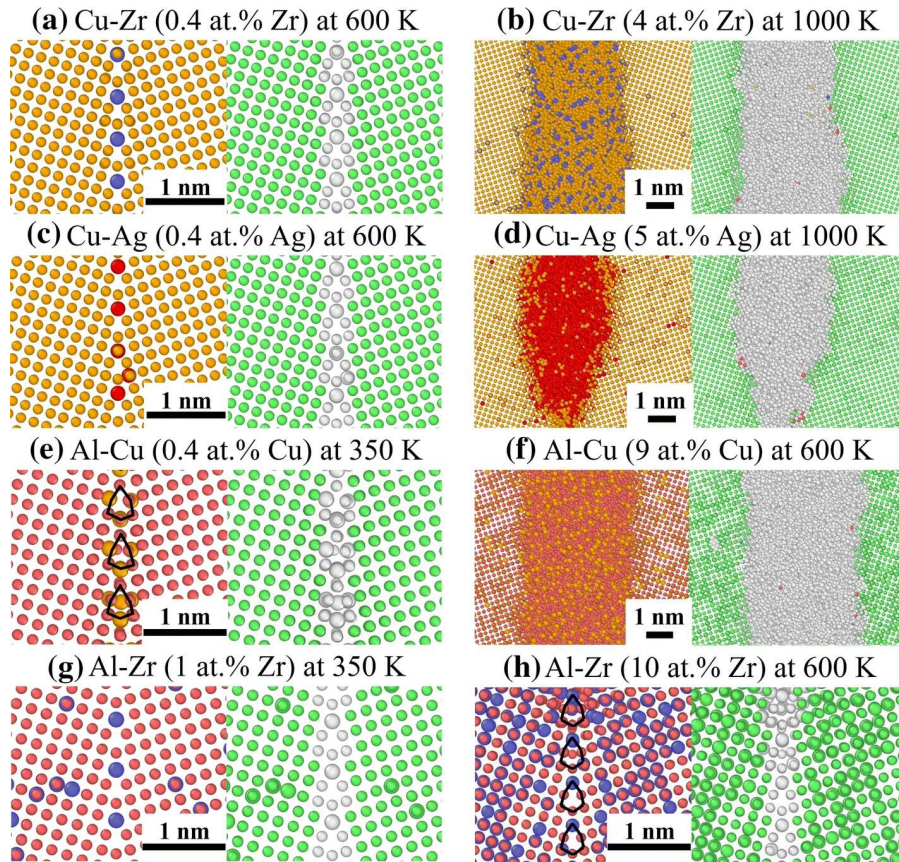
Fig. 3.2 The chemical (left frame) and structural (right frame) information of the Σ5 (013) grain boundary in Cu doped with (a) 0.4 at.% Zr at 600 K, (b) 4 at.% Zr at 1000 K, (c) 0.4 at.% Ag at 600 K, and (d) 5 at.% Zr at 1000 K, as well as the Σ5 (013) grain boundary in Al doped with (e) 0.4 at.% Cu at 350 K, (f) 9 at.% Cu at 600 K, g 1 at.% Zr at 350 K, and (h) 10 at.% Zr at 600 K. In the left panels, Cu atoms are colored orange, Ag atoms are colored red, Zr atoms are colored blue, and Al atoms are colored pink. In the right panels, fcc atoms are colored green, hcp atoms are colored red, bcc atoms are colored purple, icosahedral atoms are colored yellow, and "other" atoms are colored white. The atomic radii of dopants are set slightly larger than that of the matrix element to show them more clearly. The kite-shape structure at the grain boundary is outlined by black lines in (e) and (h).

It is useful to compare the segregation tendency of different dopants by calculating the segregation energy, $\Delta H_{seg}$, of a single dopant at various sites at the grain boundary. The segregation energy is defined as the difference in energy between a material system with solutes at the grain boundary and a system with the same amount of solutes in the grain interior. A negative value of segregation energy indicates the preference of segregating to the grain boundary while a positive value means depletion from the grain boundary. The equation used for calculating the segregation energy is shown below [122],

$$\Delta H_{seg}\left(\sum N_i\right) = \frac{\left(H\left(\sum N_i\right) - H(0) - \sum N_i \Delta H_{i,bulk}\right)}{\sum N_i} \tag{3}$$

where $\Delta H_{seg}(\sum N_i)$ is the segregation energy per solute for a bicrystalline sample containing $\sum N_i$ dopants, $H(\sum N_i)$ is the energy of a bicrystalline sample containing $\sum N_i$ dopants, $\Delta H_{i,bulk}$ is the change in energy when inserting one dopant $i$ in the bulk system. The segregation energy of solutes as a function of distance from grain boundaries is shown in Fig. 3.3, and that as a function of spatial position projected onto the (100) plane. The promising segregation sites for each dopant is circled in blue. The results show that for Cu grain boundaries, the most advantageous segregation site for both Zr and Ag is site 1 which is the kite-tip. Since the segregation energy of Zr is more negative than that of Ag, Zr has a higher segregation tendency in Cu-based alloys (-1.3 eV for Zr and -0.53 eV for Ag, a DFT calculation result is -1.62 eV [123]). Another promising site for Zr and Ag is site 3 which is right next to the kite-bottom. For Al grain boundaries, since the grain boundary structure is symmetric at finite temperatures, the trend of dopant segregation will be the same as what is shown for the symmetric Cu grain boundary. The distribution of the dopant segregation energy is consistent with the distribution of the hydrostatic stresses in the vicinity of grain boundaries,

with the atoms larger than the host element preferring sites under tension while atoms smaller than the host element preferring sites that are compressed.
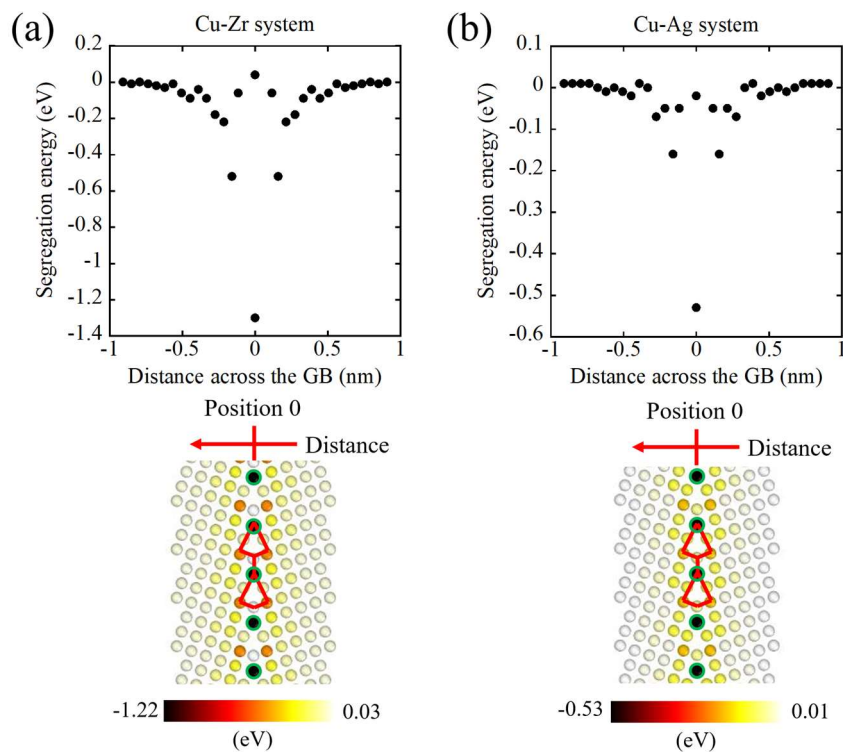


Fig. 3.3 The spatial dependence of the segregation enthalpy of (a) Zr, (b) Ag in Cu across the grain boundary (top frames). The images below each figure provide a reference for how distance across the grain boundary is measured. A positive value of segregation enthalpy indicates depletion from the grain boundary, while a negative value indicates segregation of dopant to the grain boundary. In the bottom frames, the kite-shape structure at the grain boundary is outlined by red lines, and the promising segregation sites of each solute is outlined by blue circles.

### 3.3.2 Segregation and structural transitions in ternary systems

At low temperature and low dopant concentration, ordered grain boundaries were found in both Cu-Zr-Ag and Al-Zr-Cu. Chemical and structural snapshots of representative

ordered grain boundaries, as well as their solute concentration profiles and the Gibbsian interfacial excesses are shown in Fig. 3.4. The Gibbsian interfacial excess of solutes describes the total solute excess per unit area and is defined as [124]:

$$\Gamma = \frac{N_{GB}(c_{GB} - c_0)}{A}$$  (4)

where $N_{GB}$ is the number of atoms in the grain boundary region, $c_{GB}$ is the grain boundary composition, $c_0$ is the grain interior composition, and $A$ is the interfacial area. Fig. 3.4(a) shows that the boundary in the Cu-Zr-Ag alloy has ordered grain boundaries characterized by Zr atoms at the kite-tip sites (site 1), while no Ag atoms can be found at these sites that were most promising in the binary Cu-Ag. Instead, the Ag atoms must be incorporated as a solid solution into the lattice. Fig. 3.4(c) demonstrates this effect in a more quantitative manner, where a drop in the Ag concentration at the grain boundary is found while there is a sudden increase of the Zr concentration. The total dopant concentration matches the Zr concentration in the grain boundary, but is determined by the Ag concentration in the grain interior. Since Zr interfacial segregation leads to the formation of a monolayer complexion at the grain boundary, meaning that all the Zr atoms are located along one atomic plane, the increase of Zr concentration is very sharp and is within a small region. Fig. 3.4(e) presents the Gibbsian interfacial excess in the ternary Cu-based alloys and shows a similar trend, with the curve for Ag having a small negative value at the interface. Taken as a whole, these figures show that, although Zr and Ag would like to segregate to the same promising segregation sites, Zr wins out and fills them first. This observation is consistent with our calculation of lower segregation energy in absolute terms for Zr in Cu, as compared to Ag in Cu.

On the contrary, Zr and Cu occupy different sites at grain boundaries in Al-Zr-Cu, as shown in Fig. 3.4(b). From Fig. 3.4(d) and Fig. 3.4(f), the concentrations of both Zr and Cu peak in the grain boundary, signaling the co-segregation of Cu and Zr. Since the two types of dopants prefer different sites, they do not compete and the grain boundary can be much more heavily doped. This can be seen by observing that the maximum grain boundary dopant concentration in Al-Zr-Cu is more than twice as large as that in the Cu-Zr-Ag alloy (~40 at.% versus ~17 at.%, respectively). This suggests that careful selection of dopant elements is important when planning for segregation engineering. For example, if one wants to maximize the grain boundary doping to reduce boundary energy and limit grain growth, a synergistic type of doping would be targeted.



43
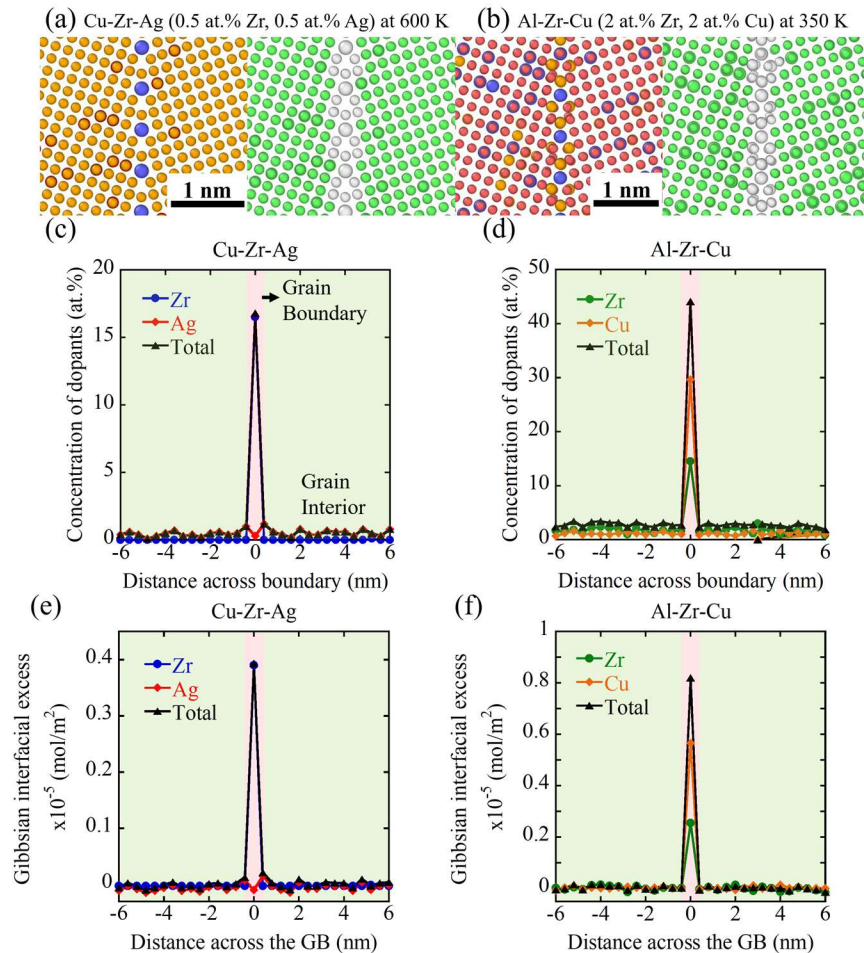
Fig. 3.4 The chemical (left frame) and structural (right frame) information of the Σ5 (013) grain boundary in Cu doped with (a) 0.5 at.% Zr and 0.5 at.% Ag at 600 K, (b) 2 at.% Zr and 2 at.% Cu at 350 K. In the left panels, Cu atoms are colored orange, Ag atoms are colored red, Zr atoms are colored blue, and Al atoms are colored pink. In the right panels, fcc atoms are colored green and other atoms are colored white. The concentration profile of dopants across the grain boundary for (c) Cu-0.5 at.% Zr-0.5 at.% Ag and (d) Al-2 at.% Zr-2 at.% Cu. The Gibbsian interfacial excess profile of solutes across the grain boundary for (e) Cu-0.5 at.% Zr-0.5 at.% Ag and (f) Al-2 at.% Zr-2 at.% Cu. In (c)-(f), the light green regions are the grain interiors and the light red regions are the grain boundaries.

At high temperature and dopant concentration, AIFs form in both ternary systems. Chemical and structural snapshots of representative amorphous grain boundary films, as well as their solute concentration profiles and the Gibbsian interfacial excesses are shown in Fig. 3.5. Both alloys form structurally and chemically disordered amorphous films, but the AIF in Al-Zr-Cu contains only a small amount of Zr. Fig. 3.5(c), presents the total dopant concentration in Cu-2 at.% Zr-2 at.% Ag, where both Zr and Ag concentrations increase in the grain boundary region, indicating co-segregation. Unlike the competition for limited segregation sites in the ordered grain boundary which leads to the depletion of Ag, there are many more possible segregation sites generated after the formation of an AIF. Because of this, Ag also has a chance to segregate to grain boundaries. In the Al-5 at.% Zr-5 at.% Cu system shown in Fig. 3.5(d), the concentration of Cu reaches its highest value in the grain boundary, but there is a drop in Zr concentration. Since the two dopants had no trouble being close to each other in the ordered boundary, it is unlikely that the reduced Zr is caused

by a chemical repulsion of the two dopants. A more likely explanation is that there is simply an energetic penalty associated with Zr in an amorphous structure here, which was why AIFs did not form in the binary Al-Zr alloy. The curves in Fig. 3.5(e) and Fig. 3.5(f) show the Gibbsian interfacial excess of dopants, which have similar shapes to the chemical concentration curves in Fig. 3.5(c) and Fig. 3.5(d). In Fig. 3.5 (f), there is a range of negative Gibbsian interfacial excess for Zr at the grain boundary, again signaling depletion of Zr.
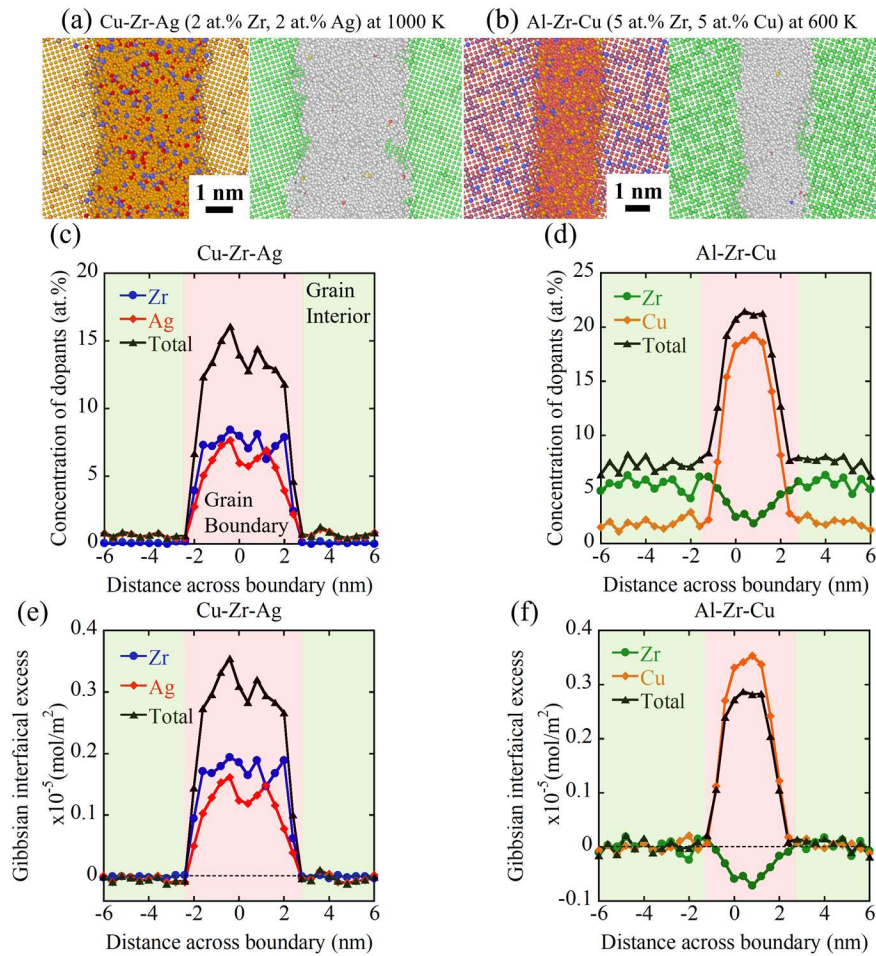


Fig. 3.5 The chemical (left frame) and structural (right frame) information of the Σ5 (013) grain boundary in Cu doped with (a) 2 at.% Zr and 2 at.% Ag at 1000 K, (b) 5 at.% Zr and 5 at.% Cu at 600 K. In the left panels, Cu atoms are colored orange, Ag atoms are colored red, Zr atoms are colored blue, and Al atoms are colored pink. In the right panels, fcc atoms are

colored green, hcp atoms are colored red, bcc atoms are colored purple, icosahedral atoms are colored yellow, and other atoms are colored white. The concentration profile of dopants across the grain boundary for (c) Cu-2 at.% Zr-2 at.% Ag and (d) Al-5 at.% Zr-5 at.% Cu. The Gibbsian interfacial excess profile of dopants across the grain boundary for (e) Cu-2 at.% Zr-2 at.% Ag and (f) Al-5 at.% Zr-5 at.% Cu. In (c)-(f), the light green regions are the grain interiors and the light red regions are the grain boundaries.

### 3.3.3 Forming thicker amorphous intergranular films in ternary alloys

Pan and Rupert reported that AIFs can improve ductility by delaying crack nucleation and slowing down crack propagation, with this effect increasing as film thickness increases [33]. Thus, a question of great practical importance is whether a ternary alloy can sustain thicker AIFs. Fig. 3.6 presents the grain boundary thickness as a function of the total dopant concentration for both ternary and binary Cu-based and Al-based alloys. Again, we hold the concentration ratio of different types of dopants in the ternary systems as 1:1 for simplicity, with all the simulations were performed at 600 K for Al-based alloys and 1000 K for Cu-based alloys. Fig. 3.6(a) and Fig. 3.6(c) show that the ternary curves lie between the curves for the two related binary systems. The Cu-Zr and Al-Cu systems have the thickest AIFs for a given total dopant concentration. Cu-Ag forms AIFs but they are relatively thin, which can be explained by the clustering of Ag caused by the positive enthalpy. A second caveat exists for the Cu-Ag system. The prior work showing that AIFs can delay crack nucleation and propagation focused on amorphous films which were chemically disordered (i.e., like the films in Cu-Zr and Al-Cu). It is not obvious whether structurally disordered but chemically ordered films such as those in Cu-Ag would be beneficial or mechanical properties. Finally,

46

Al-Zr cannot sustain AIFs, so the grain boundary thickness remains small. Interestingly, the curve for Al-Zr in Fig. 3.6(c) shows a modest decrease from the pure Al grain boundary thickness. In this case, the "thickness" only comes from thermal fluctuations. Zr segregates to the grain boundary in Al, reduces the amount of thermal fluctuation, and hence the grain boundary is more ordered. Fig. 3.6(b) and Fig. 3.6(d) isolate the ternary alloys and compare them with the binary that is better able to sustain AIFs (Cu-Zr and Al-Cu), while keeping the amount of Zr and Cu constant. In this case, we are asking when AIFs are the thickest for a given amount of Zr or Cu in the system. This could be important if a given amount of one dopant is limit (e.g., if >X at.% Zr led to precipitation of an intermetallic phase). These figures show that the curves for ternary systems are above the curves for the two binary systems, showing that ternary compositions may still be useful in certain situations.
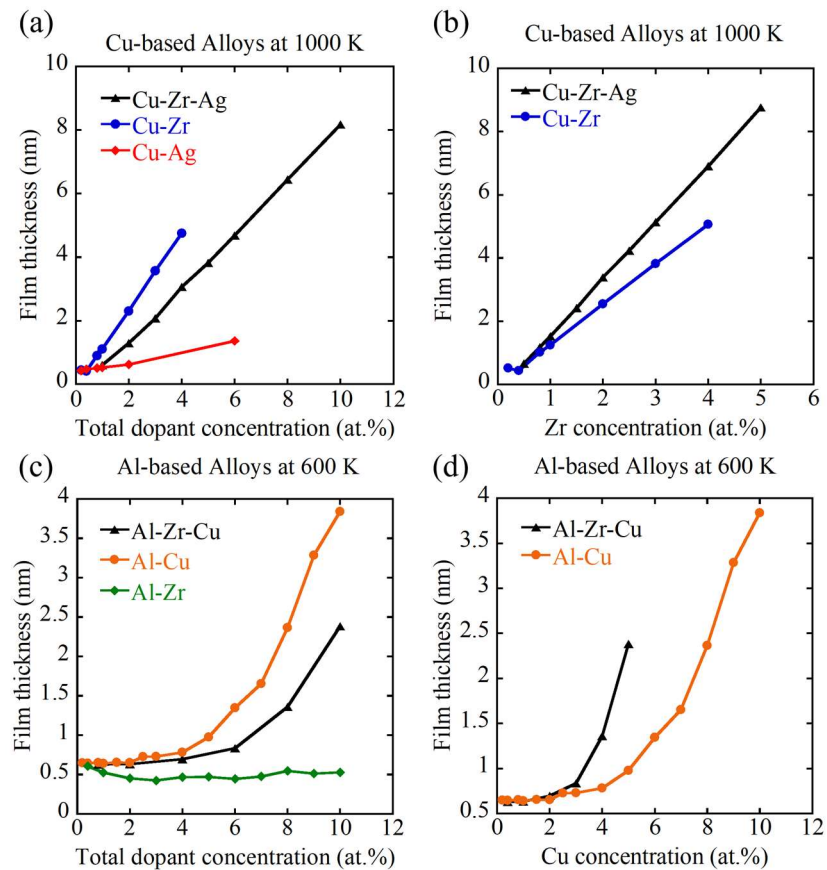
Fig. 3.6 The variation of film thickness with increasing total dopant concentration for (a) Cu-Zr, Cu-Ag, and Cu-Zr-Ag, as well as film thickness as a function of Zr concentration for (b) Cu-Zr and Cu-Zr-Ag.  The variation of film thickness with increasing total dopant concentration for (c) Al-Zr, Al-Cu, and Al-Zr-Cu, as well as film thickness as a function of Cu concentration for (d) Al-Cu and Al-Zr-Cu.

As a final test of the ability of these ternary alloys to form AIFs, we relax the restriction on the concentration ratio of the different dopants.  It is possible that there is a promising concentration ratio that allows ternary systems to form thicker AIFs than the binaries for a given amount of total dopant.  The metallic glass literature is filled with examples of alloys where the best glass forming composition is not an even distribution between the constituent elements [121, 125-127].  To explore this, we fix the total amount of dopant to a given value while changing the concentration ratio of the two dopants in a ternary.  For the Cu-Zr-Ag system with a total concentration of 4 at.% total dopant, the film thickness is presented in Fig. 3.7(a) as a function of the Ag concentration.  This means that Cu-Zr appears on the plot at 0 at.% and Cu-Ag appears on the plot at 4 at.%, with ternary alloys in between. For this system, we find that the thickness simply moves between the two bounds.  The film thickness versus Cu concentration for Al-Zr-Cu with 10 at.% total dopant is shown in Fig. 3.7(b), with 0 at.% indicating the Al-Zr binary system and 10 at.% indicating the Al-Cu binary system.  In this case, we do find that the ternary can more efficiently produce AIFs, as the thickest AIF is found in a ternary composition (Al-9.5 at.% Zr-0.5 at.% Cu).  While the ternary AIFs only appear to be slightly thicker, it is important to put this number in perspective, as they are 3.95% thicker than the AIFs in Al-Cu.  This observation proves that ternary

compositions can in fact lead to thicker AIFs compared to binary alloys in certain situations. It is worth noting that we observe this behavior even though one of the two binaries was a relatively poor glass former, as shown by the fact that Al-Zr did not amorphize at all. Future work should likely focus on combinations where all alloy combinations are good glass formers in their binary combinations.
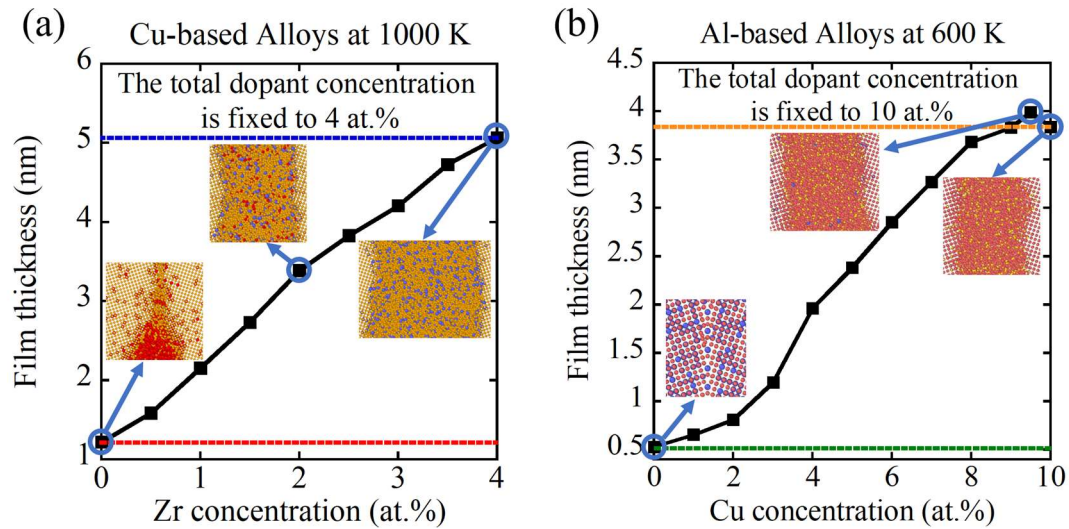


Fig. 3.7 (a) The film thickness as a function of Ag concentration for Cu-Zr-Ag. The total dopant concentration is fixed as 4 at.%, meaning the system with 0 at.% Ag is the Cu-Zr binary (blue dashed line) while the system with 4 at.% Ag is the Cu-Ag binary (red dashed line). The insets show the atomic structures of the grain boundary in the Cu-Zr, Cu-Ag, and Cu-2 at.% Zr-2 at.% Ag. (b) The film thickness as a function of Cu concentration for Al-Zr-Cu alloys. The total dopant concentration is fixed as 10 at.%, meaning the system with 0 at.% Cu is the Al-Zr binary (green dashed line) while the system with 10 at.% Cu is the Al-Cu binary (orange dashed line). The insets show the atomic structures of the grain boundary in the Al-Zr, Al-Cu, and Al-0.5 at.% Zr-9.5 at.% Cu.

### 3.4 Conclusions

In this paper, atomistic simulations were performed to study Cu-Zr-Ag and Al-Zr-Cu ternary alloys about the solute behaviors in interfacial segregation and amorphous complexion formation. A bicrystal sample with two $\Sigma5$ (310) grain boundaries is used as a model to represent a high-angle and high-energy tilt grain boundary. The following conclusions can be drawn from this work:

- In Cu-Zr-Ag, the preferred segregation site for both Zr and Ag is the kite-tip site, which leads to a local depletion of Ag at the grain boundary in the ternary alloys with ordered grain boundaries. In contrast, for Al-Zr-Cu, Zr and Cu have different preferred segregation sites, they therefore have a synergistic doping pattern. As a consequence, much higher grain boundary dopant concentrations are achieved in Al-Zr-Cu.

- The segregation patterns in the ordered grain boundaries for these alloys can be explained by mechanical effects, where the local hydrostatic stress and relative atomic size determines site preference.

- The interaction between dopants affects their segregation behavior, with an attraction enhancing the extent of total dopant segregation while a repulsion decreases the segregation tendency.

- By controlling the concentration ratio of different dopant elements, it is possible to form thicker AIFs in some ternary alloys. Alternatively, if only a limited amount of a given dopant can be added, a ternary composition can be a way to enable further grain boundary segregation and thickening of AIFs. In nanocrystalline metals where such AIFs can improve ductility, our results suggest that ternary compositions should be explored.

# CHAPTER 4: Disconnection-mediated boundary migration in pure Mg

## 4.1 Introduction

While deformation twinning in hexagonal close-packed metals has been widely studied due to its substantial impact on mechanical properties, an understanding of the detailed atomic processes associated with twin embryo growth is still lacking. However, as the early stages of the twinning process, the growth of twin embryos should place a huge influence on the final morphology of mature twins. It is therefore a critical need for a comprehensive model of twin embryo growth. In this chapter, we aim to provide the missing piece for a full picture of the twinning process in pure Mg. MD simulations are first performed to obtain atomistic growth mechanisms for twin embryos. Then, a phenomenological model, which unifies the motion of twinning disconnections and twin tip propagation, is proposed to provide a quantitative analysis of twin embryo growth. The power of the phenomenological model is that it can describe twin embryo growth at a larger length-scale and provide data that can be compared or connected to experimental results. In the end, the recent work of Yu et al. [128] on twin growth in a nanoscale single crystal is chosen to validate the MD simulation as well as the robustness of the phenomenological model.

## 4.2 Computational Methods

To study the atomic scale mechanisms responsible for twin embryo growth, we first perform MD simulations using the Modified Embedded-Atom Method (MEAM) potential developed by Wu et al. that was constructed to accurately model the plastic deformation and fracture of Mg [129]. Atoms are relaxed under an NVT ensemble at 1 K or 300 K using Nose-Hoover thermostat, with the temperature adjusted every 500 time steps with one integration

step of 0.1 fs. The low temperature simulations at 1 K are used to inhibit any effect of thermal fluctuations on twin growth, making it easier to identify the key deformation mechanisms. The simulations conducted at 300 K are used to compare with the experimental results on twinning in nanoscale Mg single crystals [128]. Structural analysis and visualization of atomic configurations are performed using the open-source visualization tool OVITO [130]. The Polyhedral Template Matching (PTM) method [131] is used to characterize the local crystalline structure and orientation associated with each atom in the system. Mg atoms with an hcp structural environment are colored blue, while those with any other structural environments are colored white.

A schematic of the simulation cell is shown in Fig. 4.1, with the X-axis along the $[1\bar{2}10]$ direction, the Y-axis along the twinning direction $[10\bar{1}1]$, and the Z-axis perpendicular to the $(\bar{1}012)$ plane (approximately parallel to the $[10\bar{1}\bar{m}]$ direction with m = 1.139, as reported by Ostapovets and Gröger [69]). The dimensions of the simulation box are $5.15 \times 76.8 \times 55$ nm$^3$ in the X, Y, and Z directions, respectively, and the sample contains ~950,000 atoms. The dimensions along the Y and Z directions are chosen to minimize interactions between the twin embryo and the fixed-atom region, as well as interactions between the twin embryo and its periodic image. One twin embryo with a length of 7.0 nm ($l_0$, the initial length of the twin embryo) and a thickness of 4.3 nm ($h_0$, the initial thickness of the twin embryo) is inserted at the center of a simulation box containing the perfect Mg crystal lattice, using the Eshelby method reported by Xu et al. [132]. The ratio of the initial embryo length to the initial embryo thickness is 1.6. To test the effect of initial shape and size on the twin embryo growth process, the simulations are repeated using two other initial twin embryo sizes with different

52

aspect ratios: (1) length $l_0$ = 8.2 nm and thickness $h_0$ = 7.5 nm ($l_0/h_0 \approx$ 1.1), and the other with $l_0$ = 15.4 nm and $h_0$ = 4.1 nm ($l_0/h_0 \approx$ 3.7).
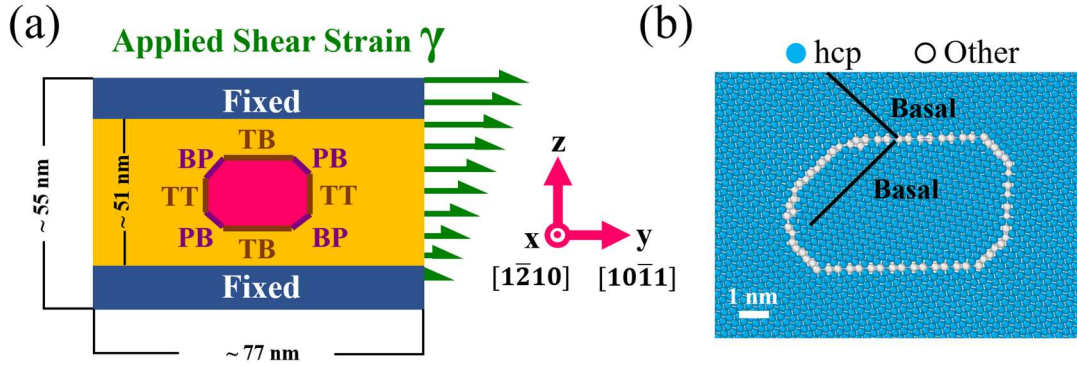


Fig. 4.1 (a) A schematic of the shear deformation simulation, and (b) an atomic snapshot of the initial twin embryo. In (b), hcp atoms are colored blue, while atoms at the boundaries are colored white due to their local structure. The different interfaces associated with the twin embryo are designated in (a). Shear strains are applied by displacing all atoms in the simulation cell, as it is shown by the green arrows in (a) which denote the displacement at a given height within the sample. The basal planes in the matrix and the twin are shown in (b) using solid black lines.

The following procedure for twin embryo insertion was used. First, a piece of the initial Mg lattice bound by two conjugate twinning planes in the $\{10\bar{1}2\}$ plane family is extracted (the horizontal twinning plane is the $(\bar{1}012)$ plane and the one almost perpendicular to it is the $(10\bar{1}2)$ plane). Then a twinned region is obtained by applying mirror symmetry to the extracted region, which is subsequently introduced into the lattice. The shape of the twinned region is slightly different from the shape of the extracted region of the initial lattice. In order to match the shape of these two regions, a shear is applied to the twinned region. Finally, the sample is structurally relaxed using energy minimization. If there are no shear strains

applied to the sample, the twin embryo is not stable and will shrink until it disappears due to the local stress profile. Therefore, shear strains are applied parallel to the $(\bar{1}012)$ planes in the $[10\bar{1}1]$-direction to stabilize the twin embryo. The minimum shear strain which can stabilize the twin embryo is around 5%. For the following shear simulation, the whole simulation box is first shear back to a non-strain state, and then deformed at a certain strain level. The twin embryo obtained after energy minimization is bound by a series of connected TBs, conjugate TBs, and BP/PB interfaces. Specifically, the upper and lower plane is the $(\bar{1}012)$ twinning plane (referred to simply as "TBs" from now on, as these defects would be the only TBs remaining once the twin embryo has matured), while the vertical planes are the $(10\bar{1}2)$ twinning planes (these are the twin tips, so they are referred to simply as "TTs" from now on). The two twinning planes are connected by BP and PB interfaces. Various morphologies of TTs of the $\{10\bar{1}2\}$ twins have been reported in prior literature [91, 92, 133, 134]. The TTs can either be comprised of BP/PB interfaces only [91, 92], or be made of planes which are perpendicular to primary twinning planes, such as planes contain interfacial dislocations and are separated by BP/PB interfaces [133, 134]. In our simulations, the initial TTs are defect free.

Periodic boundary conditions are applied in the X- and Y-directions, while the top and bottom surfaces in the Z-direction are free surfaces. Shear strains are applied uniformly by displacing all atoms in the simulation box. To maintain a constant shear strain, atoms within a 2 nm thick band at the top and bottom of the box are fixed, while the rest of atoms are free to move. The thickness of the fixed region is chosen to be above the cutoff distance of the interatomic potential to ensure that the evolving atoms see the fixed strain condition, not the free surface on top and bottom. The motivation behind this type of loading is to provide a

constant driving force for twin embryo growth, by putting the matrix into a state where shear stress is available to drive growth. The expected driving force (the matrix stress) can be obtained by finding the shear stress in a single crystal with the matrix configuration. The overall or global shear stress in the combined matrix-twin embryo sample will decrease as the system evolves and the twin fraction grows, but the assumption of a constant matrix stress is reasonable for the conditions studied here. Shear strains ranging from 6% to 10% are used, so that the lowest shear strain can activate twin embryo growth during MD timescales, yet the highest shear strain would not lead to rampant twin embryo growth such that there is an interaction with the fixed-atom regions and its periodic images.

To quantify the growth of the twin embryo, its length is calculated as the difference between the positions of the two TTs, while its thickness is calculated as the difference between the positions of the upper and lower TBs. To determine the positions of the TBs and TTs at any given moment, the atoms in the twinned region should be correctly identified first via the orientation information of each atom. The PTM method implemented in OVITO gives a point-to-point correspondence between the template structures and the structures to be analyzed, by minimizing the root-mean-square deviation of atom positions from the templates and simulated structures [131]. The lattice orientation information can be encoded as an orientation quaternion, $q = q_w + q_x i + q_y j + q_z k$. Component $q_w$ is the best to distinguish the twin embryo from the matrix, using a threshold value of $q_w = 0.8$. This criterion can be used for samples deformed at different strains and configurations taken at different times. To identify each boundary position, the simulation box is divided into 100 bins along the Y or Z-axis (displayed in Fig. 4.2), and then the number of atoms with $q_w > 0.8$ is counted in each bin and plotted versus the position of the bin. The peak in Fig. 4.2(c) then

represents the twin embryo. Since the number of atoms with $q_w > 0.8$ in each bin changes

with time as the twin grows, these values are normalized by the peak value in order to set

up a consistent criterion for twin identification. Finally, the full width at half maximum

values along the Y or Z-axis represents the positions of the TBs or TTs, respectively.
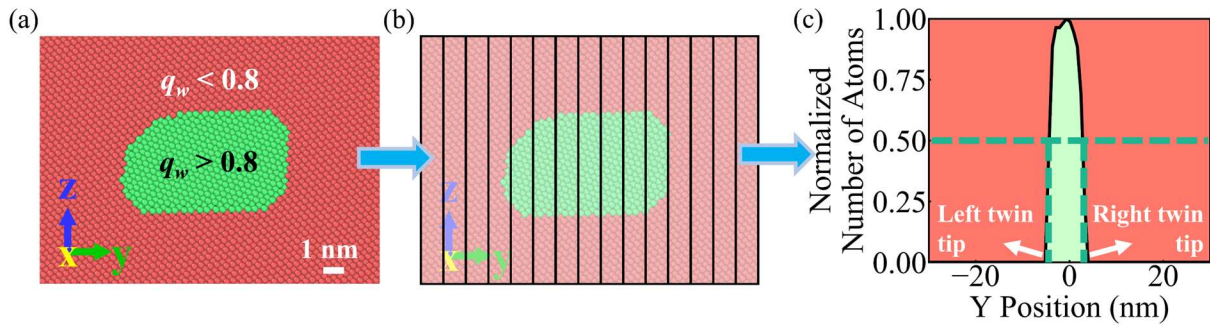


Fig. 4.2 Determining the positions of twin embryo boundaries. (a) The twinned region can

be accurately detected using lattice orientation information. The twin embryo is colored

green to contrast with the red matrix. (b) The simulation box is then divided into several

bins, and the number of atoms with $q_w$ larger than 0.8 in each bin is counted. (c) Next, these

numbers are normalized by their maximum value and plotted versus the positions of the

bins, where the peak represents the twinned region while the locations of boundaries are

chosen as the two positions with the Y-axis value equal to 0.5.

### 4.3 Results

### 4.3.1 Overall twin embryo growth

Atomistic simulations at 1 K were first used to reveal the atomic scale mechanisms

responsible for the expansion of a twin embryo under different applied shear strains. For

example, Fig. 4.3(a) shows the boundary atoms of the twin embryo in the sample deformed

under 7% shear strain, while Fig. 4.3(b) shows the corresponding boundary positions

extracted at different moments in time. The propagation of TTs is found to be faster than twin thickening, with a final twin length that is ~2.3 times larger than the twin thickness at the end of the simulation (32 ps). Fig. 4.3(b) shows a linear relationship between the TT position and time, which suggests the TTs move at a constant velocity. In contrast, TB motion slows down over time, indicating a decrease in the TB velocity.
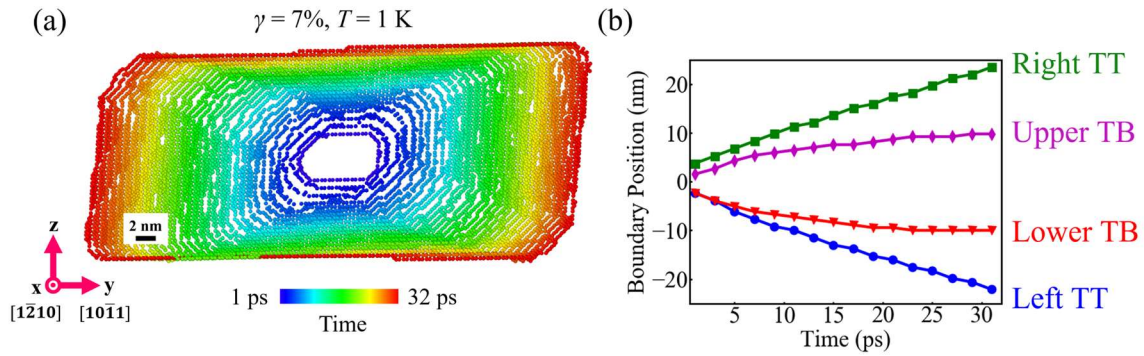


Fig. 4.3 Time evolution of the twin embryo at 7% shear strain and 1 K. (a) Boundary atoms of the twin embryo are colored by the time at which they are extracted. (b) The positions of boundaries versus time.

### 4.3.2 Twin boundary migration

Our MD simulations also show that most twinning disconnections form at the intersections of the TBs and BP/PB interfaces, and then propagate laterally to enable the growth of the twin embryo. An example is displayed in Fig. 4.4, where only the boundary atoms (white atoms) are shown and the hcp atoms in the matrix and twin are represented by the light blue background. In the first frame (8 ps) of Fig. 4.4(a), a twinning disconnection forms at the intersection on the right, followed by the formation of a second twinning disconnection at the intersection on the left in the second frame (9 ps). These two twinning disconnections move laterally towards each other in the second and third frames, similar to

observations of disconnection migration on twinning planes by Xu et al. [132], Ostapovets and Gröger [69], and El Kadiri et al. [55]. Because of this disconnection propagation, the upper TB eventually moves upward one step height. At the same time, the TTs migrate laterally as well, as shown by comparing the TT positions with the dashed black line denoting the position at 8 ps. The spatial distribution of atoms near the first twinning disconnection at 8 ps and 11 ps is displayed in Fig. 4.4(b), with pairs of atoms near each other denoting atoms at the two different times and the displacements between these atoms indicated by white arrows. The atoms, which were once in the matrix (red atoms) but joined the twin (green atoms) later, exhibit displacements in different directions, although there is a pattern with a repeating periodicity. Wang et al. [68] reported the movements of atoms in Zn samples containing even-layer-thick twins or odd-layer-thick twins of different thicknesses. Comparing their work with ours, it shows that the atomic displacements are not the same, although a shear strain parallel to the $\{10\bar{1}2\}$ plane is applied in both cases. However, only TBs exist in their simulations, while we have TBs, TTs, and PB/BP interfaces in our simulated twin embryos. Fig. 4.4(b) shows that most atomic displacements are a combination of horizontal displacements of atoms parallel to the twin planes and vertical displacements parallel to the TTs. A zoomed-in view of the atomic structure of a twinning disconnection is displayed in Fig. 4.4(c) with the Burgers vector and step character shown. The Burgers vector of a twinning disconnection is $b_t = \frac{1}{15}[10\bar{1}1]$ and the step height, $h_d$, is 0.38 nm. In Fig. 4.4(d), the distances traveled by several twinning disconnections, analyzed during the twin embryo growth, are plotted as a function of simulation time, showing linear trends for each twinning disconnection. The slopes of the dashed lines are very similar, indicating a

relatively constant velocity of the twinning disconnections for a given applied shear strain during the time period considered.
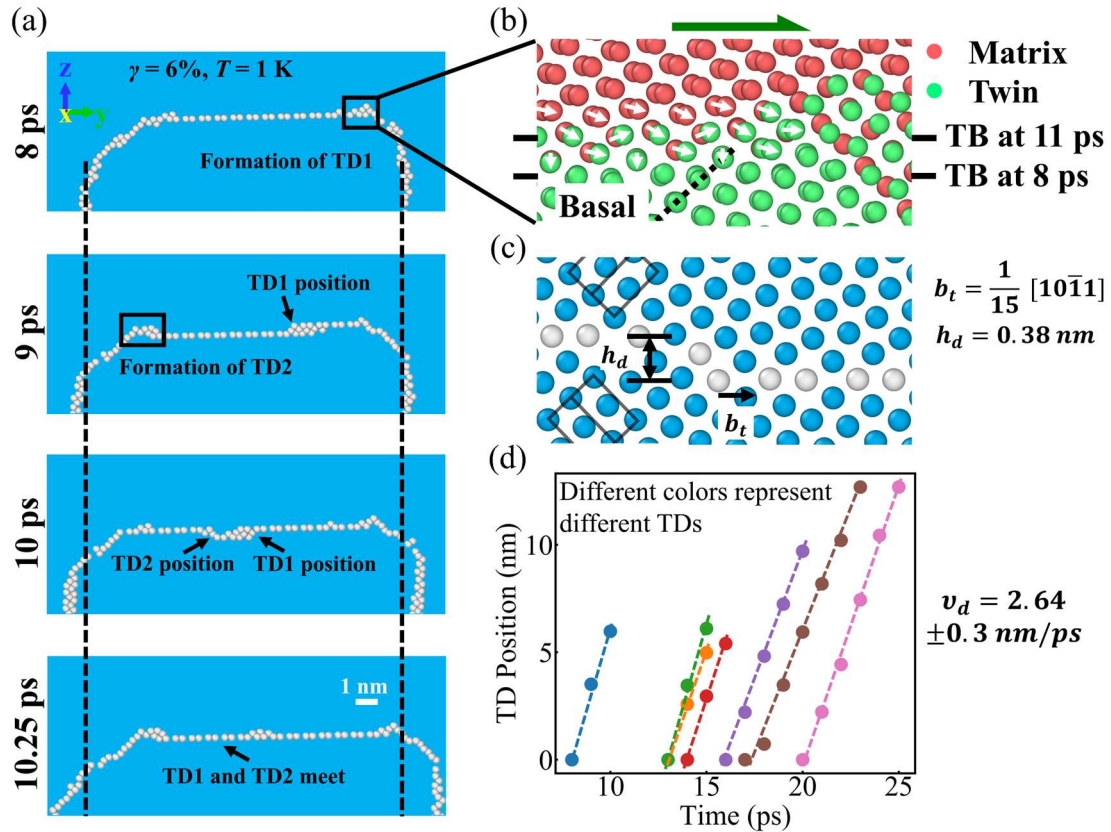


Fig. 4.4 (a) The nucleation and propagation of twinning disconnections on the upper TB in a sample deformed at 6% shear strain and 1 K. The positions of two twinning disconnections (TD1 and TD2) are marked in each frame. The dashed black lines represent the positions of TTs at 8 ps. (b) The spatial distribution of atoms near TD1 at 8 ps and 11 ps, where atoms in the matrix are colored red, while those in the twin embryo are colored green. The initial and new TBs are marked using solid black lines, while the dashed black line shows the basal plane in the twin. The white arrows indicate the atomic displacements. The dark green arrow on the top of the figure shows the direction of the applied shear strain. (c) The zoomed-in view of a twinning disconnection with its Burgers vector ($b_t$) and step character

($h_d$) shown, the outlines of two hcp cells are also drawn in the matrix and twin. The black arrow shows the Burgers vector of the twinning disconnection, the magnitude of which is very small. (d) The variation in disconnection position versus time. Data points in different colors are obtained for different twinning disconnections.

### 4.3.3 Twin tip migration

To further investigate the propagation of TTs, a sequence of atomic snapshots of the right TT is shown in Fig. 4.5(a), with magnified views of the PB interface in Fig. 4.5(b). As the TT moves to the right, several disconnections with step heights of one interplanar spacing are observed on the PB interface and are marked by black arrows in Fig. 4.5(b). These appear to be edge disconnections (disconnections with only edge Burgers vector character) with step heights of one interplanar spacing ($c/2$) on BP/PB interfaces, the same as those reported in the work of Zu et al. [135]. These disconnections move towards the intersections with the TB or the TT, causing the PB interfaces to migrate in a diagonal direction to the upper right of the simulation cell. At the same time, twinning disconnections start to form at the intersections but on twin planes, as denoted in the third and fourth frames of Fig. 4.5(b) by yellow arrows. One twinning disconnection is observed at the top intersection after the PB interface propagates two atomic planes in the diagonal direction, indicating that two of the disconnections on the PB interface contribute to the formation of one twinning disconnection.
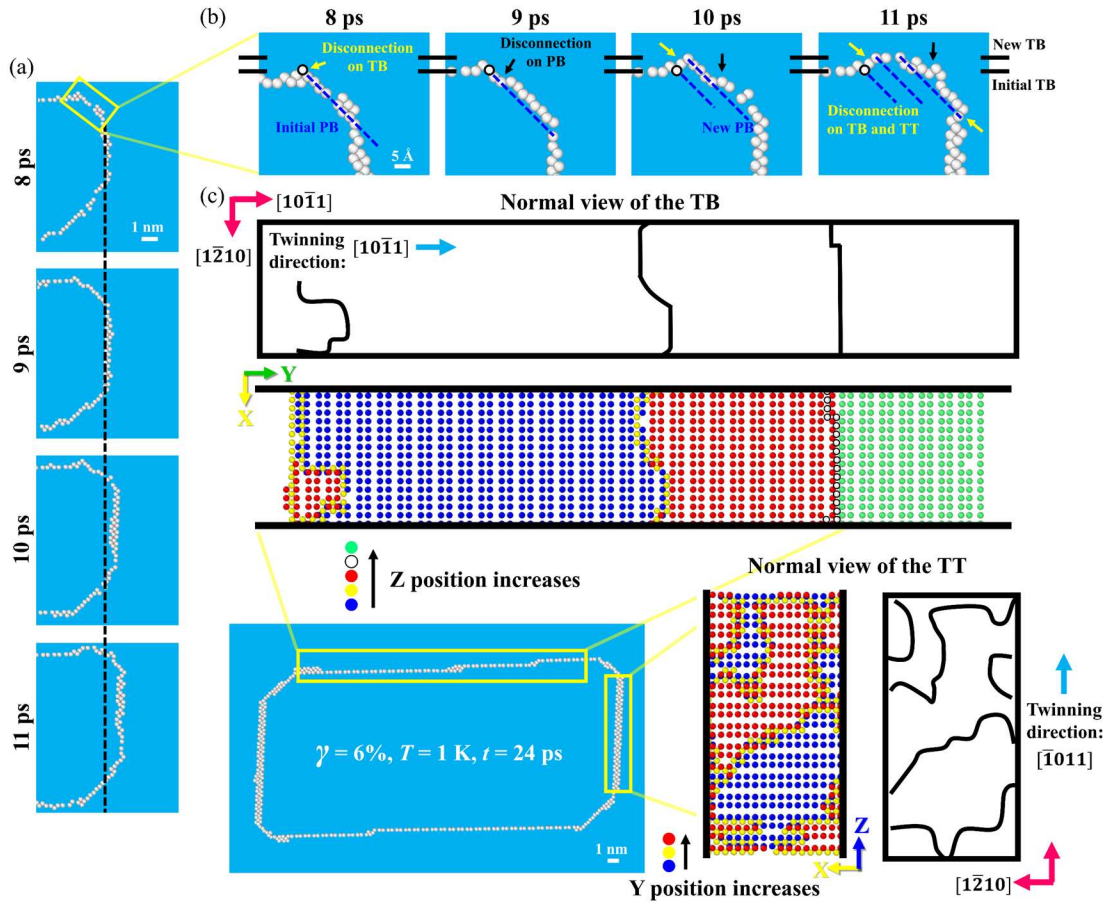
Fig. 4.5 (a) The atomic snapshots of the right TT from 8 to 11 ps for the sample deformed at 6% shear strain and 1 K. (b) The magnified view of the PB interface from 8 to 11 ps. (c) A comparison of the twinning disconnections on TB, as well as TT; atoms are colored by their Y positions or Z positions. In (a) the TT position at 8 ps is marked using a black dashed line. In (b), the TB positions at 9 ps and 11 ps are marked using black solid lines, while the PB interface positions at 8 ps, 10 ps and 11 ps are marked using dark blue dashed lines. Disconnections formed on the TB and the TT are marked by yellow arrows, while disconnections formed on the PB interface are marked by black arrows. The atom circled in black is a reference atom; its position does not change in all the frames. In (c), disconnection

lines are marked using black lines, and blue arrows show the twinning direction for each plane.

Details of the atomic structures of disconnections on BP/PB interfaces in our work can be found in Fig. 4.6. At 6.1 ps, there is a one-layer disconnection formed on the BP interface. The disconnection front involves atoms from two different BP planes, and these atoms are also in different planes along the $[\bar{1}010]$-direction, so part of atoms in lower BP plane are covered as shown in the view from the $[\bar{1}010]$-direction. At 10.15 ps, there are two one-layer disconnections formed on the PB interface, and one of them is on the top of the other one. At 10.5 ps, there is a two-layer disconnection formed on the BP interface. Barrett and El Kadiri reported the generation of disconnections with step heights of two interplanar spacings ($c$) on BP/PB interfaces by two disconnections with step heights of one interplanar spacing, and a final transformation to twinning disconnections with the involvement of disclinations (line defects where rotational symmetry is violated) at the intersections of TBs and BP/PB interfaces [136]. A similar transformation between disconnections on BP/PB interfaces and twinning disconnections was also found by Sun et al. [91], and Zu et al. [135]. According to our observations, PB interfaces move the fastest among all the boundaries of the embryo; therefore, they act as nucleation sites for twinning disconnections.
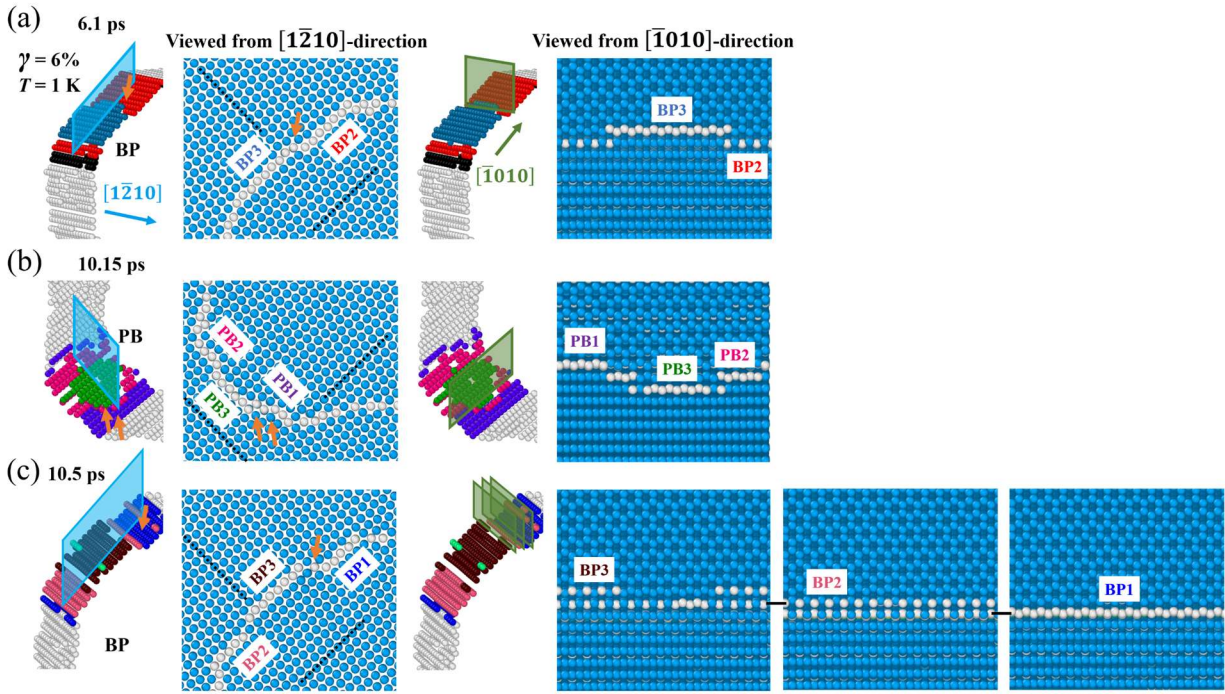
Fig. 4.6 Disconnections formed on BP/PB interfaces at (a) 6.1 ps, (b) 10.15 ps, and (c) 10.5 ps. Samples are deformed at 6% shear strain and 1 K. Different BP/PB planes are colored differently, in order to be identified more clearly, and ordered according to the time sequence of formation, with smaller numbers denoting earlier formation. The atomic structures of the disconnections are viewed from the $[1\bar{2}10]$-direction (a direction perpendicular to the blue parallelogram) and $[\bar{1}010]$-direction (a direction perpendicular to the green parallelogram), respectively. Black dashed lines are used to show the orientations of basal planes in the matrix and twin, while orange arrows are used to mark individual disconnections.

Formation and gliding of disconnections on TTs is also observed. These disconnections are also two-layer disconnections with Burgers vector parallel to the twinning direction of the $(10\bar{1}2)$ plane. Fig. 4.7(a) shows the atomic structure of one twinning disconnection

formed on the TT, while Fig. 4.7(b) shows the Burgers vector of this disconnection, determined to be $b_t = \frac{1}{15}[\bar{1}011]$. In the studies by Braisaz et al. [134] and Lay et al. [133], interfacial dislocations with Burgers vectors approximately equal to four twinning dislocations and seven twinning dislocations were reported. In our simulations, such large interfacial dislocations are not found. Unlike the twinning disconnections on TBs that have relatively straight disconnection lines, the twinning disconnections on TTs have much more tortuous disconnection lines. A comparison of the twinning disconnections on TBs and TTs is made in Fig. 4.5(c) using the normal views of boundary atoms on the two different TBs (XY plane for the TB and YZ plane for the TT). The atoms are colored by their Y or Z positions. For instance, in the normal view of the TT, the dark blue atoms have the smallest Y positions and encompass the initial TT, while the red atoms have the largest Y positions and cover the new TT, which has moved one-step height. The yellow atoms are located between these two atomic planes and delineate the disconnection lines associated with the twinning disconnections. In the normal view of the TB, there are three twinning disconnections. The two furthest to the right have not formed on the same twinning plane, so their disconnection lines lie at different Z heights and appear as different colors. It can be clearly seen that almost all white atoms are aligned. Although some tortuosity of the disconnection lines is also observed on the TBs (yellow atoms), this effect is much more prominent on the TT. Schematics of the TB and TT are also shown with the disconnection lines of twinning disconnections denoted on the two planes. Since the Burgers vectors of twinning disconnections on both planes are parallel to the twinning direction, tortuous disconnection lines indicate twinning disconnections with mixed character.
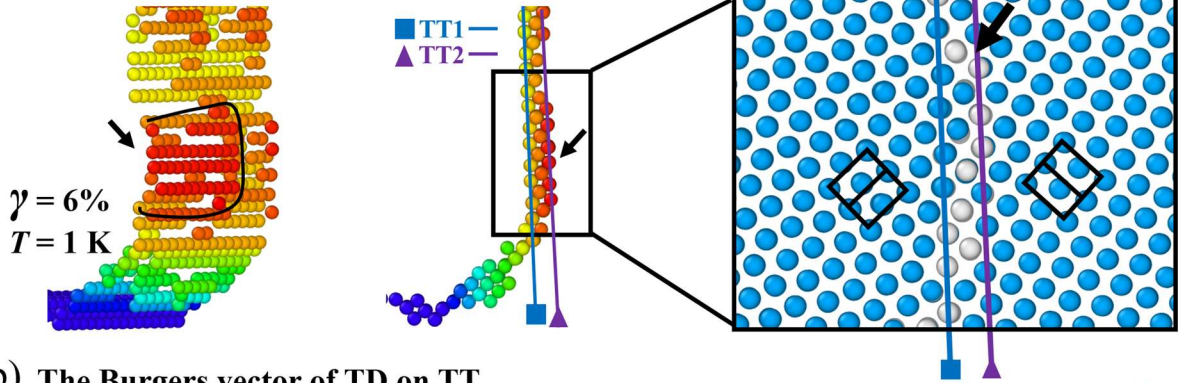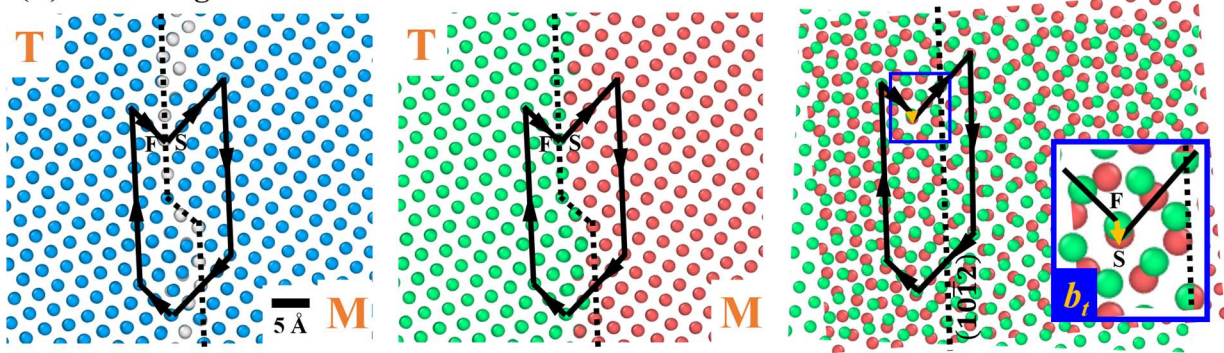
Fig. 4.7 (a) The atomic structure of one twinning disconnection formed on the TT in a sample deformed at 6% shear strain and 1 K, where the disconnection line is marked with black lines and the old and new positions of the TT are marked using solid blue and purple lines, respectively. Black arrows are used to show the location of the twinning disconnection. The outlines of two hcp cells are drawn in the matrix and twin. (b) Determination of the Burgers vector of the twinning disconnection shown in (a). The Burgers vector ($b_t$) of the twinning disconnection is marked using yellow arrows in the last frame, with the inset giving a magnified view of the Burgers vector. The structure is viewed from the negative X-direction. "M" and "T" signify matrix and twin, respectively.

### 4.3.4 Transformation between twinning disconnections and disconnections on BP/PB interfaces

As is mentioned earlier, a transformation from the disconnections on BP/PB interfaces to the twinning disconnections on TBs and TTs is likely to happen. In the last frame of Fig. 4.5(b), the twinning disconnection at the intersection of the PB interface and the TT is formed in this way. Fig. 4.8 shows an example of such transformation in detail, with an enlarged view of the BP interface at the top left corner presented. The two one-layer disconnections on the BP plane which contribute to the formation of twinning disconnection near the upper intersection between the BP interface and TT are D1 and D2. The new twinning disconnection is formed on TT2. D1 is bound by the black and red BP planes, while D2 is bound by the red and dark blue BP planes. At 5.8 ps, D1 is already formed, while D2 starts to form on BP2. At 6.4 ps, D1 and D2 transform into a two-layer disconnection. At 6.65 ps, one new twinning disconnection starts to form on TT2. Two other disconnections observed in this figure, D3 and D4, contribute to the formation of subsequent twinning disconnections. Homogeneous nucleation of the twinning disconnection on the TTs is often observed, which is possibly due to the larger local shear stress in front of TTs than the shear stress in front of TBs. The different types of twinning disconnections formed on the TB and TT lead to different migration behavior of the TB and the TT.
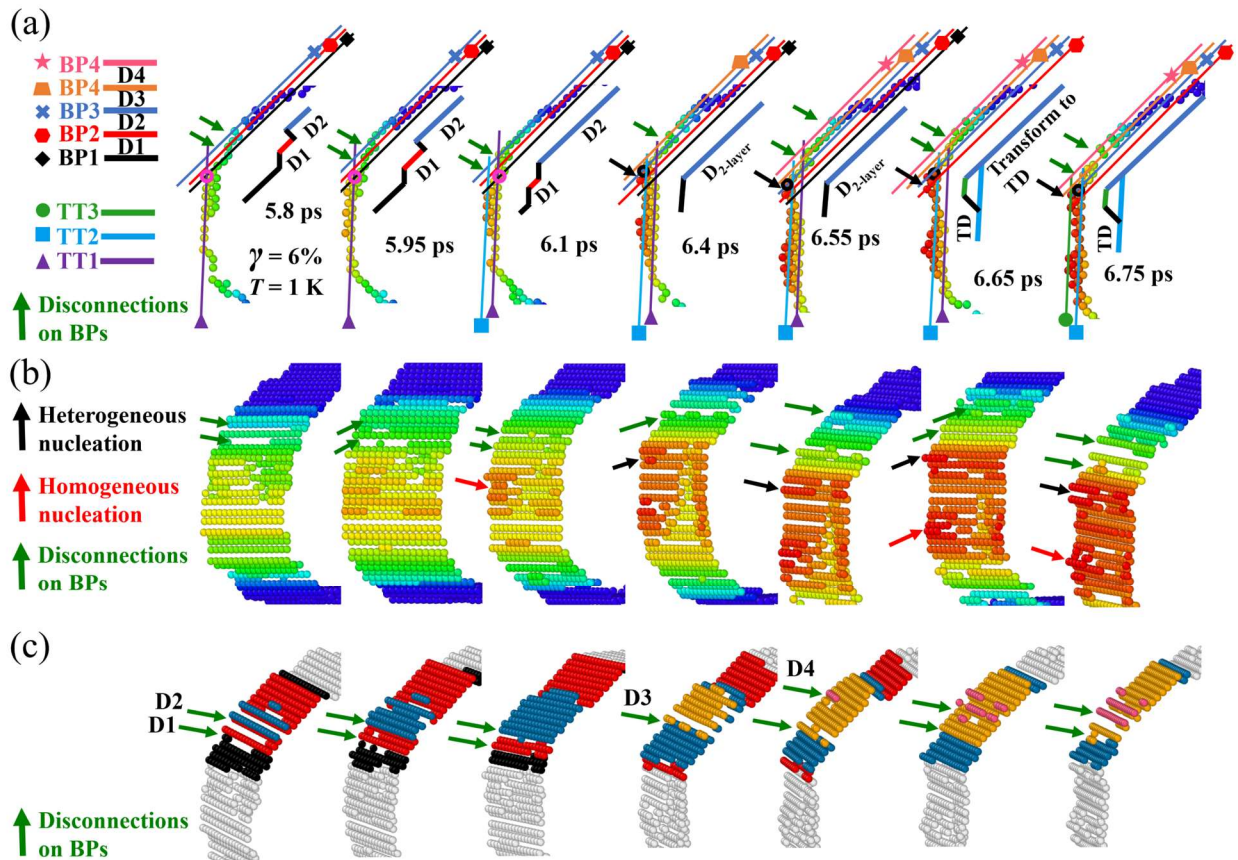
Fig. 4.8 Disconnections formed on the TTs and BP interfaces during the growth of the twin embryo in a sample deformed at 6% shear strain and 1 K, shown in both (a) normal and (b) perspective views. (c) A simplified view of disconnections on the BP interface. Different BP planes and TTs are colored differently and ordered according to the time sequence of formation, with smaller numbers denoting earlier formation. Black and dark green arrows are used to mark the disconnections formed on the TT and BP planes, respectively. Disconnections formed on BP planes are also ordered according to the time of formation. Red arrows mark two disconnections formed homogeneously on the TT. The atoms circled in magenta and black are reference atoms. The position of the atom circled in magenta does not change from 5.8 ps to 6.1 ps, while the position of the atom circled in black does not change from 6.4 ps to 6.75 ps.

### 4.4 Discussion

### 4.4.1 Phenomenological model describing twin embryo growth in Mg

Our MD simulation results capture the critical feature of faster TT propagation compared to twin thickening [128, 137-140] and isolate the importance of disconnections in this process, but also allow for the development of a general model for twin embryo growth. A quantitative description of the evolution of twin length and thickness allows us to connect MD models on the nanoscale to experimental work that usually reports on a much larger length-scale. To this end, we use our atomistic observations to develop a phenomenological model describing the growth of a single twin embryo in an infinitely large grain under a constant applied shear strain. An atomic snapshot of the twin embryo is shown in Fig. 4.9(a), while a schematic of the phenomenological model is presented in Fig. 4.9(b). The coordinate system is set up the same as our atomistic simulations. In the atomic snapshot, the twin embryo is identified by lattice orientation and colored in green, being bound by horizontal TBs, TTs, and BP/PB interfaces. This information is reproduced in the schematic, in which a green twin embryo is displayed at the center of red matrix with a length, $l$, and thickness, $h$, at a given moment in time, $t$. The TTs move in the Y-direction with velocities of $v_{TT}$, while the TBs move in the Z-direction with velocities of $v_{TB}$. Adopting the concept of BP/PB interfaces as the sources for twinning disconnections, these features are represented by the four corners of the twin embryo and generate disconnections running along the TBs. A twinning disconnection on the upper TB is identified in the atomic snapshot in Fig. 4.9(a), with a magnified view shown in the inset. In the schematic in Fig. 4.9(b), two twinning disconnections with step-heights of $h_d$ are shown on the upper and lower TBs, and these

disconnections propagate along the TB at velocities of $v_d$. The detailed derivation process of the phenomenological model is presented in Appendix A. We eventually obtain a linear relation between the twin length and time (Eq. (5)), while a logarithmic relation between the twin thickness and time (Eq. (6)).

$$l(t) = l_0 + 2v_{TT}(t - t_0) \tag{5}$$

$$h(t) = h_0 + \frac{2v_d \cdot h_d}{v_{TT}} \cdot \ln\left[1 + \frac{2v_{TT} \cdot (t-t_0)}{l_0}\right] \tag{6}$$

The dependence of the twin embryo thickness on the twin embryo length is as follows:

$$h = h_0 + \frac{2v_d \cdot h_d}{v_{TT}} \cdot \ln\left[\frac{l}{l_0}\right] \tag{7}$$
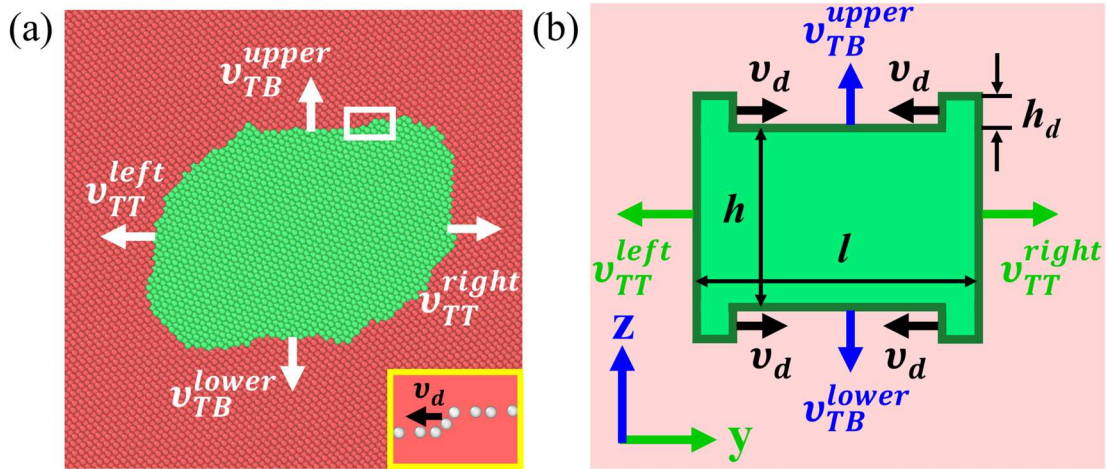


Fig. 4.9 (a) The atomic snapshot of a twin embryo in MD simulations with an inset of a twinning disconnection. (b) Schematic of the twin embryo growth model. The twin embryo in (b) is bound by two TBs and two TTs, and the BP/PB interfaces as the source of the twinning disconnections are represented by the four corners.

### 4.4.2 Connecting atomistic simulations with experiments

To connect the phenomenological model to our MD simulations, critical parameters are extracted from MD simulations under different applied shear strains using Eqs. (5) and (6). The initial twin embryo length and thickness for MD simulations are used as $l_0$ and $h_0$ when Eqs. (5) and (6) are fitted to the MD data, and the fitting results are shown in Fig. 4.10. The fit is excellent for all of the MD simulations performed in this work. Small deviations from a linear relationship between twin embryo length and time are observed at the very early times for samples deformed by 8% to 10% shear strain, due to an early twin embryo morphology that deviates from the idealized rectangular form (see inset of Fig. 4.10(a) at 5 ps). The twin embryo that grows at 10% shear strain initially adopts a more elliptical morphology that is rotated with respect to the simulation cell axes, relaxing some of the assumptions made in the model. This deviation becomes less notable as the twin embryo grows (see inset of Fig. 4.10(a) at 25 ps). TBs and TTs are slightly tilted because of the disconnection accumulation at the top right and bottom left corners.
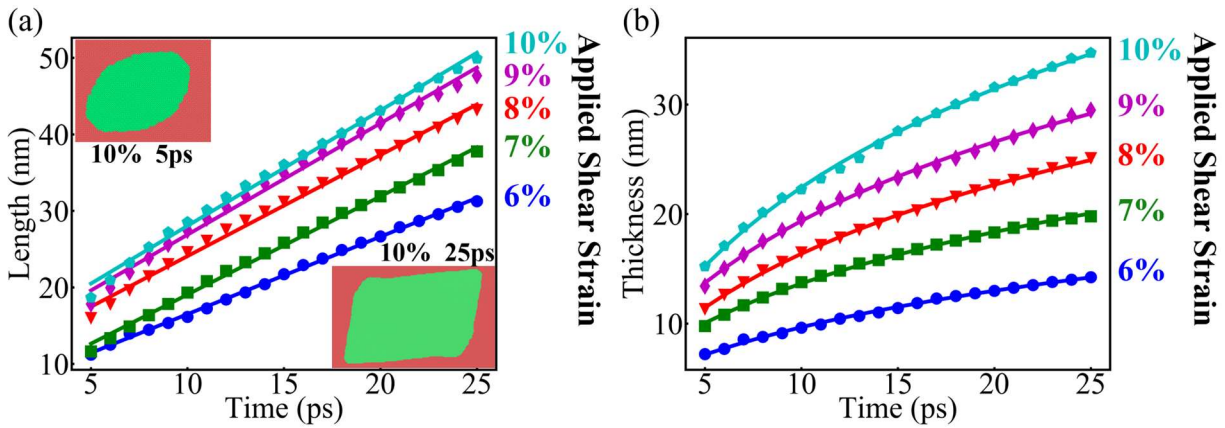


Fig. 4.10 Time evolution of the (a) length and (b) thickness of the twin embryo that grows at different shear strains and 1 K. The length is fitted by Eq. (5), while the thickness is fitted by Eq. (6). The insets in (a) show the twin embryo in a sample deformed at 10% shear strain at 5 ps and 25 ps. The twinned region is colored green, while the matrix is colored red.

To explore the influence of shear stress on TB and TT motion, values for $v_d$ and $v_{TT}$, two key velocities that describe twin embryo growth, are extracted for different matrix shear stress values. As shown in Fig. 4.11(a), both velocities increase with the matrix shear stress, which can be expected, since the applied shear stress is the driving force for disconnection migration and twin embryo growth. Also important for determining twin morphology is the ratio of $v_d$ to $v_{TT}$ as a function of matrix shear stress. Fig. 4.11 (b) shows that this ratio also monotonically increases with the matrix shear stress. We should mention that the same result is obtained for initial twin embryos of different shapes and sizes. As seen in Fig. 4.11(b) the dashed blue line obtained by fitting all the data points nearly overlaps the dashed black line obtained by only fitting the data points of samples with embryos having $l_0/h_0 \approx 1.6$, indicating that the initial twin embryo shape and size does not alter the relationship between the velocity ratio and the matrix shear stress. In the following discussion, we will only use the data for an embryo with $l_0/h_0 \approx 1.6$. Finally, we note that the disconnection velocities in Fig. 4.11 are larger than the values shown in Fig. 4.4(d) from the MD simulations. The main reason behind this discrepancy is that homogeneous nucleation of twinning disconnections does occasionally occur, which is not included in our model that only considers disconnection nucleation from the BP/PB interfaces. With slightly more disconnections than our model predicts, each needs to move slower to give the same twin thickening rate. Even with a number of approximations, the simple phenomenological model can accurately recreate the important phenomenological features of twin embryo growth.
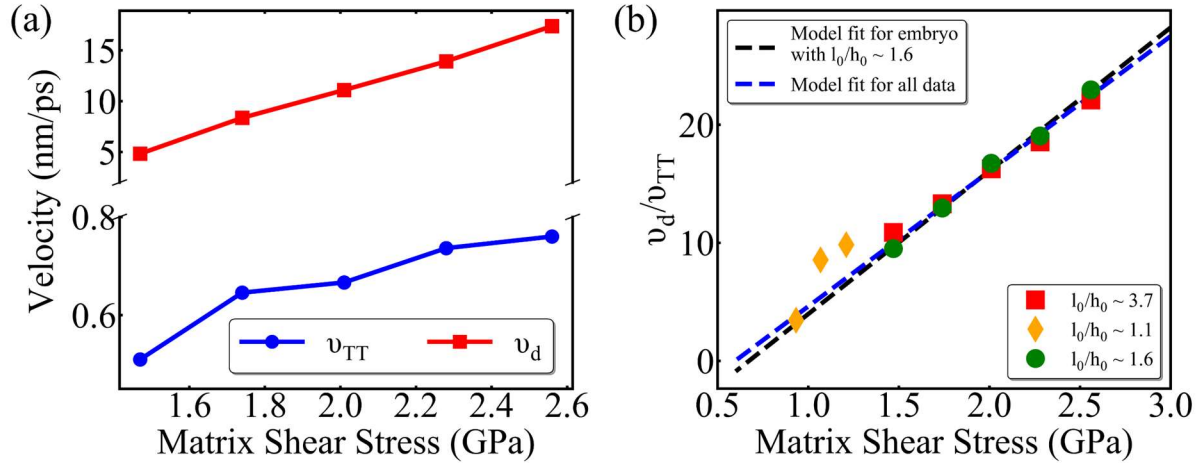
Fig. 4.11 (a) $v_{TT}$ and $v_d$ versus the matrix shear stress. (b) The ratio of $v_d$ to $v_{TT}$ versus the matrix shear stress for samples with different initial sizes of twin embryos.

The experimental work of Yu et al. [128] with in situ tensile, compressive, and bending tests on Mg single crystals of nanometer scale was chosen to test our phenomenological model. This work was chosen because: (1) it is known that the twin embryos nucleate at free surfaces, (2) no grain boundaries exist surrounding the twin, and (3) the tensile samples are nanometer sized and therefore dislocation-free. These factors result in a relatively uniform stress field, without abrupt local stress concentrations associated with other microstructural features. The experimental setup is schematically shown in Fig. 4.12(a), and a bright field transmission electron microscopy image showing an array of $\{10\bar{1}2\}$ twins is displayed in Fig. 4.12(b). The widths of the tensile bars were reported by the authors to be in the range of 100-200 nm, with the example shown in Fig. 4.12(b) being 100 nm wide. Forces were applied along the c-axis, and the nucleation of the $\{10\bar{1}2\}$ twins started at $\sim 800$ MPa. The twins then elongated during testing, with some of the TTs reaching the opposite surface of the sample. Most of the twins have thicknesses of 5-10 nm. To be more consistent with the

experimental setup, the phenomenological twin embryo growth model was modified to include the existence of a free surface or a grain boundary that can provide sites for heterogeneous nucleation of twinning disconnections [128, 141]. Free surfaces and grain boundaries should have a similar ability to generate disconnections as BP/PB interfaces. Most of these twins observed in the experiment adopt a half-lenticular morphology, meaning that they are thinner at the TTs terminated in the matrix and wider at the free surface or grain boundary [18, 128, 142].

The schematic for the modified twin embryo growth model is presented in Fig. 4.12(c). The TT cannot move to the left due to the presence of the free surface, so Eqs. (5), (6) and (7) are updated as:

$$l(t) = l_0 + v_{TT}(t - t_0) \tag{8}$$

$$h(t) = h_0 + \frac{4v_d \cdot h_d}{v_{TT}} \cdot \ln\left[1 + \frac{v_{TT} \cdot (t - t_0)}{l_0}\right] \tag{9}$$

$$h = h_0 + \frac{4v_d \cdot h_d}{v_{TT}} \cdot \ln\left[\frac{l}{l_0}\right] \tag{10}$$

Eq. (10) can be used to fit experimental data of twin length and thickness to obtain the ratio of disconnection velocity to TT velocity. Measurements of twin length and twin thickness from the image displayed in Fig. 4.12(b) are presented in Fig. 4.12(d). Nine twins that could be clearly identified were selected. The twin length and twin thickness are then approximated as the length and width of the rectangles shown in Fig. 4.12(b), respectively. The ratio of $v_d/v_{TT}$ = 3.4 ± 0.55 is obtained. To determine the shear stress, the applied stress at the point of twin nucleation that was reported in experiments is transformed to the resolved shear stress ($\tau_{RSS}$) via the Schmid factor ($m$). The $\tau_{RSS} = \sigma \cdot m = \sigma \cdot (\cos\theta \cdot \cos\varphi)$, where $\theta$ is the angle between the loading axis and twin plane normal, $\varphi$ is the angle between the

loading axis and the twinning direction, and $\sigma$ is the applied normal stress. For the $\{10\bar{1}2\}$ twins created by stretching the c-axis, the Schmid factor is 0.499, so $\tau_{RSS}$ = 800 MPa × 0.499 = 399.2 MPa. Fig. 4.12(e) shows this single experimental data point together with our MD data. The experimental data point fits well with the extrapolated curve for our MD simulations at 300 K. The fact that the ratio of the disconnection velocity to TT velocity can be predicted and is consistent with our atomistic modeling results demonstrates the robust nature of the phenomenological model developed here. The heterogeneous nucleation of twinning disconnections dominates TB migration at twin lengths of several hundred nanometers. Note that as the matrix shear stress decreases to a certain level, the velocity ratio $\upsilon_d/\upsilon_{TT}$ becomes negative, indicating the shrinkage of an existing twin embryo. This finding is again consistent with our MD simulations, which showed that a critical strain must be applied or else the twin embryos will shrink and disappear. Eq. (10) also yields a relation between the twin length ($l_0$) and twin thickness ($h_0$) at the beginning of the steady-state twin embryo evolution, which is $5.168 \cdot \ln l_0 - h_0 = 17.96$. So if a range of $h_0$ from 0.76 nm (twice the step height of twinning disconnections and the minimum imaginable twin thickness) to 4.3 nm (initial twin thickness used in MD simulations) was considered, then the expected range for $l_0$ would be 37 nm to 74 nm. We note that experiments typically are unable to extract the values of the initial twin embryo size, as it would necessitate high magnification TEM in exactly the right place at exactly the right time.
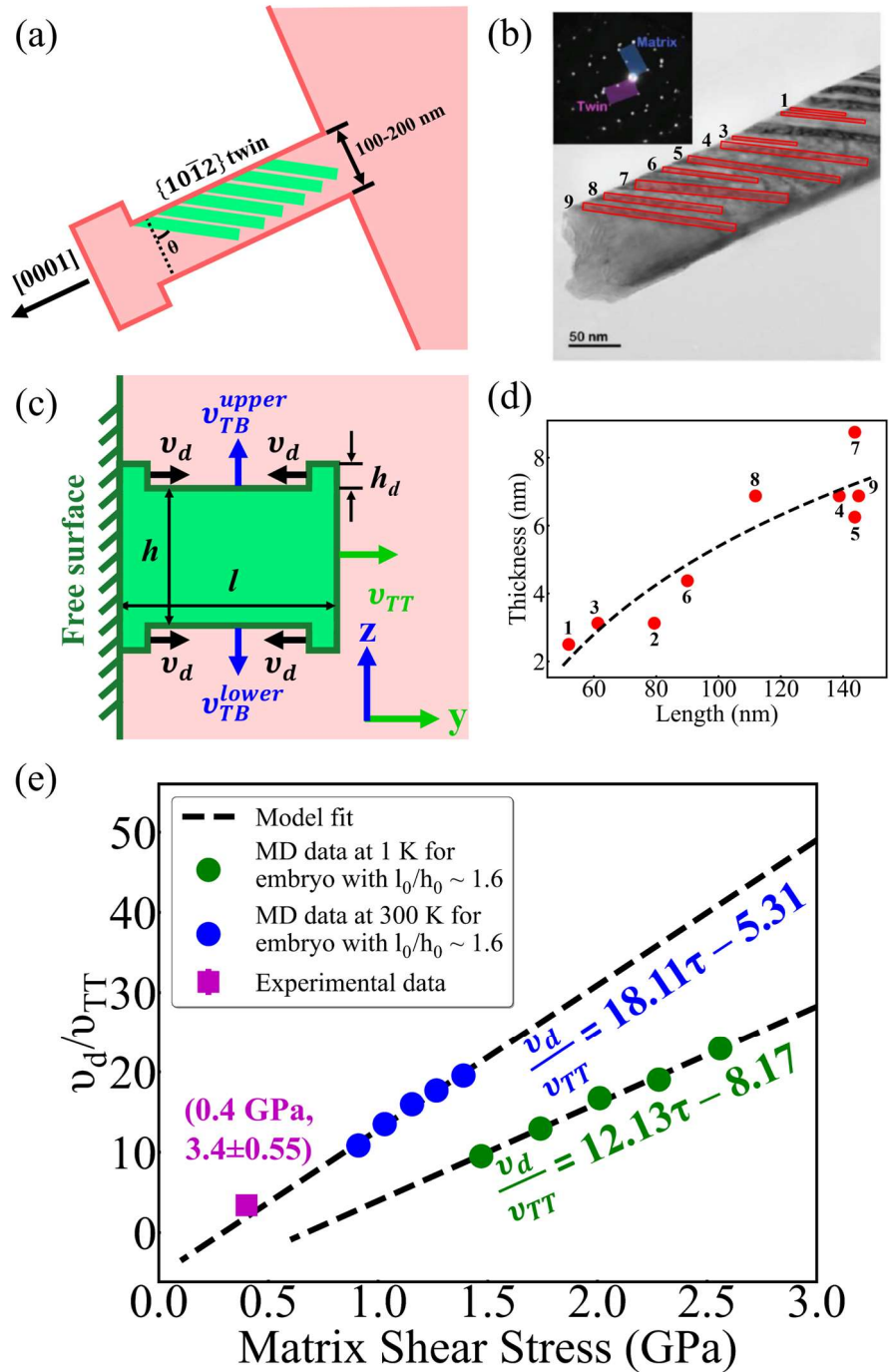
Fig. 4.12 (a) The experimental set up of the *in-situ* tensile testing in Ref. [128]. (b) A TEM image that shows the {10$\bar{1}$2} nanotwin array in a tensile sample. The inset displays the related diffraction pattern with beam direction along [1$\bar{2}$10]. Nine twins are selected to measure length and thickness and are numbered from 1 to 9. Images in (b) are reproduced

with permission from Ref. [128].  (c) The schematic of the modified twin embryo growth

model with the presence of free surfaces.  (d) The twin thickness versus twin length for those

twins selected from (b) along with the fit obtained using Eq. (10).  (e) The ratio of $\upsilon_d$ to $\upsilon_{TT}$

versus matrix shear stress for both MD simulations and data extracted from the

experimental work [128].


### 4.4.3 Effective application and further extensibility of the model

The current model is developed to describe the initial embryotic growth stage of a twin

formed by homogeneous nucleation in an infinitely large and perfect grain, in which there

are no impurities or solute atoms, defects such as dislocations, and influence from other

twins.  The nucleation process of twin embryos, such as where and how twin embryos are

nucleated are not included in this work.  The model can be applied to analyze experimental

results, especially the relationship between twin length and twin thickness described by Eq.

(10) can be used to predict the final thickness of twins.  Parameters, such as the initial size

of the twin embryo, $l_0$ and $h_0$, the final twin length, $l$, and the ratio of the two velocities, $\upsilon_d$ and

$\upsilon_{TT}$ must be obtained.  While the final twin length could be measured via electron microscopy

and the ratio of the velocities can be predicted by MD simulations for a given set of

conditions, the initial size of the twin embryo is less certain.  As mentioned earlier,

experimental observations of twin embryos are missing due to their rapid expansion, with

most twin embryos growing beyond their initial size by the time of observation.  MD

simulations allow twin nucleation to be explored.  For instance, twin embryos can be

initiated by structurally relaxing two partial dislocations at a certain distance [68], meaning

the initial twin embryo size might also be found from such simulations.  Our findings are also

applicable to the thickening of "tapering twins". Mahajan and coworkers [143-145] first observed twinning dislocations and their reactions at thin "tapering twins" in face-centered-cubic Cu and body-centered-cubic Mo-Re alloys. "Tapering twins" may be formed by tiny embryo growing into each other, and they contain twinning dislocations/disconnections. These disconnections could move in a similar fashion.

A possible limitation of our simulations and phenomenological model is the two-dimensional nature. Recently, Liu et al. [146] revealed the structure of the "dark side" of a twin embryo via high resolution transmission electron microscopy. They found the "dark side" of a twin embryo is composed of coherent TBs and semi-coherent twist prismatic–prismatic boundaries. To explore the migration of the "dark side", Gong et al. [147] developed the 3D twin embryo in MD simulations, and reported the motion of twist prismatic–prismatic boundaries through atomic shuffling as well as the pinning effect of misfit dislocations on such boundaries. Spearot et al. [73] also showed that three-dimensional simulations are needed to capture disconnection terrace nucleation and growth processes that are essential for the migration of mature TBs (i.e., larger TBs which can be approximated as flat interfaces, without considering bounding PB/BP interfaces, grain boundaries, or surfaces). In this study, the third dimension was essential for capturing homogeneous disconnection nucleation from the flat TB. In our paper, we focus on the growth of an embryo in its shear plane in two-dimensions, so any interactions with defects responsible for growth in the third dimension are not considered here. However, we obtain excellent agreement with experiments [128], which would indicate that interactions with processes in the third direction do not dominate the early stages of embryo growth.

In addition, the current model can be extended in multiple ways to cover different conditions in experiments, which opens up future research opportunities. As discussed earlier, grain boundaries and free surfaces may also facilitate the nucleation of twinning disconnections. Twinning disconnections might also be generated through the interaction between twins and dislocations [59]. For the case where multiple twins grow in one grain, a common occurrence observed in experiments, the stress fields around the twins can interact and affect their subsequent growth. For example, using tri-crystal models containing two twins, Arul Kumar et al. [75] predicted that within a certain distance, the stress-fields around two twins overlap and give higher back stresses that resist further twin growth. As twins get thicker and longer, it is also possible that multiple twins merge together and eventually leave one thick twin in the grain, or twins propagating in different directions might intersect to form twin junctions. These junctions can also play an important role in twin growth, as demonstrated in early studies on Co and Co-Fe showing that the incident shear strains of the crossing twin can be accommodated by activating dislocation slip within or on the exit side of the crossed twin, or alternatively inducing secondary twinning or secondary slip in the crossed twin which can result in either thickening or detwinning [148, 149]. Segregating impurities or solutes are another contributing factor that strongly influences twin growth. Solutes located at the boundary of the twin embryo demonstrate a pinning effect on boundary motion and thus suppress twin growth, as shown in the work of Nie et al. [18]. These authors used atomic resolution transmission electron microscopy images of Gd-doped and Zn-doped coherent TBs in a Mg alloy to show that solute segregation limited the expansion of twins, compared to observations in pure Mg.

## 4.5 Conclusions

In this work, MD simulations were conducted to reveal the initial growth mechanisms of a twin embryo in a single Mg crystal.

- The simulation results reveal a constant velocity for the TT, while a decrease in the TB velocity over time (i.e., as the twin embryo grows). Twinning disconnections nucleated at the intersections between BP/PB interfaces and the TBs, followed by their lateral motion across the TB. The velocity of the twinning disconnections was found to be constant for given applied shear stress. Accumulation of twinning disconnections on TBs occurred, especially at the later stage of simulation when the twin length is relatively large, suggesting that the propagation of twinning disconnections is the rate-limiting process for twin embryo growth.

- In addition, a phenomenological model was developed to describe the evolution of twin length and thickness with time. The proposed model fits well with the simulation data for the two key parameters, the velocities of TTs and twinning disconnections, being extracted. Both velocities increase monotonically as the applied shear stress increases. The phenomenological model was also found to fit an experimental report on nanoscale twin growth, even though the stress level was much lower than those probed by MD and used to calibrate the model. We envision that this model can be used to predict various twin geometries and morphologies given known experimental conditions.

Taken as a whole, our work fills an important gap in the understanding of twinning by providing a clear and consistent description of the early stages of twin embryo growth. The

time evolution of twin length and thickness are studied together for the first time, with kinetic parameters such as TT velocity and twinning disconnection velocity obtained.

# CHAPTER 5: Alloying effects on boundary migration in Mg alloys

## 5.1 Introduction

After the atomistic growth mechanisms of twin embryos in pure Mg are gained, we now move our focus to the effect of solute atoms on twin embryo growth. Alloying is a common way to improve the properties of pure Mg. For example, in the work of Stanford et al. [150], introducing ~5 wt.% Y into pure Mg samples leads to both enhanced yield strength and ductility. While focusing on the overall alloying effect on bulk properties, the growth process of twin embryos at the presence of solutes has been largely neglected. However, the work of Cui et al. [94] showed increased number of twin variants activated in the alloys versus the pure Mg samples, which indicates a solute effect that has never been discussed before (see Fig. 5.1(a)). Using high-resolution transmission electron microscopy, Xin et al. [151] observed the segregation of Y atoms to the twin boundary and BP/PB interfaces and Y-rich cluster at the BP facets (A faceted twin boundary refers to a structural feature of "TB-BP-TB", with a small BP interface connecting two coherent twin boundaries). How these solutes alter the motion of the faceted twin boundaries becomes an interesting question. In this chapter, some initial steps are provided towards the goal of understanding the solute effect on twin embryo growth. Two scenarios are considered, one is solute being in the bulk as solid solution additions, the other one is solute segregating and clustering at the faceted twin boundary. Two alloys are chosen for study, Mg-Al and Mg-Y, Al and Y are both common alloying elements for Mg.

## 5.2 Randomly distributed solutes add stochasticity in twin embryo growth

### 5.2.1 Computational Methods

A triclinic simulation cell was constructed, as shown in Fig. 5.1(b), with the X-axis set along the $[1\bar{2}10]$-direction and Y-axis set along the $[10\bar{1}1]$-direction. The top and bottom surfaces of the simulation cell are, therefore, parallel to the $(\bar{1}012)$ twin plane. The dimensions of the simulation box are approximately $5.1 \times 77.2 \times 77.0$ nm$^3$ in the X, Y, and Z directions with periodic boundary conditions being applied to all directions. The sample contains $\sim$1,300,000 atoms. One twin embryo with a length of 7.6 nm and a thickness of 4.1 nm is inserted at the center of a simulation box using the Eshelby method reported by Xu et al. [132]. The inset of Fig. 5.1(b) shows the morphology of the twin embryo, which is bound by twin boundaries (TBs), conjugate TBs (c-TBs, almost 90° to the TBs), basal-prismatic (BP), and prismatic-basal (PB) interfaces. In last chapter, we show that twin embryo growth mechanisms in pure Mg are not influenced by the initial twin embryo shape and size [153]. Al atoms are then introduced by randomly replacing Mg atoms, with the average concentration varying from 0-10 at.%. Note that the size of the simulation box for different alloys was slightly different due to the change of equilibrium lattice constant as solute concentration was varied.

MD simulations were conducted using the EAM potential developed by Liu et al. [152]. Shear deformation is applied to the simulation box to drive embryo growth. First, a global shear stress of $\sim$1.05 GPa is applied to the simulation cell using an NPT (i.e. isothermal-isobaric) ensemble at 1 K. The cell is held for 1 ps, by which time any fluctuations in the shear stress have become negligible. After this time, an NVT (i.e. isothermal-isochoric) ensemble is then used to fix the shear strain value that was responsible for the 1.05 GPa stress (varies slightly with alloy composition) and relax the simulation cell. We note that the twin embryo wants to grow to relax the applied stress, which results in a drop in global shear

stress as the twin fraction increases. For Mg-Al alloys, sixty samples with the same global concentration but different distributions of solutes are used to enable a statistical analysis of twinning. For pure Mg samples, sixty samples are also used but with different atomic velocity distributions. Visualization of atomic configurations is performed using the same way as mentioned in the last chapter. Atoms in the matrix and twin are then differentiated from each other using the orientation information, with Mg atoms in the matrix colored red and those in the twinned region colored green. In all images, the Al solutes are colored dark purple.
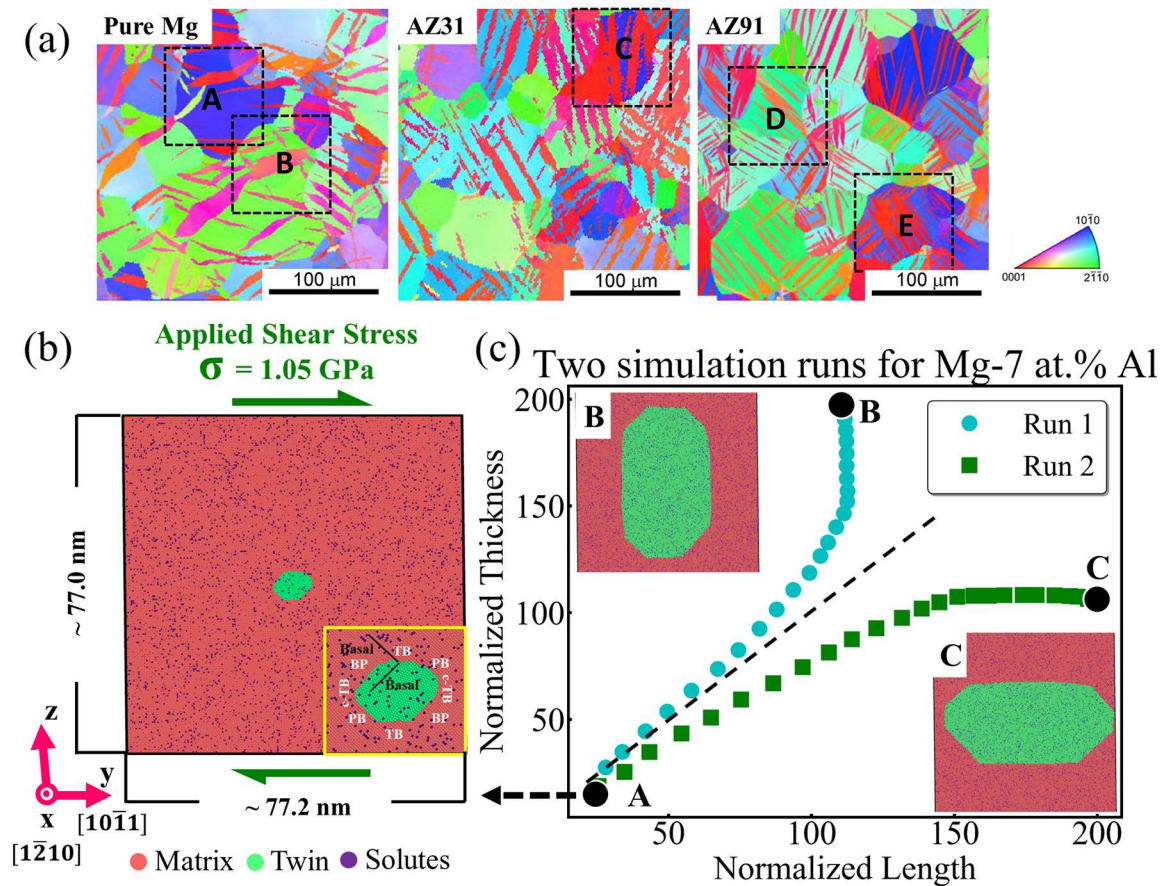


Fig. 5.1 (a) Grain orientation maps of pure Mg, AZ31 alloy, and AZ91 alloy compressed to an engineering strain of 4% under a strain rate of 0.01 s$^{-1}$. Images in (a) are reproduced with permission from Ref. [94]. (b) The atomic snapshot of the simulation box with the initial

twin embryo shown. The inset of (b) shows an enlarged view of the twin embryo, with different interfaces being designated. The basal planes in the matrix and the twin are also shown using solid black lines. (c) The variation of normalized twin thickness (thickness divided by the lattice constant) with normalized twin length (length divided by the lattice constant) for two simulation runs of Mg-7 at.% Al. The insets of (c) show the final configurations of twin embryos in the two runs. A black dashed line is plotted as the 1:1 reference line. Mg atoms in the matrix are colored red, Mg atoms in the twin are colored green, and Al solutes are colored dark purple.

### 5.2.2 Results and Discussion

In our previous work on twin embryo growth in pure Mg [153], the lateral propagation of c-TBs was observed to be faster than the migration of TBs, which leads to TBs becoming the primary boundaries as the twin grows and matures. TB motion occurred by disconnection propagation, and a logarithmic relation between twin length and thickness was obtained. However, we find here that these findings do not hold true for alloy samples and embryo growth in the alloy exhibits a very different pattern. Fig. 5.1(c) shows the evolution of twin embryos in two samples of Mg-7 at.% Al. Two different twinning behaviors are observed, in which either the TB or c-TB becomes the primary boundary, leading to two different shapes. To follow the changes in shape, the twin length and thickness are measured as the position difference of the two TBs and c-TBs, respectively, with procedural details provided in the last chapter. To allow for a better comparison of twin embryo growth among the sixty alloy samples, the twin length and thickness are normalized by the lattice constant, $a$, at a given concentration. The black dashed line in Fig. 5.1(c) is the 1:1 reference line, so

the samples with horizontally- and vertically-grown twin embryos exhibit data points above or below the reference line, respectively. We note that the data generated near the end of the simulation, namely after the twin embryo reaches 22% volume fraction of the simulation cell, is not used for any analysis due to the strong interaction with periodic images.

The first suspected cause for the two distinct evolutions in embryos is the variations in local shear stress between different random samples since twin embryos grow towards regions with large shear stress. The spatial variation of initial shear stress for Mg-7 at.% Al is plotted in Fig. 5.2. The stresses at each Y position or Z position are averaged over samples showing the same twinning behavior (the blue curve for $(\bar{1}012)$ twins and the orange curve for $(10\bar{1}2)$ twins), standard deviations are also calculated. Fig. 5.2 shows that the average shear stress decreases as the Y or Z position approaches the center of the simulation box, but suddenly jumps at certain positions, and then continue going down until it reaches the minimum. The two local peaks indicate the positions of TBs or c-TBs. Atoms in the vicinity of TBs and c-TBs are located in the different structural environment than atoms in the bulk, and therefore leads to drastic changes of the local stress. Twinned regions show lower shear stresses caused by the twin shear transformation. Though local fluctuations of the blue and orange curves slightly differ, the overall trend of the two curves is very similar and they almost overlap each other. Thus, there is no discernible difference in the initial stress state in these samples, and local stress variations are not the driving force for twin variant selection in our simulations.
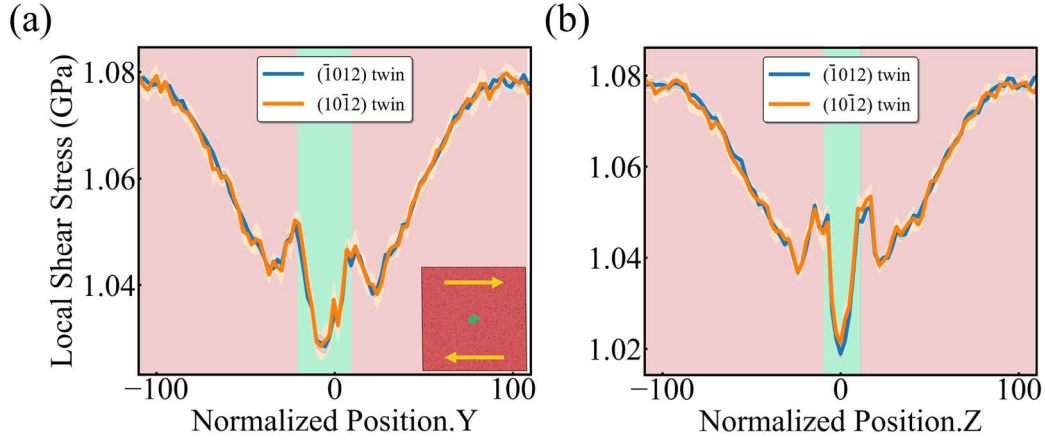
Fig. 5.2 The distribution of initial shear stress along the (a) Y-axis and (b) Z-axis in samples of Mg-7 at.% Al. The stress values at each Y position or Z position are averaged over samples adopting the same twin variants. The standard deviations are also shown. The insets in (a) show the directions of shear stress. The light green region in each frame is the twinned region, while the light red region is the matrix.

To differentiate between the horizontally- and vertically-grown twin variants, it is convenient to use the aspect ratio (*AR*), which is defined here as a twin thickness divided by twin length. Analyzing the two examples shown in Fig. 5.1(c), the atomic positions of the twin embryos at 0.5% and 22% volume fractions overlap for the horizontally-grown embryo (Fig. 5.3(a)), while there are substantial deviations in atomic positions for the vertically-grown embryo (Fig. 5.3(b)), indicating rotation of basal planes during vertical twin embryo growth. Considering all simulation data, a linear dependence between basal plane rotation angle, defined as the misorientation between the basal plane and the YZ plane, and the natural logarithm of aspect ratio is revealed, as shown in Fig. 5.3(c). The existence of this trend identifies that the horizontally-grown and vertically-grown twins belong to different

co-zone twin variants, specifically the ($\bar{1}012$) twin and ($10\bar{1}2$) twin, corresponding to the negative and positive sign of ln($AR$), respectively.

To understand the origins of the two states, we analyze the evolution of twin embryo shape using the variation of ln($AR$) with the twin volume fraction ($V_t$), as shown in Fig. 5.3(d). Since the same initial embryo configuration is used for all samples, all of the curves start from the same negative value corresponding to the initial ($\bar{1}012$) twin embryo. During the early growth stage, all of the curves strongly fluctuate up and down until they converge to either an increasing or decreasing trend (see Fig. 5.4), indicating the future twin variant. Eventually, as an indication of the two divergent behaviors, the value of ln($AR$) becomes larger than 0 for some curves, indicating a transition to the ($10\bar{1}2$) twin variant, while remaining below 0 for others. The analysis, thus, identifies two stages of twin embryo growth, a stochastic incubation stage and the deterministic growth stage, as shown in Fig. 5.3(d).

The transition from one stage to another can be determined by tracking the slope $d$ln($AR$)/$dV_t$ for each curve, where the sign of the slope shows the intent to adopt one twin variant or another. The twin volume fraction corresponding to the transition point increases with an increase in solute composition, making the stochastic stage more profound. In turn, the probability of adopting the ($10\bar{1}2$) twin variant increases with increasing solute composition, as demonstrated in Fig. 5.3(e). In this figure, ln($AR$) is obtained for each sample at the end of the simulation run (22% twin volume fraction), and plotted for the sixty samples at each alloy composition. The median values of ln($AR$) for each composition are marked with black dots and shift closer to 0, meaning that there is more random selection of twin variants at higher compositions. We note that, while all of the samples reached the

deterministic growth stage by the time the twin volume fraction reached 22% volume fraction, not all of the nanoscale simulations adopted the intended twin variant that would be preferred for an infinitely large simulation cell (i.e., our small simulation size needed to run many identical configurations stopped the growth prematurely).

To extrapolate our MD results to larger length scales and better determine the chances to adopt another twin variant, we calculated the average slope $d\ln(AR)/dV_t$ in the range from 15 to 22% twin volume fraction for each sample and present them in Fig. 5.3(f). Again, values below 0 would correspond to the expected $(\bar{1}012)$ twin, while values above 0 would indicate selection of the alternative $(10\bar{1}2)$ variant. Consistent with results from direct simulation, the extrapolation to larger simulation sizes suggest that alloying Mg with >5 at.% Al should promote the formation of multiple twin variants. The critical solute concentration beyond which there is the possibility of forming multiple twin variants may be influenced by the applied stress and temperature, but the existence of this critical concentration itself is already interesting. This is a novel finding, implying that alloying can overcome the typical strong preference believed to be pre-determined by the relative orientation of the grain and applied stress.
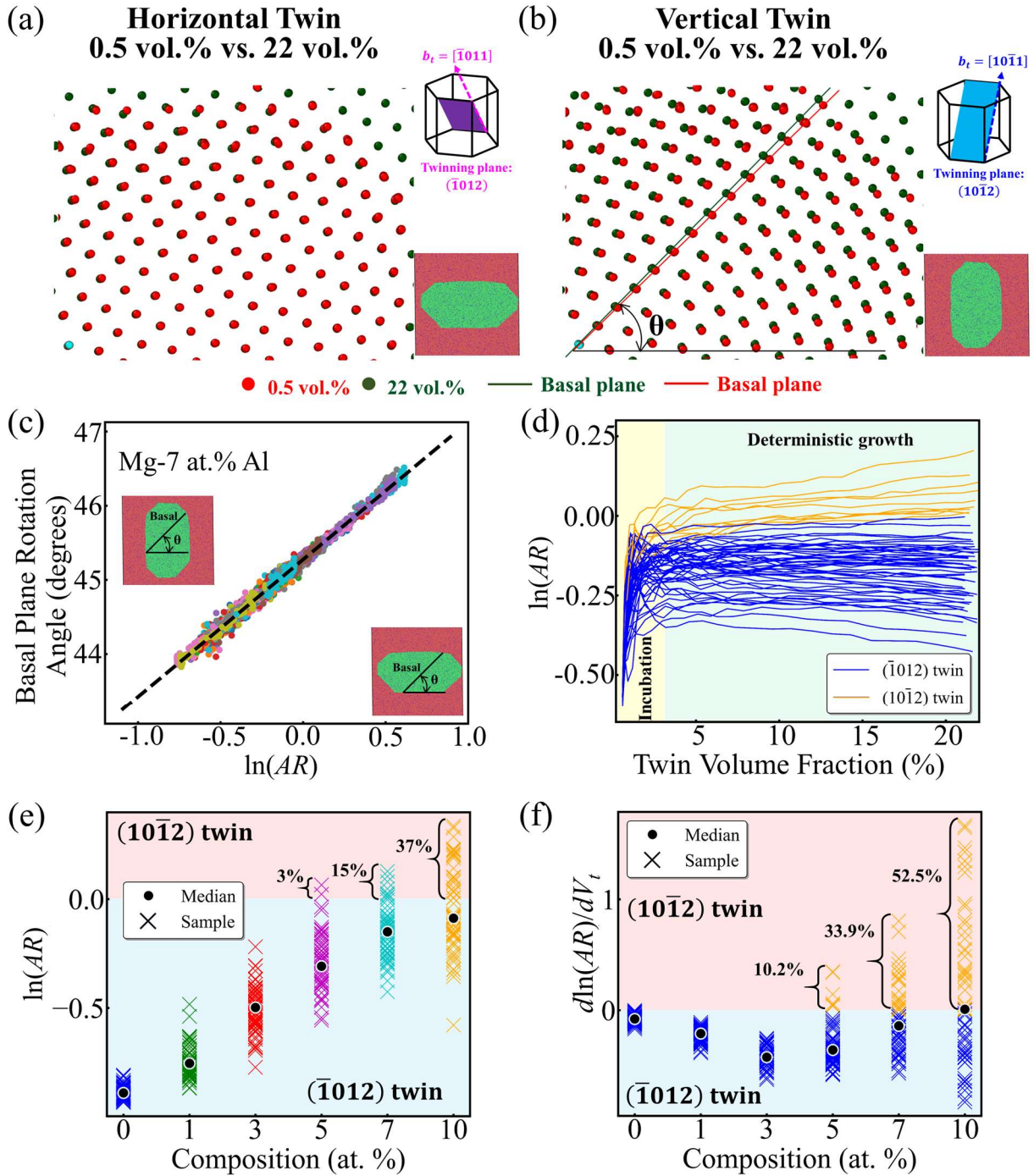
Fig. 5.3 The atomic positions of a twin embryo at the beginning (0.5% twin volume) and end (22% twin volume) of a simulation for (a) a sample which grows horizontally and has TBs as the primary boundaries and (b) a sample which grows vertically and has c-TBs as the primary boundaries. The basal planes in twin embryos of different volumes are marked

using red and dark green lines, respectively, in (b). (c) Basal plane rotation angle versus the natural logarithm of aspect ratio for Mg-7 at.% Al samples, showing a linear relationship. (d) The variation of ln($AR$) with twin volume fraction for Mg-7 at.% Al samples, where a value below 0 denotes a horizontal twin and a value above 0 denotes a vertical twin. The different twin variants are denoted by the color of the curve, while the yellow region is the stochastic incubation period and the red region is the deterministic growth stage. (e) The natural logarithm of aspect ratio taken at the end of the simulations for pure Mg and Mg-Al alloy samples with different concentrations. The median of the data for each composition and the fraction of samples with aspect ratios larger than one is also shown. (f) The average value of $d$ln($AR$)/$dV_t$ measured in the range from 15% to 22% twin volume fraction in (e) is used to extrapolate to an infinitely large sample cell size. The data are colored according to the final predicted twin variant.
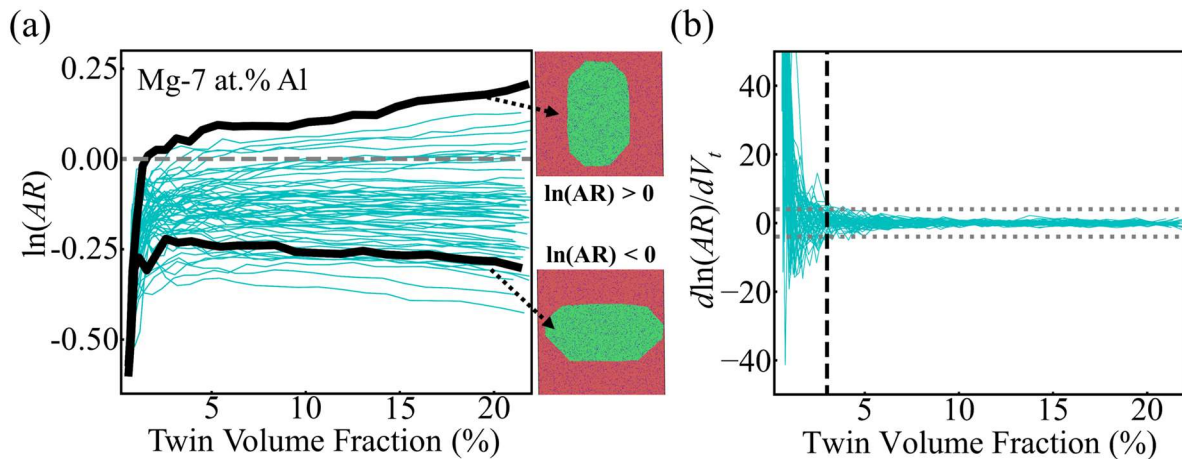


Fig. 5.4 (a) The variation of ln($AR$) with twin volume fraction for Mg-7 at.% Al samples. The data for two samples are manifested using large black circles, and the twin embryo configuration at 22% volume in each sample is also shown. (b) The variation of $d$ln($AR$)/$dV_t$ with twin volume fraction for Mg-7 at.% Al samples. Grey dotted lines mark the value of ±4,

and the black dashed line gives an estimation of the boundary between the incubation period and the deterministic growth stage.

Stochastic simulation of multiple variants opens a pathway for the formation of twin meshes within individual grains. On the one hand, when the same macroscopic stresses are applied, a grain in an alloyed sample is more likely to develop multiple twin variants than a grain in a pure Mg sample, which could then result in intersecting twins which started as different twin embryos. On the other hand, we find via calculation that the addition of more solute also slows the growth of the twin embryos, potentially even restricting growth completely (see Fig. 5.5). These results indicate an optimal condition for having both (1) considerable twin embryo growth and (2) the random selection of twin variants.
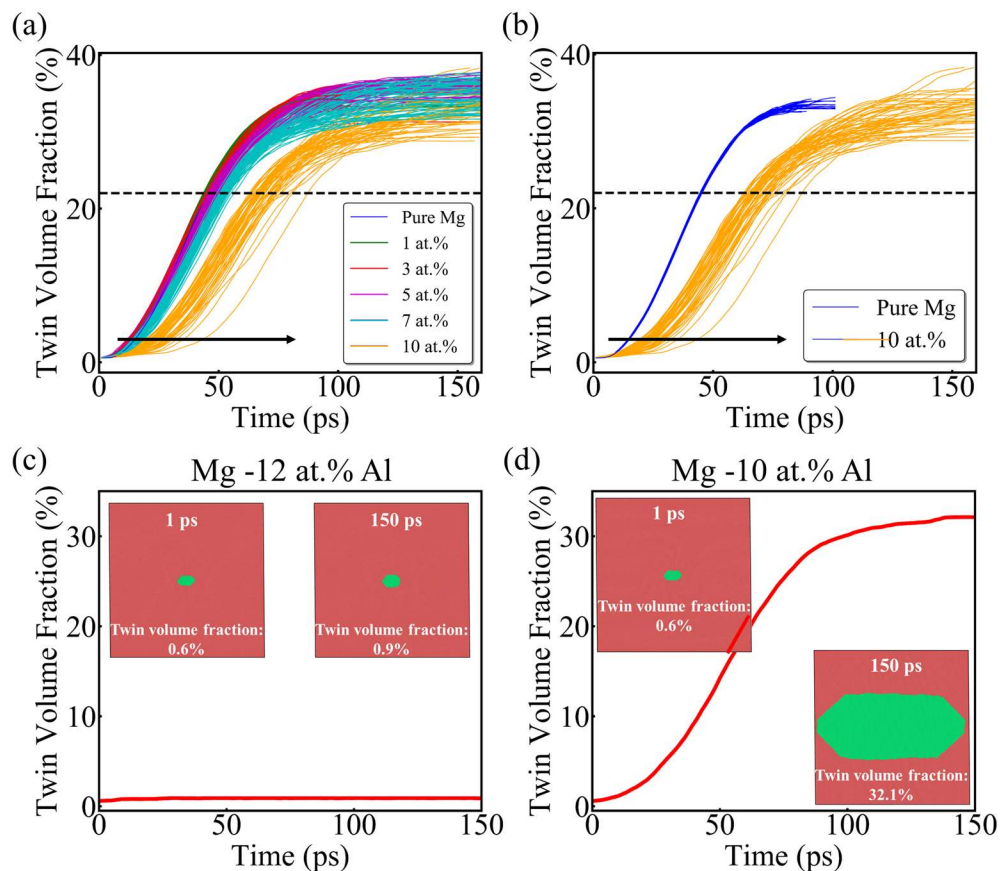
Fig. 5.5 The twin volume fraction versus time for all sixty samples of (a) pure Mg and Mg-Al alloys with all concentrations, and (b) pure Mg and Mg-10 at.% Al alloys. As the Al concentration increases, curves of twin volume fraction versus time start to shift to the right, meaning slower growth of twin embryos. Twin volume fraction versus time in one sample of (c) Mg-12 at.% Al, and (d) Mg-10 at.% Al. The insets in (c) and (d) show the configuration of twin embryo at 1 ps and 150 ps with the twin volume fraction being revealed.

To reveal the atomistic mechanisms behind random twin variant selection in the high-concentration alloy samples, we focus on the effect of solute atoms on the nucleation and propagation of twinning disconnections, since these two processes drive the twin embryo growth [153]. In our simulations, twinning disconnections can be nucleated in two ways, depending on the source of disconnection nucleation. As shown in Fig. 5.6(a), twinning disconnections are formed at BP/PB interfaces in pure Mg samples, which then migrate towards each other to advance the TB or c-TB. The black arrows mark the formation of new twinning disconnections, while solid black lines mark disconnection lines. Solute atoms have both supportive and restrictive impacts on embryo growth. On the one hand, solute atoms promote the nucleation of twinning disconnections [70, 73, 154]. In the alloy sample shown in Fig. 5.6(b), small disconnection loops (circled in black) have nucleated in the middle of the TB, indicating homogeneous nucleation of twinning disconnections without the assistance of the BP/PB interfaces. On the other hand, solutes exhibit a pinning effect and reduce the velocity of twinning disconnection motion [70, 73, 154]. Disconnection lines in the alloy samples are more tortuous than the disconnection lines in pure Mg samples, because of this pinning effect of solutes. While similar findings of solute effect on the nucleation and

propagation of twinning disconnections during the growth of mature twins can be found in Refs. [70, 73, 154], our work further reveals that solute atoms also dramatically influence twin embryo growth. Ultimately, the stochastic events of disconnection nucleation and pinning/unpinning drive the growth of twin embryos, leading to the stochastic selection of different twin variants at an early stage of twin embryo growth.
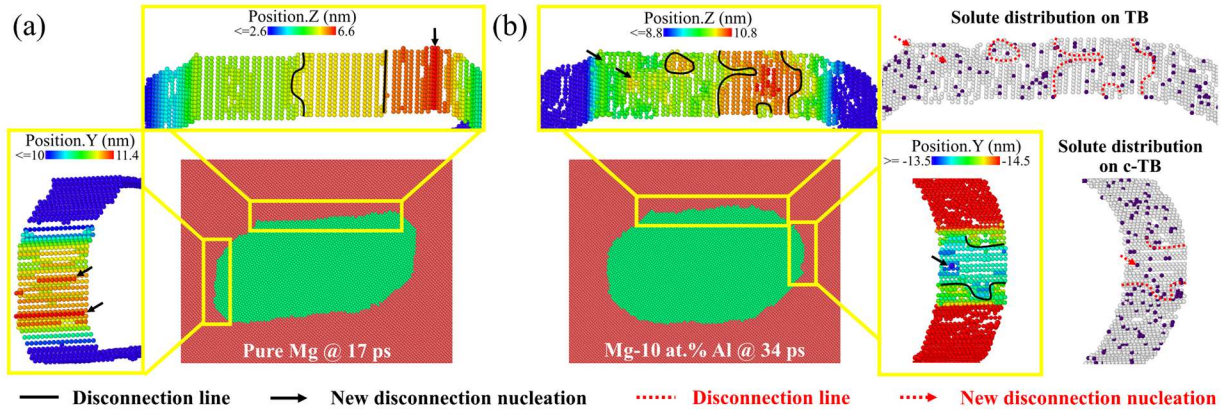


Fig. 5.6 Twinning disconnections formed on a TB and a c-TB in (a) pure Mg and (b) Mg-10 at.% Al samples. Atoms are colored using their Y positions in the enlarged views of c-TBs, while they are colored using their Z positions in the enlarged views of TBs. Solid black lines show disconnection lines, while black arrows show the nucleation of new twinning disconnections. In (b), solute distribution on the TB and c-TB is shown, with solute atoms being colored in dark purple. The disconnection lines and nucleation of twinning disconnections are marked by red dashed lines and red dashed arrows, respectively.

### 5.3 Segregated solutes lead to anisotropy in faceted twin boundary migration

### 5.3.1 Computational Methods

Based on the experimental observations (see Fig. 5.7), MD simulations are used to answer questions such as whether it is an energetically favorable process to have Y

segregation and clustering near the faceted TB, and what the influences of Y-clusters are on twin boundary migration. To create a faceted TB, we start from two triclinic simulation cells each containing two twin boundaries as shown in Fig. 5.8. The X-axis of the cell is along the $[1\bar{2}10]$-direction and the Y-axis is along the twinning direction, $[10\bar{1}1]$-direction. The dimensions of the simulation cells are around $5.1 \times 45.5 \times 60.1$ nm$^3$ in the X, Y, and Z directions with the periodic boundary condition being applied to all directions. The positions of twin boundaries in two samples are slightly different, with the twin boundaries in one sample being $\sim$1.14 nm higher than the twin boundaries in the other sample. Two simulation cells are then joined together, and before energy minimization, the atoms at the joining area are recognized as non-hcp atoms. Energy minimization is then applied to structurally relax the sample, and two facets are formed on each twin boundary. In our simulation, the BP interface is around 1.63 nm, which is very close to experimental observation. Note that in pure Mg samples, these facets are not stable, they will eventually be dissociated into three individual twinning disconnections. Since in this work, we attempt to explain phenomena occurring at such a faceted structural feature, a configuration of the facet before its dissociation is taken for following studies. To reduce the computation load, a smaller simulation cell is taken from the larger sample, and the migration behavior can be fully captured even though smaller samples are used. The dimensions of the smaller simulation box are around $5.1 \times 50.1 \times 50.0$ nm$^3$ in the X, Y, and Z directions with the periodic boundary condition being applied to the X direction. The sample contains $\sim$560,000 atoms. An enlarged view of the faceted TB is presented in Fig. 5.9(a). MD simulations are conducted using an EAM potential developed by Sheng et al. [155].
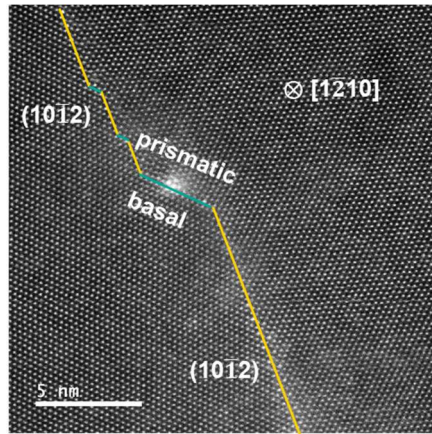
Fig. 5.7 HAADF-STEM image of the Y distribution near the faceted twin boundary [151].
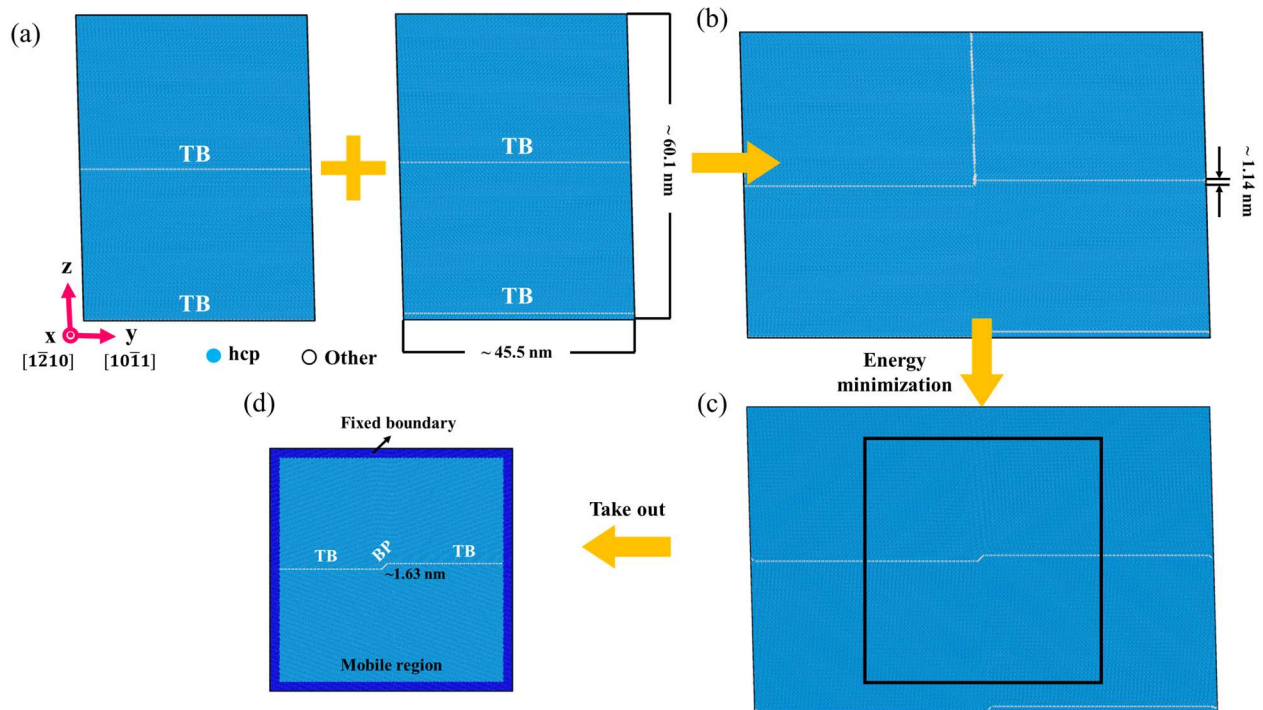


Fig. 5.8 (a)-(c) Procedures of forming the faceted twin boundary. (d) An atomic snapshot of the simulation cell used for this work.

To initiate twin boundary motion, a constant shear strain is applied uniformly by displacing all atoms in the simulation box. A schematic for the simulations on twin boundary motion is shown in Fig. 5.10(a). Atoms within a 2 nm-band around the edge of the simulation

box are fixed to maintain the constant shear strain during the simulation. Shear strains ranging from 2% ~ 8% are used. Atoms are relaxed under an NVT ensemble at 1 K, with the temperature adjusted every 100 time steps with one integration step of 0.1 fs. Visualization of atomic configurations is performed in the same way as mentioned in Chapter 4 to characterize the local crystalline structure and orientation associated with each atom in the system. Atoms on one side of the twin boundary are then differentiated from atoms on the other side using the orientation information, with atoms in the upper region (refer as "matrix") colored red and those in the lower region (refer as "twin") colored green. When showing structural information, atoms with an hcp structural environment are colored blue, those with an fcc structural environment are colored green, while atoms at the boundaries are colored in white. Y solutes are colored in dark purple.

### 5.3.2 Results and Discussion

To obtain the segregation tendency of a single Y atom to lattice sites near the BP interface, one Mg atom in the vicinity of the BP interface is replaced by a Y atom. The segregation energy, $\Delta E_{seg}$, is then calculated as the energy difference before and after segregation to certain lattice sites occurs. The following equation, Eq. (11), is used, and results are shown in Fig. 5.9(b).

$$\Delta E_{seg} = (E_{Twin}(Mg_{n-1}Y_1) - E_{Twin}(Mg_n)) - 1 \cdot (E_{Bulk}(Mg_{n-1}Y_1) - E_{Bulk}(Mg_n)) \qquad (11)$$

where $E_{Twin}(Mg_{n-1}Y_1)$ is the energy of a sample with the faceted twin boundary and one Y dopant, $E_{Twin}(Mg_n)$ is the energy of a pure Mg sample with the faceted twin boundary. $E_{Bulk}(Mg_{n-1}Y_1)$ is the energy of a sample without the faceted twin boundary and one Y dopant, while $E_{Bulk}(Mg_n)$ is the energy of a pure Mg sample without the faceted twin boundary. A

negative value of segregation energy indicates a preference for segregation, while a positive value predicts grain boundary depletion. The atomic hydrostatic stress of the same region is presented in Fig. 5.9(c). The hydrostatic stress is the average of three normal stresses and its magnitude measures the degree of lattice distortion. In Fig. 5.9(c), positive values indicate lattice sites under tension. Obvious correlations between the distribution of segregation energies and atomic hydrostatic stresses are found. Fig. 5.9(b) shows that there are two types of lattice sites on the twin boundary and BP interface, one strongly prefers Y segregation while the other would prefer to be depleted. The lattice sites favorable for Y segregation correspond to those under tension shown in Fig. 5.9(c). It is reported that the atomic radius of Y is ~12.45% larger than the atomic radius of Mg [156], so the occupation of Y to positions under tension can reduce lattice distortion, which in turn reduces the energy of the whole system. Two factors contribute to the final segregation energy [157, 158], one is the reduction of lattice distortion due to solute segregation (volumetric contribution), and the other is the change of local chemical bonding for solute atom being at the target spot versus the solute being in the bulk (chemical contribution). Since in pure Mg samples, the BP facet is not the most stable state and is dissociated into individual twinning disconnections during energy minimization, we neglect the chemical contribution, which also plays less important role for metallic systems due to the fact that atoms are embedded in an electron sea. Some sites above the BP interface also exhibit a preference for Y segregation, again corresponding to lattice sites under tension. The closer a spot to the BP interface, the higher the segregation tendency. The reason for the existence of these lattice sites under tension can be traced back to how the BP interface is formed. Basic hcp crystallography shows that the repeating unit of the basal lattice has a slightly larger lattice

97

constant ( $\sqrt{3}a$, where $a$ is the $\langle 11\bar{2}0 \rangle$ lattice parameter of Mg, with a value of 0.320 nm [159]) than the repeating unit of the prismatic lattice ($c$, where $c$ is the $\langle 0001 \rangle$ lattice parameter of Mg, with a value of 0.520 nm [159]). To form the BP interface, the prismatic lattice is stretched to match the basal lattice. Our simulation results show that the expanded lattice sites on the twin boundary as well as on the BP interface have the strongest preference for solute segregation, indicating a start of Y clustering. We note that real materials can also nucleate defects such as dislocations to relax the local stress state, but this is not explicitly treated here.

The segregation energy of Y at the expanded lattice sites on the twin boundary has also been studied using density functional theory (DFT) [157]. The DFT-computed values using two samples of different sizes are -0.288 eV and -0.276 eV. To compare with the DFT data, additional calculations are performed to fully relax the local structure surrounding the solute, and the segregation energy obtained is -0.31 eV. Our results are close to what is reported and demonstrate the ability of the interatomic potential on reproducing such information.
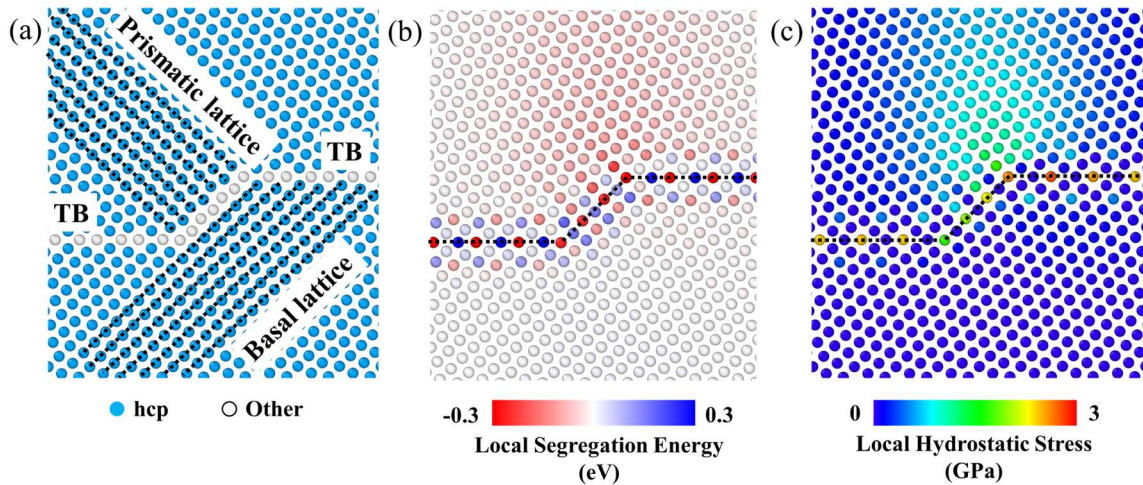
Fig. 5.9 (a) The atomic structure of the BP facet on the twin boundary. Basal planes on both sides of the faceted twin boundary are marked using black dashed lines. (b) The distribution of Y segregation energy. (c) The distribution of atomic hydrostatic stress for the same region. In (b) and (c), the twin boundary and BP interface are marked using black dashed lines.

The faceted twin boundary migration with and without the presence of Y solutes is then explored. The boundary position is plotted against time for pure Mg samples in Fig. 5.10. Here we selected the part of boundary away from the edges of the simulation box for analysis, to avoid the influence of the fixed boundary on twin boundary motion. The faceted twin boundary in pure Mg samples are easy to move, and its motion starts from releasing twinning disconnections. In Fig. 5.10, all the curves start from the same initial position (~0.0 nm), and the curves for positive shear strains go up, meaning that the boundary moves upward at positive shear strains, while those curves for negative shear strains go down, meaning that the boundary moves downward at negative shear strains. Eventually all the boundaries reach a stable position, signaling by the plateaus. Most importantly curves for the same amount of shear strains are symmetric around the initial position of the twin boundary, in contrast to the twin boundary migration in Mg-Y samples (shown in Fig. 5.11(a)). In Mg-Y samples, a Y-cluster is created at the BP interface by replacing Mg atoms at 50% of those lattice sites with larger volume by Y atoms. 50% of the expanded lattice sites on the twin boundary are also occupied by Y atoms, being consistent with experimental observations. Although the same shear strain is applied, the faceted twin boundary in Mg-Y samples moves slower due to the pinning effect of Y solutes on the twin boundary and BP interface. In addition, the presence of Y atoms at the twin boundary and the Y-cluster leads

to anisotropy in boundary motion. Twin growth occurs through the nucleation and migration of twinning dislocations, and BP interfaces are reported as a source of generating twinning dislocations [55]. Our results show that the existence of segregated Y solutes at twin boundaries and BP interfaces can alter the further twinning or detwinning of existing twins. For example, the lower part of the sample is considered as the twinned-region according to our notation, the Y-cluster at the BP interface creates difficulties for the faceted twin boundary to move up, which means further twin growth is more difficult to occur. Fig. 5.11(b) shows the local atomic structure of the BP interface in different samples. While in samples deformed at 8% shear strain, the twin boundary stays immobile. In samples deformed at -8% shear strain, the boundary can become unppined from the Y solutes at the BP interface and begin to migrate.
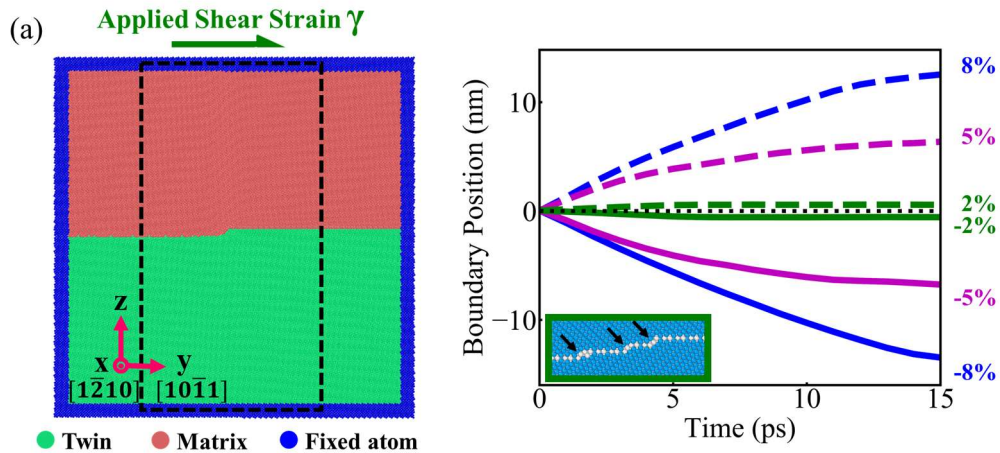


Fig. 5.10 (a) A schematic of the simulation cell for shear deformation. Atoms colored in dark blue are fixed during simulation, while atoms in the mobile region are colored according to their lattice orientation. The green arrow on the top shows the direction of the positive shear strain/stress. The rectangle shown by the black dashed line marks the part of the boundary used to calculate the average boundary position. (b) Boundary position versus time for pure

Mg samples deformed at different shear strains. The inset shows the dissociation of the BP interface into twinning disconnections (marked using black arrows).
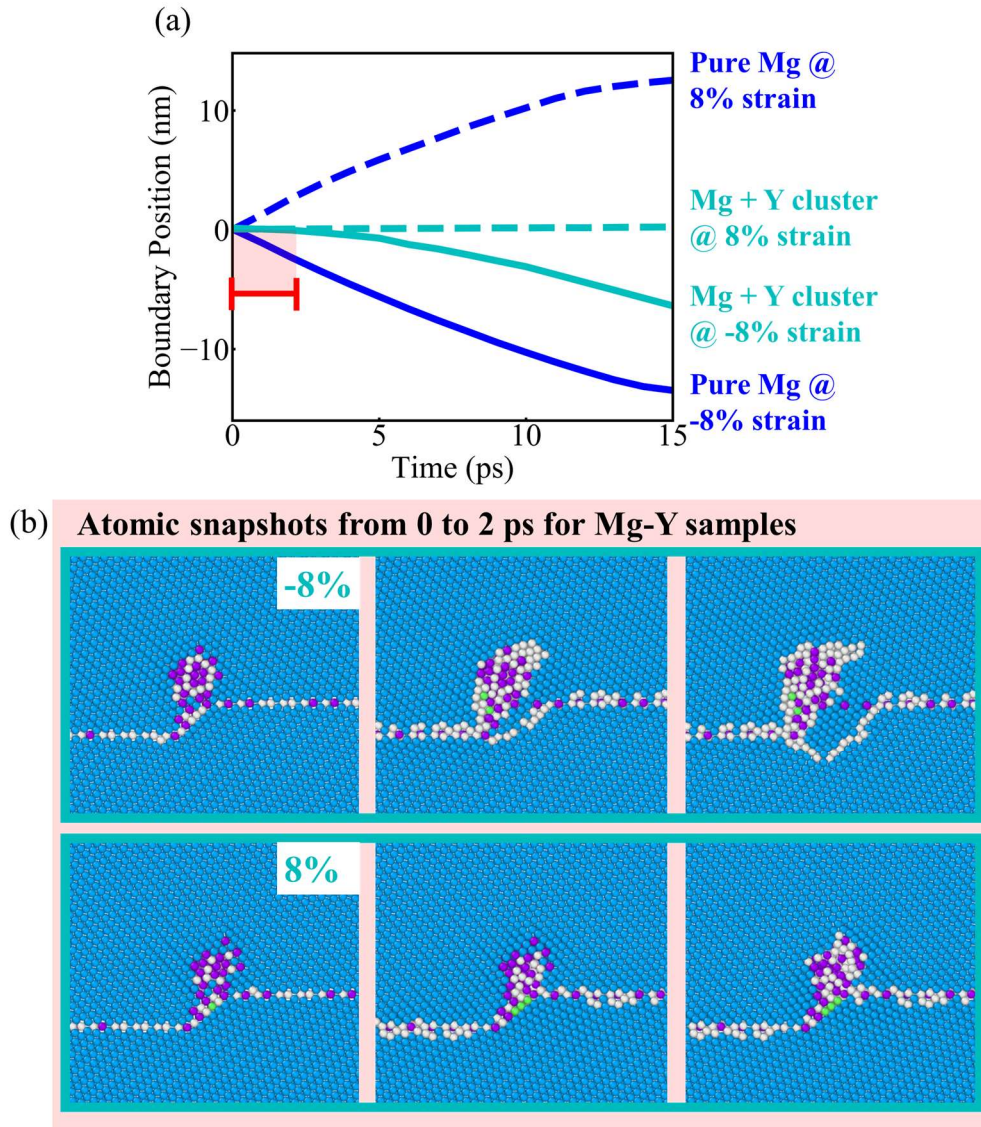


Fig. 5.11 (a) Boundary position versus time for pure Mg and Mg-Y samples deformed at ±8% shear strain. (b) Local atomic structure of the BP interface from 0 to 2 ps for Mg-Y samples deformed at ±8% shear strain, and the pure Mg sample deformed at -8% shear strain. hcp atoms are colored blue, fcc atoms are colored green, while atoms at the boundaries are

colored white due to their local structure. Black arrows show the individual twinning disconnection formed from the BP interface.

## *5.4 Conclusions*

In summary, we explored the solute effect on twin embryo growth as well as the motion of faceted twin boundaries using atomistic simulations. In these two cases, solid solution additions and segregated solute atoms are considered respectively, and two alloying elements, Al and Y are used. The following conclusions can be drawn from this work:

- We have discovered a process of random variant selection between $(\bar{1}012)$ and $(10\bar{1}2)$ co-zone twins in Mg-Al alloys after Al concentration reaches a critical level.

- The twin embryo growth can be separated into two stages: (1) the stochastic incubation stage when embryos choose which twin variants to eventually adopt, and (2) the deterministic growth stage when embryos expand without changing the selected twin variant.

- The stochastic twin variant selection is caused by the stochastic events of nucleation and pinning/unpinning of twinning disconnections by solute atoms.

These findings reveal a previously unknown effect of alloying on twinning and thereby benefit continuously emerging strategies for improving Mg properties via alloy design. We also note that this stochastic twin variant selection could be used for the construction of twin meshes. Forming twin meshes requires twins that grow in different directions and intersect each other, which can be accomplished by random twin variant selection in Mg alloys even for the same macroscopic stress state.

## Chapter 6: Conclusions

Grain boundary phenomena have been attracting researchers' attention for decades. In polycrystalline alloys, solute-grain boundary interactions inevitably occur and further alter bulk properties. The studies of such interactions are not only exciting examples of fundamental science, but also of engineering purposes. The changed grain boundary chemistry, structure or migration mechanisms may lead to enhancement in overall strength, ductility, cohesion, sintering properties and so on. In this thesis, with a primary focus on solute-induced grain boundary structure change and solute altered migration behaviors, the following conclusions can be summarized.

- Chapter 2: Based on existing experimental results on Cu-Zr nanoalloys, the ability of four interatomic potentials to model interfacial segregation and structural transitions was tested. The selection criteria of accurate interatomic potentials for modeling was then set up. Such potentials can give good reproduction on liquid enthalpy of mixing and bond energies. To obtain precise values of these parameters, experimental or first-principles data from multiple phases and material states should be included in the fitting database used to create the cross-potential terms.

- Chapter 3: The possibility of forming thicker AIFs in two model ternary alloys, Cu-Zr-Ag and Al-Zr-Cu, was investigated. Different segregation behaviors of different dopant elements are observed. While Zr and Ag compete for limited segregation sites at ordered Cu grain boundaries, Zr and Cu exhibit co-segregation to ordered Al grain boundaries. Zr and Ag can both induce a structural transformation to disordered grain boundaries in Cu-based alloys, yet only Cu possess the same ability in Al-based alloys. Thicker AIFs are found in Al-9.5 at.% Zr-0.5 at.% Cu alloys.

103

- Chapter 4: The atomistic growth mechanisms of a twin embryo in a single crystal of pure Mg was first explored. We found constant twin tip velocity and twinning disconnection velocity for constant shear strain, and a much longer disconnection propagation time than nucleation time on the twin boundary. These results are then used for developing a phenomenological model to bridge between atomistic simulations and available experimental results. A logarithmic relation between twin thickness and time was derived and fitted well MD data. The ratio of disconnection velocity to twin tip velocity obtained from experiments follows the trend predicted by MD data, which proves the validity of our MD results as well as the robustness of the phenomenological model.

- Chapter 5: As the focus of Chapter 4 is on the atomistic growth mechanisms of twin embryo in pure Mg, the solute effect on overall twin embryo growth and the migration of faceted twin boundaries were investigated in this chapter. Randomly distributed Al atoms were demonstrated to add stochasticity in twin embryo growth. Analysis on three hundred and sixty simulations on alloys at six different concentrations shows the possibility of forming multiple twin variants after solute concentration reaches a certain level, while only one twin variant appears in pure Mg simulations. Y segregation to twin boundary and BP/PB interfaces are proven to be energetically favorable and reduce local lattice distortion. These Y atoms also lead to anisotropy in twin boundary migration, which changes the further twinning or detwinning of existing twins.

As a whole, this thesis shows that it is essential to understand solute-grain boundary interactions in alloys to explain various material responses, and to provide guidance for material design through alloying.

# Chapter 7: Future work

This thesis represents an important step towards a comprehensive understanding of the solute-grain boundary interactions in two important grain boundary phenomena, grain boundary segregation and grain boundary migration. However, a number of gaps still exist in our current knowledge, and a plethora of research opportunities are left. Future works could be directed in the following specific areas:

- The formation of AIFs introduces two interfaces between the abutting crystal and the amorphous phase. It is interesting to know the difference in structure and chemistry between areas near the interfaces and the bulk phase, or between areas near the interfaces and the center of the AIF. In addition, how these interfaces contribute to the overall properties of materials is also an interesting question.

- Despite the efforts in identifying individual grain boundary complexion, there is a lacking knowledge on the transition between different complexion types. Though some theoretical works have proposed possible transitions in both pure metals and metallic alloys [25, 160, 161], more experimental support and validation (especially in situ experiments) need to be given.

- Solute effect on twin-twin interactions. In our current work, the growth of a single twin embryo is considered. However, EBSD images on twin morphology show that multiple twins form in single grains. As one twin approaches another twin, the stress field around them starts to interact strongly, which either inhibits or promotes the growth of each other [74, 75]. Moreover, as twin-twin intersection occurs, some interfaces at the twin embryo boundary disappear, while new interfaces are formed. For example, Yu et al. reported the formation of low-angle twin–twin boundaries, one

closely parallel to the basal plane while the other closely parallel to the prismatic plane, as two $\{10\bar{1}2\}$ co-zone twins intersect [137]. It would be interesting to know how these processes are affected by introducing solute atoms.

- Growth of 3D twin embryos in Mg alloys. To date, most of the experimental microstructure characterization of Mg and Mg alloys has been performed by 2D microscopy techniques, as well as theoretical studies are conducted on 2D morphology of twins. However, recent works show that ignorance of the third dimension may result in a faulty description of twin morphology [162, 163], and thus important aspects of twin nucleation and growth mechanism are missed. While 2D microstructure characterization shows that all twins exhibit a lamellar structure [137], 3D microstructure characterization reveals different shapes of twins with different Schmid factors [163]. With twins of low Schmid factors adopting irregular shapes, their thicknesses vary significantly as twins span, which makes twin thickness measurement based on the 2D characterization lead to significant deviations from the 3D twin thickness. In addition, the habit planes which bound tension twins can significantly deviate from the ideal $\{10\bar{1}2\}$ planes [162]. It is hard for 2D microstructure characterization to capture the real twin habit planes, much less to say providing explanations of forming these habit planes. Therefore, in-depth investigations of twin growth considering the 3D twin morphology need to be conducted. Current few works of atomistic simulations using 3D embryos were performed on characterizing the microstructure of the "dark side" of tension twins [164], exploring the interaction between tension twins and basal <a> dislocations [165], and investigating the formation of large basal-prismatic facets [166]. These

works mentioned above proves the feasibility of using 3D embryos to study twinning behaviors in Mg. Yet we noticed that in these simulations, twin growth is initiated by applied shear, while it is known that twinning behaviors depend on the strain path. As shown in the work of Ram et al. [162], tension twins obtained by stretching the c-axis or compressing along a direction perpendicular to the c-axis exhibit different morphologies. Therefore, more systematic studies considering different loading conditions need to be performed. Moreover, twinning disconnections are considered as important structural features in twin nucleation and propagation, and the effect of solute atoms are reported to both induce disconnection nucleation and suppress disconnection propagation [167]. For 3D twin configurations, new interfaces such as twist prismatic–prismatic boundaries and twist pyramidal–pyramidal boundaries are found and different types of disconnections are formed on these interfaces [162, 146], how differently solutes influence the nucleation and migration of different disconnections and lead to the overall twin growth needs to be further discussed.

- Combining atomistic simulations with continuum modeling to give a full picture of twinning process in Mg alloys. Our current work focuses on the growth of small twin embryos occurring at the nanometer scale. However, twins can expand into sizes at micrometer scale and span the entire grain, they terminate at grain boundaries and cause stress concentration which induces twinning in nearby grains and form paired twins [76, 77]. These features may span over several grains and form huge twin chains [140], which cannot be captured in atomistic simulations. On the contrary, phase field models and crystal plasticity models are known for studying microstructure evolution in polycrystalline samples with reasonable time

consumption and computation costs [168, 169]. Therefore, combining atomistic simulations and continuum modeling becomes a necessity to probe phenomena occurring at different length-scale.

# References

[1] D. McLean, Grain boundaries in metals, Oxford University (1957).

[2] A.P. Sutton and R.W. Balluffi, Interfaces in crystalline materials, OUP Oxford, New York (2006).

[3] V. Randle, The measurement of grain boundary geometry, Institute of Physics Pub (1993).

[4] J.M. Howe, Interfaces in materials: atomic structure, thermodynamics and kinetics of solid-vapor, solid-liquid and solid-solid interfaces, Wiley-Interscience (1997).

[5] G. Gottstein and L.S. Shvindlerman, Grain boundary migration in metals: thermodynamics, kinetics, applications, CRC press (2009).

[6] D. Wolf and J. Jaszczak, Materials interfaces: atomic-level structure and properties, Springer Science & Business Media (1992).

[7] P. Kwapuliński, J. Rasek and J. W. Moroń, The kinetics of structural defect recovery in pure iron in the temperature interval 300 to 800 K, Phys Status Solidi A 88(2) (1985) 561.

[8] H. Djohari and J.J. Derby, Transport mechanisms and densification during sintering: II. Grain boundaries. Chem Eng Sci 64(17) (2009) 3810-3816.

[9] M.A. Meyers, A. Mishra, D.J. Benson, Mechanical properties of nanocrystalline materials, Prog Mater Sci 51(4) (2006) 427-556.

[10] K.S. Kumar, H. Van Swygenhoven, S. Suresh, Mechanical behavior of nanocrystalline metals and alloys, Acta Mater 51(19) (2003) 5743-74.

[11] M. Dao, L. Lu, R.J. Asaro, J.T. De Hosson, E. Ma, Toward a quantitative understanding of mechanical behavior of nanocrystalline metals, Acta Mater 55(12) (2007) 4041-65.

[12] S.N. Mathaudhu, B.L. Boyce, Thermal stability: the next frontier for nanocrystalline materials, JOM 67(12) (2015) 2785-7.

[13] A.R. Kalidindi, T. Chookajorn, C.A. Schuh, Nanocrystalline materials at equilibrium: a thermodynamic review, JOM 67(12) (2015) 2834-43.

[14] H.R. Peng, M.M. Gong, Y.Z. Chen, F. Liu, Thermal stability of nanocrystalline materials: thermodynamics and kinetics, Int Mater Rev 62(6) (2017) 303-33.

[15] M. Rajagopalan, K. Darling, S. Turnage, R.K. Koju, B. Hornbuckle, Y. Mishin, K.N. Solanki, Microstructural evolution in a nanocrystalline Cu-Ta alloy: A combined in-situ TEM and atomistic study, Mater Des 113(5) (2017) 178-85.

[16] Y. Huang, A. Menovsky, F. De Boer, Calorimetric analysis of the grain growth in nanocrystalline copper samples, Nanostruct Mater 2(6) (1993) 587-595.

[17] S. Simões, R. Calinas, P.J. Ferreira, M.T. Vieira, F. Viana, M.F. Vieira, Effect of annealing conditions on the grain size of nanocrystalline copper thin films, Mater Sci Forum, 587 (2008) 483-487, Trans Tech Publications Ltd

[18] J.F. Nie, Y.M. Zhu, J.Z. Liu, and X.Y. Fang, Periodic segregation of solute atoms in fully coherent twin boundaries. Science, 340(6135) (2013) 957-960.

[19] S. Hoffman, Segregation of grain boundaries, P.A. Dowben, A. Miller (Eds.), Surface segregation phenomena, CRC Press, Boca Raton (1990), pp. 107-1134.

[20] D. Raabe, M. Herbig, S. Sandlobes, Y. Li, D. Tytko, M. Kuzmina, D. Ponge and P.P. Choi, Grain boundary segregation engineering in metallic alloys: A pathway to the design of interfaces, Curr Opin Solid St M, 18(4) (2014) 253-61.

[21] M.P. Seah, Grain-Boundary Segregation, J Phys F Met Phys, 10(6) (1980) 1043-64.

[22] P. Wynblatt and R.C. Ku, Surface-Energy and Solute Strain-Energy Effects in Surface Segregation. Surf Sci 65(2) (1977) 11-31.

[23] P. Wynblatt and D. Chatain, Anisotropy of segregation at grain boundaries and surfaces. Metall Mater Trans A, 37(9) (2006) 2595-2620.

[24] M.P. Harmer, The Phase Behavior of Interfaces, Science, 332(6026) (2011) 182-3.

[25] T. Frolov, M. Asta, Y. Mishin, Segregation-induced phase transformations in grain boundaries. Phys Rev B 92(2) (2015) 020103.

[26] Z.L. Pan and T.J. Rupert, Effect of grain boundary character on segregation-induced structural transitions. Phys Rev B, 93(13) (2016) 134113.

[27] S.J. Dillon, M. Tang, W.C. Carter and M.P. Harmer, Complexion: A new concept for kinetic engineering in materials science, Acta Mater 55(18) (2007) 6208-18.

[28] P.R. Cantwell, M. Tang, S.J. Dillon, J. Luo, Rohrer GS and Harmer MP, Grain boundary complexions, Acta Mater 62 (2014) 1-48.

[29] A. Khalajhedayati, Z.L. Pan, T.J. Rupert, Manipulating the interfacial structure of nanomaterials to achieve a unique combination of strength and ductility, Nat Commun 7(1) (2016) 10802.

[30] P.L. Williams, Y. Mishin, Thermodynamics of grain boundary premelting in alloys. II. Atomistic simulation, Acta Mater 57(13) (2009) 3786-3794.

[31] J.D. Schuler, T.J. Rupert, Materials selection rules for amorphous complexion formation in binary metallic alloys, Acta Mater 140 (2017) 196-205.

[32] A. Khalajhedayati, T.J. Rupert, High-temperature stability and grain boundary complexion formation in a nanocrystalline Cu-Zr alloy, JOM 67(12) (2015) 788-801.

[33] Z. Pan, T.J. Rupert, Amorphous intergranular films as toughening structural features, Acta Mater 89 (2015) 205-14.

[34] W.J. Joost, 2017. Targeting high impact R&D for automotive magnesium alloys. In Magnesium Technology 2017 (pp. 5-6). Springer, Cham.

[35] H. Dieringa, N. Hort, D. Letzig, J. Bohlen, D. Höche, C. Blawert, M. Zheludkevich, and K.U. Kainer, 2018, March. Mg Alloys: Challenges and Achievements in Controlling Performance, and Future Application Perspectives. In TMS Annual Meeting & Exhibition (pp. 3-14). Springer, Cham.

[36] B.L. Mordike and T. Ebert, 2001. Magnesium: properties—applications—potential. Mater Sci Eng A 302(1) 37-45.

[37] T.M. Pollock, Weight loss with magnesium alloys, Science 328(5981) (2010) 986-987

[38] T. Dursun, and C. Soutis, Recent developments in advanced aircraft aluminium alloys. Materials & Design (1980-2015), 56 (2014) 862-871.

[39] A.S. Warren, Developments and challenges for aluminum--A Boeing perspective. In Materials Forum (2004) (Vol. 28, pp. 24-31).

[40] R. Von Mises, Mechanics of plastic deformation of crystals. Z. Angew. Math. Mech, 8(3) (1928) 161-85.

[41] G.S. Rohrer, 2001. Structure and bonding in crystalline materials. Cambridge University Press.

[42] E. Schmid, Contribution to the Physics and Metallography of Magnesium, Z Electr Chem 37 (1931) 447.

[43] P.W. Bakarian, C.H. Mathewson, Slip and twinning in Magnesium single crystals at elevated temperatures, Trans Metall Soc AIME 152 (1943) 226.

[44] R.E. Reed-Hill, W.D. Robertson, Deformation of magnesium single crystals by non basal slip, JOM 9(4) (1957) 496–502.

[45] P. Ward Flynn, J. Mote, J.E. Dorn, On the thermally activated mechanism of prismatic slip in magnesium single crystals, Trans Metall Soc AIME 221(6) (1961) 1148-1154

[46] K.Y. Xie, Z. Alam, A. Caffee, and K.J. Hemker, Pyramidal I slip in c-axis compressed Mg single crystals, Scr Mater 112 (2016) 75-78.

[47] K.H. Kim, J.B. Jeon, N.J. Kim, and B.J. Lee, Role of yttrium in activation of < c+ a> slip in magnesium: An atomistic approach, Scr Mater 108 (2015) 104-108.

[48] Z. Wu, and W.A. Curtin, The origins of high hardening and low ductility in magnesium, Nature 526(7571) (2015) 62-67.

[49] Z. Wu, R. Ahmad, B. Yin, S. Sandlöbes, and W.A. Curtin, Mechanistic origin and prediction of enhanced ductility in magnesium alloys, Science, 359(6374) (2018) 447-452.

[50] H. Fan and J.A. El-Awady, Molecular dynamics simulations of orientation effects during tension, compression, and bending deformations of magnesium nanocrystals, J Appl Mech 82(10) (2015) 101006.

[51] M. D. Nave and M. R. Barnett, Microstructures and textures of pure magnesium deformed in plane-strain compression, Scr Mater 51 (2004) 881.

[52] S. G. Hong, S. H. Park, and C. S. Lee, Role of {10$\bar{1}$2} twinning characteristics in the deformation behavior of a polycrystalline magnesium alloy, Acta Mater 58 (2010) 5873.

[53] M. G. Jiang, C. Xu, H. Yan, G. H. Fan, T. Nakata, C. S. Lao, R. S. Chen, S. Kamado, E. H. Han, and B. H. Lu, Unveiling the formation of basal texture variations based on twinning and dynamic recrystallization in AZ31 magnesium alloy during extrusion, Acta Mater 157 (2018) 53.

[54] J. Wang, I. Beyerlein, C. Tomé, An atomic and probabilistic perspective on twin nucleation in Mg, Scr Mater 63(7) (2010) 741-746.

[55] H. El Kadiri, C.D. Barrett, J. Wang, C.N. Tomé, Why are twins profuse in magnesium? Acta Mater 85 (2015) 354-361.

[56] H. El Kadiri, C.D. Barrett, M.A. Tschopp, The candidacy of shuffle and shear during compound twinning in hexagonal close-packed structures, Acta Mater 61(20) (2013) 7646-7659.

[57] A. Serra, D. Bacon, R. Pond, Twins as barriers to basal slip in hexagonal-close-packed metals, Metall Mater Trans A 33(13) (2002) 809-812.

[58] A. Serra, D. Bacon, A new model for {10$\bar{1}$2} twin growth in hcp metals, Philos Mag 73(2) (1996) 333-343.

[59] R. Pond, A. Serra, D. Bacon, Dislocations in interfaces in the hcp metals—II. Mechanisms of defect mobility under stress, Acta Mater 47(5) (1999) 1441-1453.

[60] E. Orowan, Dislocations and mechanical properties, in: M. Cohen (Ed.), Dislocations in Metals, AIME, New York, (1954) pp. 69–195.

[61] N. Thompson, D. Millard, XXXVIII. Twin formation, in cadmium, Philos Mag 43(339) (1952) 422-440.

[62] S. Mendelson, Dislocation dissociations in hcp metals, J Appl Phys 41(5) (1970) 1893-1910.

[63] S. Mendelson, Zonal dislocations and twin lamellae in hcp metals, Mater Sci Eng 4(4) (1969) 231-242.

[64] J. Wang, R. Hoagland, J. Hirth, L. Capolungo, I. Beyerlein, C. Tomé, Nucleation of a ($\bar{1}$012) twin in hexagonal close-packed crystals, Scr Mater 61(9) (2009) 903-906.

[65] J. Wang, S. Yadav, J. Hirth, C. Tomé, I. Beyerlein, Pure-shuffle nucleation of deformation twins in hexagonal-close-packed metals, Mater Res Lett 1(3) (2013) 126-132.

[66] J. Tu, X. Zhang, J. Wang, Q. Sun, Q. Liu, C.N. Tomé, Structural characterization of {10$\bar{1}$2} twin boundaries in cobalt, Appl Phys Lett 103(5) (2013) 051903.

[67] Y. Liu, N. Li, S. Shao, M. Gong, J. Wang, R. McCabe, Y. Jiang, C. Tomé, Characterizing the boundary lateral to the shear direction of deformation twins in magnesium, Nat Commun 7(1) (2016) 1-6.

[68] J. Wang, J. Hirth, C. Tomé, ($\bar{1}$012) Twinning nucleation mechanisms in hexagonal-close packed crystals, Acta Mater 57(18) (2009) 5521-5530.

[69] A. Ostapovets, R. Gröger, Twinning disconnections and basal–prismatic twin boundary in magnesium, Model Simul Mater Sci Eng 22(2) (2014) 025015.

[70] A. Luque, M. Ghazisaeidi, W.A. Curtin, A new mechanism for twin growth in Mg alloys, Acta Mater 81 (2014) 442-456.

[71] J. Hirth, J. Wang, C. Tomé, Disconnections and other defects associated with twin interfaces, Prog Mater Sci 83 (2016) 417-471.

[72] L. Capolungo, I. Beyerlein, C. Tomé, Slip-assisted twin growth in hexagonal close-packed metals, Scr Mater 60(1) (2009) 32-35.

[73] D.E. Spearot, L. Capolungo, C.N. Tome, Shear-driven motion of Mg {10$\bar{1}$2} twin boundaries via disconnection terrace nucleation, growth, and coalescence, Phys Rev Mater 3(5) (2019) 053606.

[74] M. Arul Kumar, I.J. Beyerlein, R.A. Lebensohn, C.N. Tome, Role of alloying elements on twin growth and twin transmission in magnesium alloys, Mat Sci Eng a-Struct 706 (2017) 295-303.

[75] M. Arul Kumar, I.J. Beyerlein, C.N. Tomé, Effect of local stress fields on twin characteristics in HCP metals, Acta Mater 116 (2016) 143-154.

[76] M. Arul Kumar, I.J. Beyerlein, R.J. McCabe, C.N. Tome, Grain neighbour effects on twin transmission in hexagonal close-packed materials, Nat Commun 7(1) (2016) 1-9.

[77] I. Chelladurai, D. Adams, D.T. Fullwood, M.P. Miles, S. Niezgoda, I.J. Beyerlein, M. Knezevic, Modeling of trans-grain twin transmission in AZ31 via a neighborhood-based viscoplastic self-consistent model, Int J Plasticity 117 (2019) 21-32.

[78] M.T. Dove, An introduction to atomistic simulation methods. Seminarios de la SEM. 4:7-37 (2008).

[79] C.R. Weinberger and G.J. Tucker eds., Multiscale materials modeling for nanomechanics, Switzerland: Springer, 245: (2016).

[80] J. Du and J.M. Rimsza, Atomistic computer simulations of water interactions and dissolution of inorganic glasses, npj Mater Degrad 1(1) (2017) 1-12.

[81] J. Grigera, Molecular dynamics simulation for ligand-receptor studies. Carbohydrates interactions in aqueous solutions, Curr Pharm Des 8(17) (2002) 1579-1604.

[82] B. Sadigh, P. Erhart, A. Stukowski, A. Caro, E. Martinez and L. Zepeda-Ruiz, Scalable parallel Monte Carlo algorithm for atomistic simulations of precipitation in alloys, Phys Rev B 85(18) (2012) 184203.

[83] Y. Mishin, Calculation of the $\gamma/\gamma'$ interface free energy in the Ni–Al system by the capillary fluctuation method, Model Simul Mater Sci Eng 22(4) (2014) 045001.

[84] G.P. Pun, V. Yamakov, Y. Mishin, Interatomic potential for the ternary Ni–Al–Co system and application to atomistic modeling of the B2–L10 martensitic transformation, Model Simul Mater Sci Eng 23(6) (2015) 065006.

[85] Y. Mishin, D. Farkas, M.J. Mehl and D.A. Papaconstantopoulos, Interatomic potentials for monoatomic metals from experimental data and ab initio calculations, Phys Rev B, 59 (1999) 3393.

[86] Y.M. Wang, A. Santana, and W. Cai, Au-Ge MEAM potential fitted to the binary phase diagram, Model Simul Mater Sci Eng 25 (2017) 025004.

[87] J. Dziedzic, S. Winczewski and J. Rybicki, Structure and properties of liquid Al-Cu alloys: Empirical potentials compared, Comp Mater Sci 114 (2016) 219-32.

[88] L. Malerba, M.C. Marinica, N. Anento, C. Bjorkas, H. Nguyen, C. Domain, F. Djurabekova, P. Olsson, K. Nordlund, A. Serra, D. Terentyev, F. Willaime and C.S. Becquart, Comparison of empirical interatomic potentials for iron applied to radiation damage studies, J Nucl Mater 406(1) (2010) 19-38.

[89] N. Zhou, T. Hu, J. Huang, and J. Luo, Stabilization of nanocrystalline alloys at high temperatures via utilizing high-entropy grain boundary complexions, Scr Mater 124 (2016) 160-163.

[90] B. Xu, L. Capolungo, D. Rodney, On the importance of prismatic/basal interfaces in the growth of $(\bar{1}012)$ twins in hexagonal close packed crystals, Scr Mater 68(11) (2013) 901-904.

[91] Q. Sun, X.Y. Zhang, Y. Ren, J. Tu, Q. Liu, Interfacial structure of $\{10\bar{1}2\}$ twin tip in deformed magnesium alloy, Scr Mater 90-91 (2014) 41-44.

[92] J. Zhang, G.Q. Xi, X. Wan, C. Fang, The dislocation-twin interaction and evolution of twin boundary in AZ31 Mg alloy, Acta Mater 133 (2017) 208-216.

[93] Y.M. Zhu, S.W. Xu, J.F. Nie, $\{10\bar{1}1\}$ Twin boundary structures in a Mg-Gd alloy, Acta Mater 143 (2018) 1-12.

[94] Y. J. Cui, Y. P. Li, Z. C. Wang, X. Ding, Y. Koizumi, H. K. Bian, L. Y. Lin, and A. Chiba, Impact of solute elements on detwinning in magnesium and its alloys, Int J Plasticity 91 (2017) 134

[95] S. Plimpton, Fast parallel algorithms for short-range molecular-dynamics, J Comput Phys 117(1) (1995) 1-19.

[96] A. Stukowski, Visualization and analysis of atomistic simulation data with OVITO-the Open Visualization Tool, Model Simul Mater Sci Eng 18 (2010) 015012.

[97] J.D. Honeycutt and H.C. Andersen, Molecular-dynamics study of melting and freezing of small Lennard-Jones clusters, J Phys Chem-US 91 (1987) 4950-63.

[98] Y.Q. Cheng, H.W. Sheng and E. Ma, Relationship between structure, dynamics, and mechanical properties in metallic glass-forming alloys, Phys Rev B 78 (2008) 014207.

[99] L. Ward, A. Agrawal, K.M. Flores and W. Windl, Rapid Production of Accurate Embedded-Atom Method Potentials for Metal Alloys, arXiv:1209.0619 (2012).

[100] X.W. Zhou, R.A. Johnson and H.N.G. Wadley, Misfit-energy-increasing dislocations in vapor-deposited CoFe/NiFe multilayers, Phys Rev B 69 (2004) 144113.

[101] M.I. Mendelev, M.J. Kramer, R.T. Ott, D.J. Sordelet, D. Yagodin and P. Popel, Development of suitable interatomic potentials for simulation of liquid and amorphous Cu–Zr alloys, Philos Mag 89(11) (2009) 967-87.

[102] M.N. Polyakov, T. Chookajorn, M. Mecklenburg, C.A. Schuh, A.M. Hodge, Sputtered Hf-Ti nanostructures: A segregation and high-temperature stability study, Acta Mater 108 (2016) 8-16.

[103] A. Jain, S.P. Ong, G. Hautier, W. Chen, W.D. Richards, S. Dacek, S. Cholia, D. Gunter, D. Skinner, G. Ceder, Commentary: the materials project: a materials genome approach to accelerating materials innovation, APL Mater, 1 (2013) 011002.

[104] M.E. Straumanis, L.S. Yu Lattice parameters, densities, expansion coefficients and perfection of structure of Cu and of Cu-in alpha phase, Acta Crystall A-Crys 25 (1969) 676-682.

[105] Z. Huang, F. Chen, Q. Shen, L. Zhang and T.J. Rupert, Uncovering the influence of common nonmetallic impurities on the stability and strength of a $\Sigma 5$ (310) grain boundary in Cu, Acta Mater 148 (2018) 110-122.

[106] M. Turchanin, Calorimetric research on the heat of formation of liquid alloys of copper with group IIIA and group IVA metals, Powder Metall Met C+ 36 (1997) 253-63.

[107] N.X. Zhou, J. Luo, Developing grain boundary diagrams for multicomponent alloys, Acta Mater 91 (2015) 202-216.

[108] A. Inoue, Stabilization of metallic supercooled liquid and bulk amorphous alloys, Acta Mater 48(1) (2000) 279-306.

[109] H.N.G. Wadley, A.X. Zhou, R.A. Johnson and M. Neurock, Mechanisms, models and methods of vapor deposition, Prog Mater Sci 46(3-4) (2001) 329-77.

[110] M.I. Mendelev, D.J. Sordelet and M.J. Kramer, Using atomistic computer simulations to analyze x-ray diffraction data from metallic glasses, J Appl Phys 102(4) (2007) 043501.

[111] F. Ercolessi and J.B. Adams, Interatomic Potentials from First-Principles Calculations: The Force-Matching Method, Europhys Lett 26 (1994) 583.

[112] H.W. Sheng, M.J. Kramer, A. Cadien, T. Fujita and M.W. Chen, Highly optimized embedded-atom-method potentials for fourteen fcc metals, Phys Rev B 83 (2011) 134118.

[113] A. Turchanin, I. Tomilin, M. Turchanin, I. Belokonenko and P. Agraval, Enthalpies of formation of liquid, amorphous, and crystalline phases in the Ni-Zr system, Russ J Phys Chem A 73(11) (1999) 1911-8.

[114] P. Nash and C. Jayanth, The Ni– Zr (Nickel-Zirconium) system, Bull Alloy Phase Diagr 5 (1984) 144-8.

[115] X.Y. Liu, W. Xu, S.M. Foiles, J.B. Adams, Atomistic studies of segregation and diffusion in Al-Cu grain boundaries, Appl Phys Lett 72(13) (1998) 1578-1580.

[116] D.T. Carpenter, M. Watanabe, K. Barmak, D.B. Williams, Low-magnification quantitative X-ray mapping of grain-boundary segregation in aluminum-4 wt.% copper by analytical electron microscopy, Microsc Microanal 5(4) (1999) 254-266.

[117] Y. Chen, N. Gao, G. Sha, S.P. Ringer, M.J. Starink, Microstructural evolution, strengthening and thermal stability of an ultrafine-grained Al-Cu-Mg alloy, Acta Mater 109 (2016) 202-212.

[118] D. Tsivoulas, J.D. Robson, Heterogeneous Zr solute segregation and Al3Zr dispersoid distributions in Al-Cu-Li alloys, Acta Mater 93 (2015) 73-86.

[119] H.B. Yan, F.X. Gan, D.Q. Huang, Evaporated Cu-Al amorphous-alloys and their phase-transition, J Non-Cryst Solids 112 (1989) 221-227.

[120] J.J. Yang, Y. Yang, K. Wu, Y.A. Chang, The formation of amorphous alloy oxides as barriers used in magnetic tunnel junctions, J Appl Phys 98(7) (2005) 074508.

[121] Y.Y. Cui, T.L. Wang, J.H. Li, Y. Dai, B.X. Liu, Thermodynamic calculation and interatomic potential to predict the favored composition region for the Cu-Zr-Al metallic glass formation, Phys Chem Chem Phys 13 (2011) 4103-4108.

[122] A. Tewari, S. Galmarini, M. Stuer, P. Bowen, Atomistic modeling of the effect of codoping on the atomistic structure of interfaces in alpha-alumina, J Eur Ceram Soc 32(11) (2012) 2935-2948.

[123] Z. Huang, F. Chen, Q. Shen, L. Zhang, and T.J. Rupert, Combined effects of nonmetallic impurities and planned metallic dopants on grain boundary energy and strength, Acta Mater 166 (2019) 113-125.

[124] X.Y. Liu, J.B. Adams, Grain-boundary segregation in Al-10%Mg alloys at hot working temperatures, Acta Mater 46(10) (1998) 3467-3476.

[125] D. Wang, H. Tan, Y. Li, Multiple maxima of GFA in three adjacent eutectics in Zr–Cu–Al alloy system – A metallographic way to pinpoint the best glass forming alloys, Acta Mater 53(10) (2005) 2969-2979.

[126] X.D. Wang, Q.K. Jiang, Q.P. Cao, J. Bednarcik, H. Franz, J.Z. Jiang, Atomic structure and glass forming ability of $Cu_{46}Zr_{46}Al_8$ bulk metallic glass, J Appl Phys 104(9) (2008) 093519.

[127] A. Inoue, W. Zhang, Formation, thermal stability and mechanical properties of Cu-Zr-Al bulk glassy alloys, Mater Trans 43(11) (2002) 2921-2925.

[128] Q. Yu, L. Qi, K. Chen, R.K. Mishra, J. Li, A.M. Minor, The Nanostructured Origin of Deformation Twinning, Nano Lett 12(2) (2012) 887-892.

[129] Z. Wu, M. Francis, W. Curtin, magnesium interatomic potential for simulating plasticity and fracture phenomena, Model Simul Mater Sci Eng 23(1) (2015) 015004.

[130] A. Stukowski, Visualization and analysis of atomistic simulation data with OVITO–the Open Visualization Tool, Model Simul Mater Sci Eng 18(1) (2009) 015012.

[131] P.M. Larsen, S. Schmidt, J. Schiøtz, Robust structural identification via polyhedral template matching, Model Simul Mater Sci Eng 24(5) (2016) 055007.

[132] B. Xu, L. Capolungo, D. Rodney, On the importance of prismatic/basal interfaces in the growth of ($\bar{1}012$) twins in hexagonal close packed crystals, Scr Mater 68(11) (2013) 901-904.

[133] S. Lay, G. Nouet, Morphology of ($01\bar{1}2$) twins in Zinc and related interfacial defects, Philos Mag 72(3) (1995) 603-617.

[134] T. Braisaz, P. Ruterana, G. Nouet, Twin tip defects related to the nucleation and growth mechanisms of the twin ($10\bar{1}2$) in Zinc characterized by high-resolution electron microscopy, Philos Mag 76(1) (1997) 63-84.

[135] Q. Zu, X.-Z. Tang, S. Xu, Y.-F. Guo, Atomistic study of nucleation and migration of the basal/prismatic interfaces in Mg single crystals, Acta Mater 130 (2017) 310-318.

[136] C.D. Barrett, H. El Kadiri, The roles of grain boundary dislocations and disclinations in the nucleation of $\{10\bar{1}2\}$ twinning, Acta Mater 63 (2014) 1-15.

[137] Q. Yu, J. Wang, Y. Jiang, R. J. McCabe, and C. N. Tomé, Co-zone $\{1\bar{1}012\}$ twin interaction in magnesium single crystal, Mater Res Lett 2(2) (2014) 82-88.

[138] J. Shen, H. Imai, B. Chen, X. Ye, J. Umeda, K. Kondoh, Deformation mechanisms of pure Mg materials fabricated by using pre-rolled powders, Mater Sci Eng A 658 (2016) 309-320.

[139] H. El Kadiri, J. Kapil, A. Oppedal, L. Hector Jr, S.R. Agnew, M. Cherkaoui, S. Vogel, The effect of twin–twin interactions on the nucleation and propagation of $\{10\bar{1}2\}$ twinning in magnesium, Acta Mater 61(10) (2013) 3549-3563.

[140] D. Culbertson, Q. Yu, and Y. Jiang, In situ observation of cross-grain twin pair formation in pure magnesium, Philos Mag Lett 98(4) (2018) 139-146.

[141] C.N. Tomé, I.J. Beyerlein, R.J. McCabe, J. Wang, Multiscale Statistical Study of Twinning in HCP Metals, in: M.F. Horstemeyer (Ed.), Integrated Computational Materials Engineering (ICME) for Metals: Concepts and Case Studies, Wiley, New York, (2018) pp. 283–336.

[142] S.Q. Zhu, H.G. Yan, X.Z. Liao, S.J. Moody, G. Sha, Y.Z. Wu, S.P. Ringer, Mechanisms for enhanced plasticity in magnesium alloys, Acta Mater 82 (2015) 344-355.

[143] S. Mahajan, G.Y. Chin, Twin-slip, twin-twin and slip-twin Interactions in Co-8 wt.% Fe alloy single-crystals, Acta Mater 21(2) (1973) 173-179.

[144] S. Mahajan, D.E. Barry, B.L. Eyre, A thin twin and its interaction with a coherent twin boundary in Copper, Philos Mag 21(169) (1970) 43-&.

[145] S. Mahajan, Evaluation of slip patterns observed in association with deformation twins in Mo-35 at% Re alloy, J Phys F Met Phys 2(1) (1972) 19-&.

[146] Y. Liu, P. Z. Tang, M. Y. Gong, R. J. McCabe, J. Wang, and C. N. Tome, Three-dimensional character of the deformation twin in magnesium, Nat Commun 10(1) (2019) 1-7.

[147] M.Y. Gong, J.P. Hirth, Y. Liu, Y. Shen, J. Wang, Interface structures and twinning mechanisms of $\{\bar{1}012\}$ twins in hexagonal metals, Mater Res Lett 5(7) (2017) 449-464.

[148] S. Vaidya, S. Mahajan, Accommodation and formation of $\{11\bar{2}1\}$ twins in Co single crystals, Acta Mater 28(8) (1980) 1123-1131.

[149] S. Mahajan, Twin-slip and twin-twin interactions in Mo-35 at.% Re alloy, Philos Mag 23(184) (1971) 781-794.

[150] N. Stanford, R.K.W. Marceau, and M.R. Barnett, The effect of high yttrium solute concentration on the twinning behaviour of magnesium alloys, Acta Mater 82 (2015) 447-456.

[151] X. Wang, Y. Hu, K.H. Yu, S. Mahajan, I.J. Beyerlein, E.J. Lavernia, Rupert, T.J. Rupert and J.M. Schoenung, Segregation and clustering of Y at $\{10\bar{1}2\}$ twin boundaries in a Mg-Y binary alloy, in preparation.

[152] X.Y. Liu, P.P. Ohotnicky, J.B. Adams, C.L. Rohrer, and R.W. Hyland, Anisotropic surface segregation in Al-Mg alloys, Surf Sci 373(2-3) (1997) 357.

[153] Y. Hu, V. Turlo, I.J. Beyerlein, S. Mahajan, E.J. Lavernia, J.M. Schoenung, and T.J. Rupert, Disconnection-mediated twin embryo growth in Mg, Acta Mater 194 (2020) 437.

[154] M. Ghazisaeidi, L.G. Hector, and W.A. Curtin, Solute strengthening of twinning dislocations in Mg alloys, Acta Mater 80 (2014) 278.

[155] https://sites.google.com/site/eampotentials/Home/MgY

[156] L. Pauling, Atomic radii and interatomic distances in metals, J Am Chem Soc 69(3) (1947) 542-553.

[157] Z.R. Pei, R. Li, J.F. Nie, J.R. Morris, First-principles study of the solute segregation in twin boundaries in Mg and possible descriptors for mechanical properties, Mater Des 165 (2019) 107574.

[158] J.L. Wang, R. Janisch, G.K.H. Madsen, R. Drautz, First-principles study of carbon segregation in bcc iron symmetrical tilt grain boundaries, Acta Mater 115 (2016) 259-268.

[159] R.S. Busk, Lattice parameters of Magnesium alloys, Jom-J Min Met Mat S 2(12) (1950) 1460-1464.

[160] T. Frolov, D.L. Olmsted, M. Asta, Y. Mishin, Structural Phase Transformations in Metallic Grain Boundaries, Nat Commun 4(1) (2013) 1-7.

[161] S. Yang, N. Zhou, H. Zheng, S.P. Ong, J. Luo, First-order interfacial transformations with a critical point: breaking the symmetry at a symmetric tilt grain boundary, Phys Rev Lett 120(8) (2018) 085702.

[162] F. Ram, J.T. Lloyd, and G.S. Rohrer, Habit planes of twins in a deformed Mg alloy determined from threedimensional microstructure analysis, Mater Charact 159 (2020) 110014.

[163] A. Fernandez, A. Jerusalem, I. Gutierrez-Urrutia, and M.T. Perez-Prado, Three-dimensional investigation of grain boundary–twin interactions in a Mg AZ31 alloy by electron backscatter diffraction and continuum modeling, Acta Mater 61(20) (2013) 7679.

[164] Y. Liu, N. Li, S. Shao, M. Gong, J. Wang, R. McCabe, Y. Jiang, and C. Tomé, Characterizing the boundary lateral to the shear direction of deformation twins in magnesium, Nat Commun 7(1) (2016) 1-6.

[165] M.Y. Gong, G.S. Liu, J. Wang, L. Capolungo, and C.N. Tome, Atomistic simulations of interaction between basal <a> dislocations and three-dimensional twins in magnesium, Acta Mater 155 (2018) 187.

[166] K. Dang, S. Wang, M. Gong, R.J. McCabe, J. Wang, and L. Capolungo, Formation and stability of long basal-prismatic facets in Mg, Acta Mater 185 (2019) 119-128.

[167] A. Luque, M. Ghazisaeidi, and W. A. Curtin, A new mechanism for twin growth in Mg alloys, Acta Mater 81 (2014) 442-456.

[168] Y. Chang, J.T. Lloyd, R. Becker, D.M. Kochmann. Modeling microstructure evolution in magnesium: comparison of detailed and reduced-order kinematic models, Mech Mater 108 (2017) 40-57.

[169] Y. Chang, D.M. Kochmann. A variational constitutive model for slip-twinning interactions in single- and polycrystalline magnesium, Int J Plasticity 73 (2015) 39-61.

## APPENDIX A: Derivation of the phenomenological model describing twin embryo growth in pure Mg

The analysis of our MD results showed that the nucleation of disconnections is much faster than their propagation. For example, Fig. 4.3(a) and Fig. 4.5(c) show fast accumulation of twinning disconnections on horizontal twin planes, where new disconnections can be formed on the top of the old ones even before the old twinning disconnections managed to fully traverse across the boundary. As such, we can state that ***the propagation of twinning disconnections along the twin planes is the rate-limiting mechanism behind TB motion***. There is a connection between the twin thickening rate and its size, since the twinning disconnections move at a constant speed (Fig. 4.4(d)) yet the distance that needs to be traveled increases as the twin embryo grows. Homogeneous disconnection nucleation requires higher activation energy than disconnection propagation on flat TBs [30, 31], but the nucleation in our case is heterogeneous and the activation energy alone does not determine the rate-limiting process for TB migration. The distance that twinning disconnections need to travel and the time they spend traveling during TB migration is also important. Through some combination of easier nucleation of twinning disconnections from PB/BP interfaces and the time needed to traverse the TB, disconnection propagation ends up being the rate-limiting process for TB migration. In addition, our MD results show that the BP/PB interfaces are also sources of the twinning disconnections that move along the conjugate (vertical) TBs, leading to the motion of the TTs. However, in this case, we do not observe any accumulation of such disconnections along the vertical boundaries, suggesting that TT motion may be rate-limited by disconnection nucleation.

The velocity of the TT can be approximated as:

$$v_{TT}(t) = \frac{h_d}{t_{tot}} = \frac{h_d}{t_{nucl}+t_{prop}} \approx \frac{h_d}{t_{nucl}} \tag{A1}$$

where $t_{tot}$ is the amount of time needed to traverse the TT. This time can be obtained as $t_{tot}$ = $t_{nucl}$ + $t_{prop}$, where $t_{nucl}$ is the time needed for disconnection nucleation on the TT and $t_{prop}$ is the time needed for the disconnections to propagate until they meet each other and the TT migrates one step further. $t_{nucl}$ is expected to be much larger than $t_{prop}$ according to the analysis of our MD data. In the case of the presence of both homogeneous and heterogeneous nucleation, the exact nucleation time can be determined as:

$$t_{nucl} = \min\left(t_{nucl}^{hom}, t_{nucl}^{het}\right) \tag{A2}$$

where $t_{nucl}^{hom}$ is the time needed for homogeneous nucleation and $t_{nucl}^{het}$ is the time needed for heterogeneous nucleation. While it is commonly assumed that heterogeneous nucleation has a lower nucleation barrier and consequently has a shorter waiting time, this may not be true in the case of the twin embryo. The stress around the twin embryo is not homogeneously distributed, with the positive stresses found near the center of the TT, which may promote homogeneous nucleation. It is also shown that the local distribution of shear stress near the corners of the twin embryo and the centers of the TTs stays relatively constant over time.

The magnitude of TT velocities is time-independent, with $v_{TT}^{right} = -v_{TT}^{left} = v_{TT} = const$. Taking an initial relaxation of the system into account, we consider that disconnection-driven steady-state twin embryo evolution begins at time $t = t_0$. Thus, the positions for the right and left TTs projected on the Y-axis are:

$$y_{TT}^{right}(t) = y_{TT}^{right}(t_0) + v_{TT}(t - t_0) \tag{A3}$$

$$y_{TT}^{left}(t) = y_{TT}^{left}(t_0) - v_{TT}(t - t_0) \tag{A4}$$

where $v_{TT}$ is positive for twin embryo expansion and negative for twin embryo shrinkage along the Y-axis. Thus, the expression for the twin embryo length $l = v_{TT}^{righ} - v_{TT}^{left}$ is:

$$l(t) = l_0 + 2v_{TT}(t - t_0) \tag{A5}$$

where $l_0 = y_{TT}^{right}(t_0) - y_{TT}^{left}(t_0)$.

Similarly, the velocities of TBs are opposite in direction and have the same magnitude, but are not a constant in time, with $v_{TB}^{upper} = -v_{TB}^{lower} = v_{TB} \neq const$. In fact, the TB migration slows down with time, as was observed in Fig. 4.3(b). As the twin length increases, the disconnections are nucleated from the BP/PB interfaces and moving with a constant velocity $v_d$ (see Fig. 4.4(d)), requiring more time to traverse across to push the TB position one step further. Basically, the TB velocity can be approximated as:

$$v_{TB}(t) \cong \frac{h_d}{t'_{tot}} \tag{A6}$$

where $t'_{tot}$ is the amount of time needed to traverse the TB. $t'_{tot} = t'_{nucl} + t'_{prop}$, where $t'_{nucl}$ is the time needed to emit a couple of disconnections at opposite sides of the twin embryo, and $t'_{prop}$ is the time needed for the disconnections to propagate until they meet each other and the TB migrates one step further. Due to the presence of the disconnection sources (BP/PB interfaces), the disconnection nucleation time is much smaller than the propagation time, meaning that $t'_{tot} \approx t'_{prop}$. According to the schematic in Fig. 4.9(b), the propagation time starting from any moment of time $t$ can be estimated as $t'_{prop} = l(t)/(2v_d)$, meaning that each of the two disconnections will on average have to traverse one half of the twin length to complete the corresponding growth of one layer. Thus, the TB velocity can be written as:

$$v_{TB}(t) = \frac{2v_d \cdot h_d}{l(t)} \tag{A7}$$

The average TB position, $z_{TB}$, is then:

$$z_{TB}(t) = z_{TB}(t_0) + \int_{t_0}^{t} v_{TB}(t)dt \qquad (A8)$$

By integrating the TB velocity using Eqs. (A5) and (A7), we can obtain expressions for the positions $z_{TB}^{upper}$ and $z_{TB}^{lower}$ of the upper and lower TBs, respectively, and, thus, obtain an expression for the twin embryo thickness, $h = z_{TB}^{upper} - z_{TB}^{lower}$:

$$h(t) = h_0 + \frac{2v_d \cdot h_d}{v_{TT}} \cdot \ln\left[1 + \frac{2v_{TT} \cdot (t-t_0)}{l_0}\right] \qquad (A9)$$

where $h_0 = z_{TB}^{upper}(t_0) - z_{TB}^{lower}(t_0)$. Using Eqs. (A5) and (A9), the dependence of the twin embryo thickness on the twin embryo length can be also derived:

$$h = h_0 + \frac{2v_d \cdot h_d}{v_{TT}} \cdot \ln\left[\frac{l}{l_0}\right] \qquad (A10)$$

Eq. (10) can therefore be used to estimate the twin thickness at a certain twin length. This phenomenological model can be modified to include the effect of homogeneous nucleation of twinning disconnections on TB migration, but adding this term gives the model an additional fitting parameter without improving the fit to the MD data for the situations targeted in this work. The aspect ratio of the twin embryo, which describes its morphology, can also be calculated as the length divided by thickness:

$$Aspect\ ratio = \frac{l(t)}{h(t)} \qquad (A11)$$